Titre: Title:	3D Scanning-Based Inspection and Repair Geometry Generation for Remanufacturing of Damaged Aeroengine Blades
Auteur: Author:	Hamid Ghorbani
Date:	2022
Type:	Mémoire ou thèse / Dissertation or Thesis
Référence: Citation:	Ghorbani, H. (2022). 3D Scanning-Based Inspection and Repair Geometry Generation for Remanufacturing of Damaged Aeroengine Blades [Thèse de doctorat, Polytechnique Montréal]. PolyPublie. https://publications.polymtl.ca/10218/

URL de PolyPublie: PolyPublie URL:	https://publications.polymtl.ca/10218/
Directeurs de recherche: Advisors:	Farbod Khameneifar
Programme: Program:	PhD.

POLYTECHNIQUE MONTRÉAL

affiliée à l'Université de Montréal

3D scanning-based inspection and repair geometry generation for remanufacturing of damaged aeroengine blades

HAMID GHORBANI

Département de génie mécanique

Thèse présentée en vue de l'obtention du diplôme de *Philosophiæ Doctor*
Génie mécanique

Janvier 2022

POLYTECHNIQUE MONTRÉAL

affiliée à l'Université de Montréal

Cette thèse intitulée:

3D scanning-based inspection and repair geometry generation for remanufacturing of damaged aeroengine blades

présentée par **Hamid GHORBANI**

en vue de l'obtention du diplôme de *Philosophiæ Doctor*

a été dûment acceptée par le jury d'examen constitué de:

Carl-Éric AUBIN, président
Farbod KHAMENEIFAR, membre et directeur de recherche
Oguzhan TUYSUZ, membre
Souheil-Antoine TAHAN, membre externe

DEDICATION

To my beloved wife and my dear parents

ACKNOWLEDGEMENTS

I would like to express my sincere gratitude to my advisor, Professor Farbod Khameneifar, for his continuous support of my research, for his invaluable knowledge, enthusiasm, patience, and his insightful ideas. His motivation and endless guidance inspired me to conduct high quality research during my Ph.D. journey.

I would like to acknowledge the financial support of the Natural Sciences and Engineering Research Council (NSERC) through the Discovery Grants program.

I would like to extend my appreciation to my thesis committee, Professor Carl-Éric Aubin, Professor Oguzhan Tuysuz, and Professor Souheil-Antoine Tahan for their time and efforts to review this thesis.

Furthermore, I appreciate my colleagues in Professor Khameneifar's research team and all my friends at Polytechnique Montréal for making this journey an enjoyable one.

I would also give especial thanks to my parents and my brothers for their continuous support, kindness, and encouragement.

Last but not the least; I would like to thank my loving wife, Fatemeh, for her kindness, patience, and supports in carrying out this work successfully.

RÉSUMÉ

Les aubes des moteurs aéronautiques fonctionnent dans des environnements à haute température et à haute pression. Par conséquent, elles sont susceptibles d'être endommagées et déformées par rapport à leurs formes géométriques de conception au fil du temps. Comme les aubes sont fabriquées dans des matériaux coûteux et difficiles à découper qui nécessitent des coûts de production élevés, la réparation des aubes endommagées est d'un grand intérêt pour l'industrie de la maintenance, de la réparation et de la révision afin de prolonger la durée de vie des aubes. Les systèmes de balayage optique 3D, qui fournissent un nuage de points à haute densité de la pièce à inspecter, sont largement utilisés pour l'inspection des aubes. Compte tenu du nuage de points numérisés en 3D d'une aube endommagée, l'inspection du profil de surface et de la section spécifique, ainsi que la construction du volume de réparation dans les régions où il manque du matériau, constituent un défi et sont considérées comme des sujets de recherche actifs. En pratique, les méthodes existantes pour l'inspection et la construction du volume de réparation des aubes endommagées souffrent d'un manque de précision et dépendent des interactions avec l'utilisateur.

Cette thèse présente un cadre de calcul pour inspecter les aubes endommagées et construire la géométrie du volume de réparation en utilisant des données de nuages de points scannés en 3D et le modèle CAO original. Un algorithme d'alignement rigide entre le scanner et la CAO (scan-to-CAD registration) est proposé pour faire correspondre automatiquement les points de données des régions non endommagées du nuage de points scanné avec le modèle CAO. Une nouvelle méthode de recherche de correspondance est présentée pour l'évaluation de la fiabilité des paires correspondantes dans laquelle la dissimilarité géométrique de chaque paire correspondante est mesurée par une évaluation groupe à groupe des propriétés géométriques du voisinage local de chaque point mesuré et de son point le plus proche sur le modèle CAO. Comme les aubes sont inspectées par sections, une fois que le système de coordonnées de mesure est transformé en système de coordonnées de conception à l'aide de l'enregistrement rigide, un schéma de reconstruction du profil de l'aile entièrement automatique est développé pour l'évaluation de l'erreur géométrique spécifique à la section des profils de l'aile dans les régions non endommagées. Étant donné que les points de données 2D sectionnels projetés à partir de données de nuages de points scannés en 3D sur le plan de section ne sont pas organisés et sont dispersés, une approche de reconstruction du profil de l'aile en trois étapes est présentée afin d'éclaircir automatiquement les points de données sectionnels dispersés en utilisant une technique récursive de moindres carrés locaux pondérés, de générer un polygone de profil fiable à partir des données éclaircies pour ordonner l'ensemble de données, et d'ajuster une courbe B-spline non périodique fermée sur les données ordonnées. Enfin, une nouvelle approche est conçue pour construire un jumeau numérique sans dommage de la lame défectueuse afin de le comparer aux données de balayage et de générer la représentation géométrique du volume de réparation. Le jumeau numérique sans dommage est construit par le biais d'un schéma d'enregistrement non-rigide CAD-to-scan pour déformer progressivement le modèle CAD vers les régions non endommagées des données de scan tout en préservant la rigidité locale des données autant que possible.

ABSTRACT

Aero-engine blades operate in high temperature and pressure environments; and consequently, they are likely to be damaged and deformed from their design geometric shapes over time. Since blades are made of expensive and difficult-to-cut materials requiring high production costs, remanufacturing of damaged blades is of great interest for the maintenance, repair, and overhaul industry to extend the service life of blades. Optical 3D scanning systems, due to providing a high-density point cloud of the part to be inspected, are widely used for blade inspection. Given 3D scanned point cloud of a damaged blade, surface profile and section-specific inspection and construction of repair volume in material-missing regions are challenging and are considered active topics of research. In practice, the existing methods for inspection and repair volume construction of damaged blades suffer from the lack of accuracy and rely on user interactions.

This thesis presents a computational framework to inspect the damaged blades and construct the repair volume geometry using 3D scanned point cloud data and original CAD model. A fine-tuned scan-to-CAD rigid alignment algorithm is proposed to automatically best-match the data points of the undamaged regions of the scanned point cloud with the CAD model. A novel correspondence search method is presented for reliability assessment of the corresponding pairs in which the geometric dissimilarity of each corresponding pair is measured through a group-to-group evaluation of geometric properties of the local neighborhood of each measured point and its closest point on the CAD model. Since blades are inspected in sections, once the measurement coordinate system is transformed into the design coordinate system using the rigid registration, a fully automatic airfoil profile reconstruction scheme is developed for section-specific geometric error evaluation of the airfoil profiles in undamaged regions. Due to the fact that the sectional 2D data points projected from 3D scanned point cloud data onto the section plane are unorganized and scattered, a three-step airfoil profile reconstruction approach is presented to automatically thin the scattered sectional data points using a recursive weighted local least squares technique, generate a reliable profile polygon from thinned data to order the dataset, and fit a closed nonperiodic B-spline curve on the ordered data. Finally, a new approach is devised to construct a damage-free digital twin of the defective blade to compare with scan data and generate the repair volume geometric representation. The damage-free digital twin is constructed through a CAD-to-scan non-rigid registration scheme to gradually deform the CAD model towards the undamaged regions of the scan data while preserving the local rigidity of data as much as possible.

TABLE OF CONTENTS

LIST OF TABLES

LIST OF FIGURES

LIST OF ABBREVIATIONS AND SYMBOLS

List of abbreviations

CAD	Computer-Aided Design
CAI	Computer Aided Inspection
CMM	Coordinate Measuring Machine
CNC	Computer Numerical Control
CSG	Constructive Solid Geometry
DCS	Design Coordinate System
DED	Directed Energy Deposition
DMD	Direct Material Deposition
DT	Digital Twin
GD	Geometric dissimilarity
HNN-crust	Half nearest neighbor-crust
ICP	Iterative Closest Point
k-NN	*k*-Nearest neighbors
LE	Leading Edge
MRO	Maintenance, Repair, and Overhaul
MCS	Measurement Coordinate System
MLS	Moving Least-Squares
MPE	Maximum Permissible Error
NN-crust	Nearest neighbor-crust
NURBS	Non-Uniform Rational B-Spline
PCA	Principal Component Analysis
PCS	Prominent Cross Section
PS	Pressure Side
RE	Reverse Engineering
RMSE	Root Mean Square Error
RWLLS	Recursive Weighted Local Least Squares
TE	Trailing Edge

SO	Sub-Objective
SS	Suction Side
SVD	Singular Value Decomposition
TC	Territory Claiming

List of symbols: Chapters 3

c	Quadric surface coefficients
CP_k	Cut-off point
$\overline{CHD}$	Average Gaussian curvature Hausdorff distance
E, F, G	Coefficients of the first fundamental form
E	Objective function
$\overline{EHD}$	Average Euclidean Hausdorff distance
GD	Geometric dissimilarity
$\overline{HD}$	Average Hausdorff distance
IDX	Data point index
K	Gaussian curvature
L, M, N	Coefficients of the second fundamental form
M_c	Covariance matrix
N_P	Number of points in scan data
$N\overline{CHD}$	Normalized average Gaussian curvature Hausdorff distance
$N\overline{EHD}$	Normalized average Euclidean Hausdorff distance
$\mathrm{N}(p)$	Local neighborhood of point p
O	Centroid of point cloud data
P	Scanned point cloud data
p	Measured data point
q	CAD data point
$\boldsymbol{R}$	Rotation matrix
$S(x, y, z)$	Quadric surface

$SIDX$	Scaled data point index
$\boldsymbol{T}$	Translation vector
x, y, z	Coordinates of a point

List of symbols: Chapter 4

c	Quadric polynomial coefficients
C_s	WLLS fitted curves on the query point s and its neighboring point
$\bar{d}(s)$	Neighborhood distance of the point s
$\bar{D}(s)$	Neighborhood inner distance of the point s
e	Edge of profile polygon
E	Profile polygon edge set
$\hat{f}(x)$	Quadratic polynomial
H	Neighborhood region
I	Imperfect nodes set
K	neighboring points for local curve fitting (Chapter 5)
l	Line at sectional point s parallel to the sectional normal vector $\overrightarrow{N_s}$
N	Number of points in scan data
$\vec{N}$	Normal vector
N_p	Normal vector set of thinned sectional data points
$\mathrm{NB}(v)$	Local neighborhood of point v
$\mathrm{NB}'(s)$	The projection of the 3D data points in $\mathrm{NB}(s)$
n	Number of data points projected on the sectional plane
OF	Outlier Factor
p	Filtered thinned coordinate of scattered sectional point
p^*	Imperfect node
P	Thin 2D point cloud data
q	Node corresponding to incident edge of an imperfect node
q_k	Data point in the local quadric polynomial fitting domain

r	Number of sectional data points whose fitting domain contain query point s
R^*	Angular deviation range for an imperfect node
s	Cross-sectional 2D data point
$\vec{T}$	Tangent vector
u	Standard uncertainty of data
υ	Measured data point
V	Scanned point cloud data
w	Weight value
θ	Angular deviation of the edge of an imperfect node from underlying curve
θ^*	Angular deviation set of an imperfect node
σ	Standard deviation
$\mathcal{N}$	Sectional normal vector set
$\mathcal{S}$	2D scattered sectional dataset

List of symbols: Chapter 5

D	Number of CAD points with the same corresponding point on scan data
D_e	Euclidean distance
E	Non-rigid registration objection function
E_d	Distance minimization term of the objective function
E_s	Stiffness term of the objective function
G_e	Geometric error
m	Number of data points sampled from CAD model
n	Number of data points of scanned point cloud
$\vec{n}$	Normal vector
NB(p)	Local neighborhood of point p
ND_e	Normalized Euclidean distance
$\mathbb{N}_P$	Scan normal vector set
$\mathbb{N}_Q$	CAD normal vector set

$N\theta_e$	Normalized Normal vector angular difference
p	Measured data point
P	Scanned point cloud data
pp	Point-to-point correspondence search
ps	Point-to-surface correspondence search
p^*	The nearest point on the local surface fitted to neighboring points of p to the CAD point q
q	CAD data point
Q	Sampled CAD model point cloud data
r	Stiffness weight coefficient
$\{R_d\}$	Damaged region points
RMS_{we}	Root mean square of weighted error of matching points
$\{S\}$	Seed points
T	Transformation matrix
TC	Territory Claiming
thr	Threshold of region growing segmentation algorithm
w	Weight value of a corresponding pair
α	Stiffness weight value
θ_e	Normal vector angular difference
δ_1	Threshold of the inner loop of the non-rigid registration algorithm
δ_2	Termination threshold of the non-rigid registration algorithm

Chapter 1 INTRODUCTION

1.1 Background Information and Motivation

Aero-engine blades are designed for efficient energy conversion and operation in intense conditions. They are usually made of expensive difficult-to-cut materials requiring high manufacturing costs and produced under extremely tight design tolerances to ensure their functionality. Due to operation in harsh environments, blades are susceptible to fatigue crack, creep, corrosion, etc. which may lead to geometric deformations and material-missing damages on the blade surface. Any deviation of the airfoil profile from its design specifications can adversely affect the performance and efficiency of the aero-engine blade. Thus, blades must be inspected during their service life to check for their conformance to the specified tolerances. Accurate inspection of in-service blades is crucial to make a reliable decision on acceptance, rejection, or repair of inspected blades (Figure 1.1).

Due to significant costs associated with the replacement of new parts, remanufacturing of damaged blades is of great interest for the maintenance, repair, and overhaul (MRO) industry to extend the service life of blades [1]. Around 40 % of MRO costs of an airplane are spent on aeroengine regeneration, mainly remanufacturing of the damaged blades [2]. The damaged blades must be inspected accurately to reduce the high scrap rate of the blades and figure out an effective strategy for remanufacturing the repairable blades.

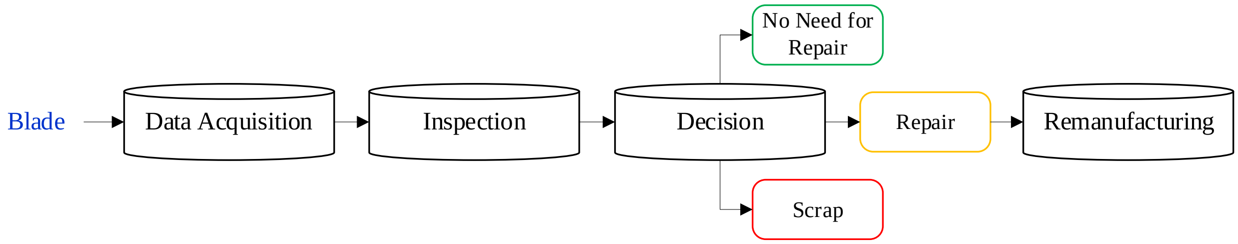

Figure 1.1 Workflow of blade inspection and repair.

To perform accurate inspection and remanufacturing of a damaged blade, MRO sectors should be able to address the following two main questions:

1. How to check for the geometric variations of the damaged blade (i.e., out of tolerance with respect to surface profile tolerance and section-specific tolerances of the blade)?
2. How to generate an accurate representation of repair volume geometry for additive and subtractive restoration of the repairable blade?

As illustrated in Figure 1.1, for inspection of a blade, it is required to collect the inspection data from the blade surface. Traditionally, contact probes on a coordinate measuring machine (CMM) have been used for data acquisition. Although these sensors are known to be very accurate, they are relatively slow and need complicated inspection path planning. Inspection is a crucial task during different lifecycle phases of a blade from manufacturing to end-of-life stages. Therefore, a high-speed inspection process is preferred for maintenance, repair, and overhaul application to collect inspection data from the free-form surface of a blade in a short period of time.

Nowadays, blade manufacturers and MRO industry mostly prefer using non-contact optical scanners for inspection data acquisition. The 3D laser scanning systems (e.g., structured light scanners) provide hundreds of thousands of data points from the inspected part in a short period of time (i.e., just a few seconds) [3]. Although the digitized data mostly are not as accurate as the data of touch trigger probes, application of the non-contact measurement systems is increasing to quickly capture the free-form geometry of blades in the form of point cloud data.

The motivation of this research is to enhance the accuracy and automation in damaged aero-engine blades inspection and remanufacturing with the 3D scanned point cloud data captured from the damaged blade surface.

1.2 3D Scanning-based Inspection of Damaged Blades

As blades are the critical parts of an aero-engine, blade inspection is a crucial task in order to verify the conformity of the measured blade to the specified tolerances and ensure efficient energy conversion. The blade tolerances are typically specified and evaluated in sections. In general, there are three types of geometric tolerances and dimensions for section-specific evaluation of the blades: blade position and orientation tolerances (i.e., three-dimensional tolerances [4]), blade dimensions, and profile tolerance [5]. Blade orientation means the angular relationship of the airfoil to the attachment plane and orientation tolerance is defined as the permitted angular deviation of the airfoil profile from its basic orientation [5, 6]. Position tolerance is also defined as the allowable deviation between practical and theoretical positions of the stacking point (i.e., centroid). Blade dimensions evaluated for airfoil inspection are airfoil thickness dimensions, chord length, minimum radius along the leading and trailing edges, etc. Profile tolerance is used to identify the form error of the airfoil profile and defined as the permitted deviation of the measured profile from the theoretical airfoil profile. In the case of in-service and damaged blades where the blade surface includes significant geometric deformations and/or material-missing defects, evaluation of section-specific deviations of undamaged airfoil profiles from design specifications is an essential step before repair volume computation and remanufacturing process tool-path planning. In addition, the airfoil profiles should be inspected after additive and subtractive restoration to validate the conformance of the airfoil profiles in deposited regions to the specified tolerances.

By emerging the optical 3D scanning systems, this technology has become of great interest for data capturing and geometric inspection of complicated free-form surfaces of airfoil blades. The first problem in the 3D scanning-based inspection of a damaged blade is that the collected point cloud of the damaged blade surface is not located in the same coordinate frame with the CAD model for any surface profile and section-specific inspection. Scan data lie in the measurement coordinate system (MCS) and the CAD model is located in the design coordinate system (DCS) (Figure 1.2).

To address this challenge, the measured point cloud of the damaged blade must be transformed into the design coordinate system using a rigid body transformation. This operation is called either registration, or alignment, or localization in the context of Computer-Aided Inspection (CAI) [7]. All these three terms (i.e., registration, alignment, and localization) refer to the same process and are used interchangeably. The main goal in the rigid registration process is to bring the scan data in a common coordinate system with the nominal CAD model so that the two surfaces can be compared as well as the section-specific geometric errors of the airfoils can be evaluated.

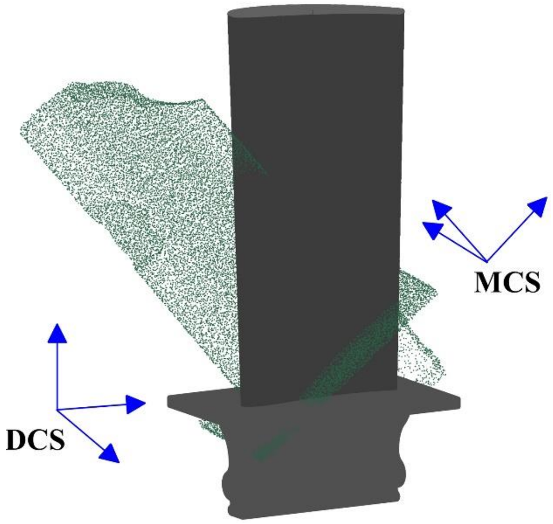

Figure 1.2 Initial position and orientation of the scan data relative to the CAD model.

Iterative closest point (ICP) [8] is one of the most popular computational methods for the localization of free-form surfaces. The ICP algorithm iteratively minimizes the sum of the squared distances between the scanned data points and their closest points on the CAD model using a rigid body transformation to best match two datasets. The original ICP algorithm and other purely Euclidean distance-based least-squares minimization approaches are precise when aligning two identical geometric shapes. Therefore, when the scanned point cloud of a damaged blade is aligned to its CAD model using the original ICP algorithm, due to significant geometric nonconformities between scan data and the CAD model in defective areas, the registration process can be affected by the unreliable correspondences defined in damaged regions. In practice, the original ICP algorithm attempts to best-match the whole point cloud of the damaged blade (i.e., material-missing regions and undamaged areas) to the CAD model to globally minimize the least-squares objective function. This computation introduces averaging-out errors in rigid alignment of the damaged blade where the estimated errors between two datasets at the damaged regions become smaller than the actual errors, and the estimated errors at the undamaged regions become larger than the actual errors. It should be noted that the averaging-out error values depend on the size and the geometry of damages on the scanned damaged blade. When the number of unreliable corresponding pairs belonging to the damaged regions is larger and/or the distance between the unreliable corresponding pairs is greater, the averaging-out error values become larger. In order to avoid the averaging-out errors resulted from the original ICP algorithm, there is a definite need to detect and eliminate the corresponding pairs belonging to damaged regions from the scan-to-CAD rigid registration process. In addition to the geometric nonconformities between two datasets, the noise level of the measurement data can affect the scan-to-CAD rigid registration outcomes. Thus, the registration algorithm should be robust in the presence of different noise levels.

The second problem in quality inspection of damaged blades is to reconstruct the airfoil profile from unordered projected 2D sectional data points for section-specific geometric error evaluation. Once the scanned point cloud of the damaged blade is registered to the CAD model and both datasets are in the design coordinate system (DCS), a smooth airfoil profile should be reliably reconstructed from section-specific inspection data points to check conformance of the airfoil profile to the specified tolerances [6]. Due to the fact that the scanned point cloud is a set of unorganized noisy points all over the blade surface rather than at the pre-specified sections, the 2D cross-sectional data points for pre-specified sections are extracted from the 3D point cloud data through the projection of nearby data points onto the sectional plane [9, 10]. In general, the airfoil profile is approximated using a nonperiodic B-spline closed-curve fitting method. In order to fit a B-spline curve to the sectional data points, it is a need to compute parameter values for 2D data points. However, for the projected set of data points from the 3D scanned point cloud, the order of points is unknown for parametrization (Figure 1.3). Khameneifar and Feng [9] ordered the sectional data points of a 3D scanned point cloud of a newly manufactured blade based on the corresponding closest points on the CAD model. As Figure 1.3 illustrates, due to the considerable deformations on the surface of in-service blades or undamaged regions of damaged blades, the projected sectional points from 3D scanned point cloud are completely unorganized and scattered so that it would not be possible to order sectional data points through closest corresponding points search on the CAD profile.

In addition to the underlying geometry of the sectional data points, there are mainly two other factors affecting the performance of airfoil profile reconstruction methods i.e., measurement noise level and point density. As the real scanned point cloud contains measurement noise, the accuracy of the reconstructed airfoil profile could be affected by any level of noise. The point cloud density is also important when reconstructing the airfoil profile from a 2D sectional dataset. For a small number of sectional data points, the reconstructed airfoil profile may not be able to capture the actual underlying geometry of the blade; and consequently, the section-specific geometric error evaluation of the airfoil profile becomes error-prone. On the other hand, for a large number of sectional data points, the computational efficiency of the airfoil profile reconstruction will reduce.

The fundamental challenge for section-specific geometric error evaluation of damaged blades is to develop a fully automatic methodology to reconstruct the airfoil profile from the scattered 2D sectional data set with high performance in the presence of different measurement noise and point density.

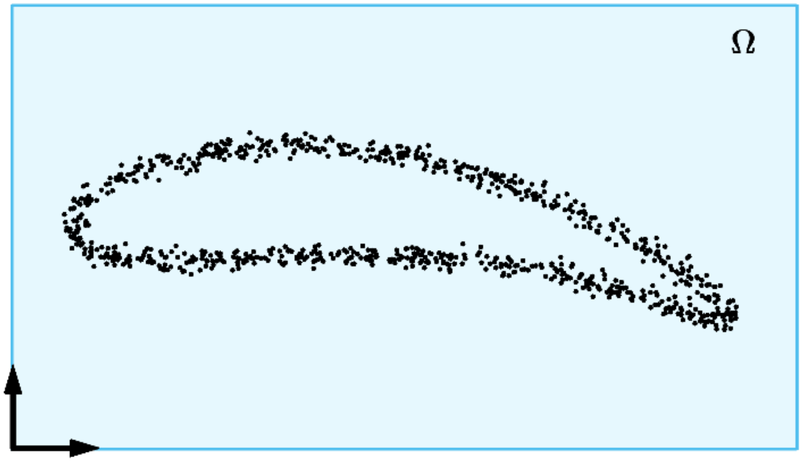

Figure 1.3 Noisy and scattered set of 2D data points projected from 3D scanned point cloud onto the sectional plane Ω.

1.3 Remanufacturing of Damaged Blades

In this study, remanufacturing is defined as restoring the defective aeroengine blade to a like-new condition so that the geometric shape of the repaired blade is preserved within specified tolerances. The development of Hybrid manufacturing provides an effective technical approach for remanufacturing damaged blades in which additive manufacturing (i.e., DED) is employed to fill up the material-missing regions and subtractive manufacturing (i.e., CNC machining and grinding) is utilized to regenerate the original geometric shape of the airfoil profiles in deposited areas.

Accurate repair volume construction is the key to guarantee an accurate toolpath generation for reliable additive and subtractive processes. Once the 3D scanned point cloud of the damaged blade is registered to its CAD model, the geometric representation of the repair volume would be constructed for remanufacturing of the repairable defective blade. In practice, the repair volume is generated by performing a Boolean operation to extract the difference between the scan data of the damaged blade and its nominal model i.e., original CAD model [11, 12] or scan data of an unused blade [13]. However, as illustrated in Figure 1.4, under extreme working conditions, the geometric shapes of aero-engine blades in undamaged regions deviate from the original geometry so that the CAD model or intact blade point cloud no longer represents the current geometric shape of the defective blade. Thus, employing the original CAD model or intact blade point cloud for Boolean operation causes inaccurate repair volume generation and consequently, considerable discontinuity at the interface of the repaired area and unrepaired regions of the blade. Here, the fundamental challenge is how to take the deformations of the undamaged regions to account in repair volume construction.

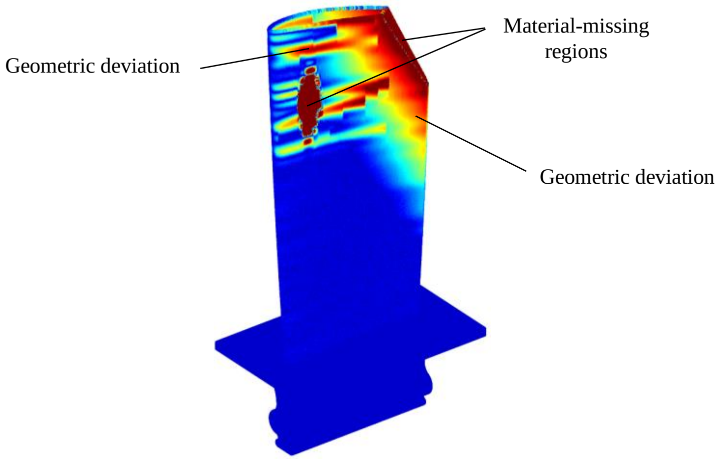

Figure 1.4 A damaged blade with the geometric shapes deviated from the original CAD geometry on the undamaged regions.

To address the original CAD-based repair volume construction problem, some researchers have tried to deform the original CAD airfoil profiles based on the sectional profile information obtained from scan data of the defective blade, and then construct the repaired region geometry through interpolation or extrapolation of modified CAD airfoil profiles [14, 15]. As another solution, reverse engineering (RE)-based methodologies are utilized to construct the geometry of blade surface in damaged regions. In the RE-based methods, the airfoil profiles are reconstructed in undamaged regions of the scan data of defective blade; and then, the repair surface geometry in the material missing region is generated through sweeping a surface across the defective region using the measured airfoil profiles and a guide curve [16, 17].

Employing only a limited number of sectional data in undamaged regions of the defective blade for constructing the blade surface in the material missing area or deforming the original CAD model may lead to incorrect repair volume geometric representation. In addition, interpolation or extrapolation of cross-section curves for damage region reconstruction is an error-prone process.

Thus, there is a definite need to devise an accurate methodology to construct the geometric representation of the repair volume while providing a smooth continuity between repaired and unrepaired regions. Employing the whole scan data instead of only a limited number of sectional data is also essential to generate a reliable repair surface geometry in the material missing region of the damaged blade.

1.4 Research Objectives

The overall objective of this research is to create a computational framework of virtual inspection and repair that can automatically check the conformance of the airfoil profile to the specified tolerances and yield the geometric representation of the repair volume from a 3D scanned point cloud of the damaged blade (Figure 1.5).

Once the blade is scanned and the point cloud data is captured for inspection of the damaged blade, the 3D scanned point cloud is not located in the same coordinate frame with the CAD model. Due to the fact that the rigid body transformation obtained by original ICP-based registration methods may be affected by geometric nonconformities between scan data and CAD model, the data points of the damaged regions should be eliminated from the registration process. Thus, as an early research concentration, the first sub-objective of this thesis is:

First sub-objective (SO1): Develop an accurate scan-to-CAD rigid registration scheme to automatically align the point cloud of damaged aero-engine blades with the CAD model.

Since the airfoil blades tolerances are typically specified and evaluated in sections, it is essential to ensure correct reconstruction of the airfoil profile from unorganized and noisy 2D data points projected from 3D scanned point cloud data onto the section plane. Therefore, for the second sub-objective of this research, we focus on:

Second sub-objective (SO2): Devise a fully automatic methodology to reconstruct the airfoil profile from unorganized 2D sectional data points for section-specific geometric error evaluation in undamaged regions of the defective blade.

The reliable and accurate construction of the geometric representation of the repair volume in material missing regions of the damaged blade is the key to generate the repair tool-paths to deposit correct geometry on damaged regions via the DED technique and regenerate the original geometric shape of the airfoil profiles in deposited areas by adaptive machining process. The repair volume is constructed through a Boolean difference between the scan data and a defect-free reference model of the damaged blade. Thus, the third sub-objective of this thesis is:

Third sub-objective (SO3): Develop a method to generate a damage-free digital twin of the defective blade to ensure accurate and reliable construction of the repair volume geometric representation of the damaged areas (i.e., material-missing regions).

As illustrated in Figure 1.5, integrating these three sub-objectives as a computational framework enables to virtually inspect damaged blades and generate the repair volume for MRO applications.

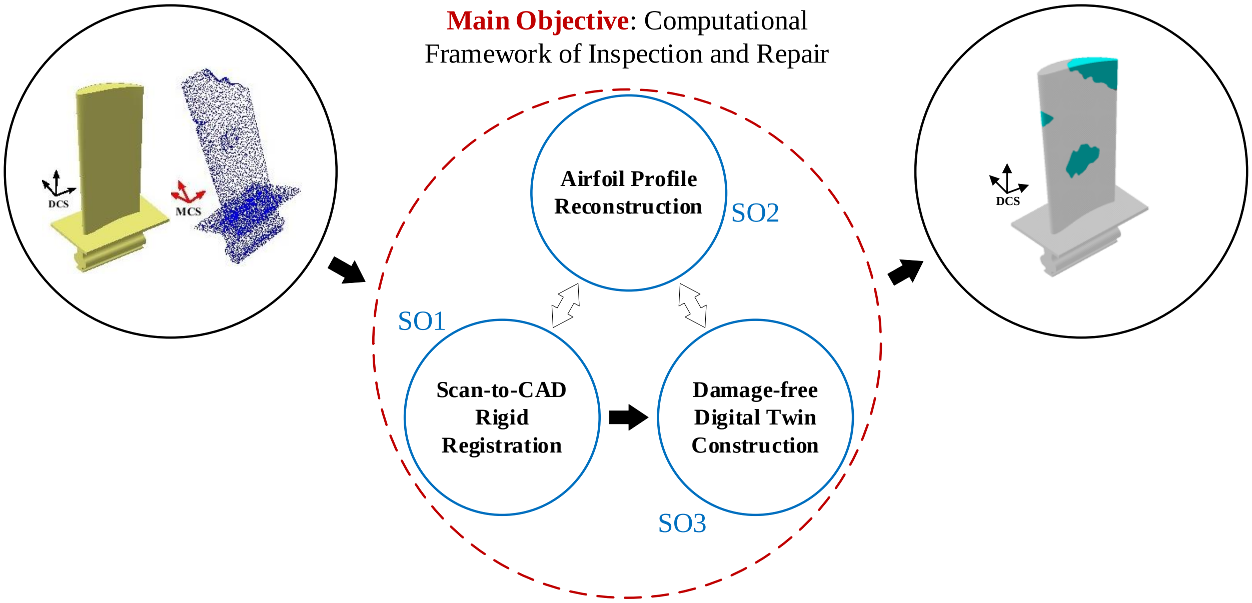

Figure 1.5 Proposed computational framework of 3D scanning-based virtual inspection and repair of damaged blades.

1.5 Thesis Scope

This research seeks to develop a computational framework for virtual inspection and repair volume generation of damaged aero-engine blades. Numerical and experimental case studies have been conducted to validate the proposed framework. In this thesis, the input to the computational framework is a smooth and simplified scan data of simulated damaged blade which is not contaminated by outliers particularly at the high-curvature features i.e., trailing edge and leading edge. However, for the experimental case studies, the raw scan data of the blade (contaminated by outliers at the high-curvature features) is given as input of the computational framework.

Also, it is assumed that the measurement uncertainty of 3D scanned point cloud data is given.

It should be noted that all algorithms and functions of the virtual inspection and repair framework are implemented using MATLAB software.

1.6 Thesis Structure

Following the present introduction, Chapter 2 reviews the relevant work in the literature on damaged aeroengine blades inspection and repair volume construction methodologies. As discussed earlier, for section-specific inspection of a damaged blade it is essential to bring the measured point cloud in a common coordinate system with the nominal CAD model using an alignment approach. Thus, Chapter 3 is dedicated to introduce a new fully-automated method for scan-to-CAD rigid registration of the measured point cloud to the nominal CAD model. In addition, the performance of the proposed method is evaluated in the presence of various noise levels and compared with that of existing approaches. The performance of the rigid registration method proposed in Chapter 3 is examined for an experimental case study with the real scan data and presented in Appendix A. In Chapter 4, a novel method is proposed to automatically reconstruct the airfoil profile from unorganized noisy sectional data points of the measured blade for section-specific geometric errors evaluation of profile in undamaged areas. The performance of the proposed airfoil profile reconstruction approach is also evaluated for different typical levels of measurement noise and density of 3D scanned point cloud data. Chapter 5 presents a new approach to construct a damage-free model of the defective blade for repair volume geometric representation. A CAD-to-scan non-rigid registration technique is proposed to deform the CAD model to best-match to the scanned point cloud in undamaged regions. Finally, the conclusion of this thesis and the proposed future works are presented in Chapter 6.

Chapter 2 LITERATURE REVIEW

This chapter reviews the relevant works in the literature. Each section discusses the existing methodologies on each sub-objective of this research work. Section 2.1 presents the existing methods for rigid registration of scanned point cloud of the damaged blade to its nominal model (SO1: scan-to-CAD rigid registration). Section 2.2 reviews the related works on how to reconstruct a smooth 2D curve from unorganized noisy sectional data points for airfoil profile tolerance analysis with respect to the CAD model (SO2: section-specific geometric error evaluation of airfoil profiles). Finally, Section 2.3 discusses the existing methods for the generation of the blade surface geometry in defective regions (i.e., material missing areas) to yield the repair volume geometric representation (SO3: damage-free digital twin construction).

2.1 Scan-to-CAD Rigid Registration of Damaged Blades

Initially, the collected point cloud of a blade lies in the measurement coordinate system (MCS) which is different from the design coordinate system (DCS). For any surface profile or section-specific inspection of the damaged blades, it is essential to align these two coordinate frames. Registration is defined as to bring the measured point cloud in a common coordinate system with the nominal CAD model. In practice, the rigid registration methods for matching the scanned point cloud to its CAD model can be divided into three main categories i.e., feature-based methods, ICP-based methods, and other methods.

Feature-based alignment methods extract the geometric features from the collected data and CAD model to transform measurement coordinate system into design coordinate system using these features. The “3-2-1” approach (or six-point principle method) is a commonly used feature-based method to establish a reference frame for the part using regular features (e.g. planner surfaces and cylindrical features). At first, three points are measured from the first datum to determine a plane; then, two points are measured from the second datum to establish the second plane perpendicular to the first datum plane; and finally, one point is measured from the last datum perpendicular to the first two datum planes [18, 19].

Hsu et al. [5, 18] proposed an iterative algorithm based on 3-2-1 alignment approach to establish the coordinate system. They developed an iterative coordinate setup process to decrease the measuring time and improve the accuracy of the process. Makem et al. [20, 21] proposed a virtual inspection system to evaluate the dimensions and geometrical parameters of a blade model. They extracted six points on the blade surface (three points on concave surface, two points on the central axis of cylindrical feature at end of blade, and one point located on the root block) to match the finite element model of a forged blade to its nominal model via 3-2-1 approach. In some applications, high precision fixtures are used for rigid alignment of free-form geometry of blades [17, 22, 23]. Because of the simple geometry of fixture features (e.g. ball, plane, sphere, etc.), it is relatively easy and straightforward to obtain the homogeneous transformation matrix and bring the measurement coordinate system into the CAD coordinate system. Fixtures normally require precision manufacturing for both mating surfaces as well as the reference features located by a precision fixture for registration of the part to be inspected [24].

Despite the fact that feature-based approaches are simple and computationally efficient, these methods would not be able to provide an accurate matching result when registration of free-form surfaces such as aero-engine blades [20]. Feature-based registration approaches usually are applied as the rough matching step for ICP-based or other rigid registration methods [25, 26].

Iterative closest point (ICP) [8] is one of the most popular computational methods for the localization of free-form surfaces. The ICP algorithm iteratively minimizes the sum of the squared distances between the scanned data points and their closest points on the CAD model using a rigid body transformation to best-match two datasets.

Since the ICP-based algorithms employ the closest point concept for establishing the correspondence between the two sets, its convergence depends on the initial pose of the two. If the two sets are significantly misaligned, the original ICP may converge towards local minima instead of global minimum [27]. Generally, the ICP-based registration of scanned point cloud can be divided into two steps: coarse and fine registration. The purpose of coarse registration is to find a proper initial estimation of the rigid transformation between two datasets and bring both sets close to each other before ICP registration [28]. Practically, the rough registration could be carried out through various matching methodologies such as geometric features matching [25, 29-33], statistics methods [28, 34, 35], heuristic algorithms [36] and etc. Some researchers have tried to extract the blade features like center points of the trailing edge and the leading edge of airfoil sections, the maximum inscribed circle and maximum thickness of airfoil sections, chord line of airfoil sections, and etc. for coarse registration. Blade features usually are extracted manually on the airfoil sections [30] or 3D scanned point cloud [29]. Others have conducted the coarse registration by aligning the intrinsic features of the underlying surface shape of the point cloud data extracted through shape analysis with the Delaunay triangulation [37], or through feature points picked based on shape descriptor values [33, 38]. Principal component analysis (PCA), as a statistical technique, is used to estimate the principal axes of the two datasets for rough alignment [39]. The PCA-based coarse alignment brings the two datasets close to each other by translating the scan data to a position where it shares the same centroid with its nominal model and then rotating it to align its principal axes with those of the nominal model [28, 35]. The Genetic algorithm also has been applied for rough matching of the scanned point cloud a blade to its nominal model [36].

After initially matching two geometric representations using an appropriate coarse registration, the ICP algorithm iteratively best-matches the whole point cloud to the CAD model. The main idea behind applying the ICP algorithm is to iteratively minimize the sum of the squared distances between measured data points and their corresponding points on the CAD model. A rigid body transformation, comprising a translation vector $\boldsymbol{T}$ and a rotation matrix $\boldsymbol{R}$, is applied to match every measured point p_i with its corresponding point q_i on the CAD model by minimizing a least-squares objective function [8]. A closed form solution for the minimization of the point-to-point error metric can be obtained using the singular value decomposition [40] which has been described in Appendix A. In addition to point-to-point minimization of the ICP algorithm, point-to-plane [41] and point-to-surface [42] minimization strategies are used by variants of the ICP algorithm for rigid body transformation computation [38]. Various studies have tried to remove the effects of outliers from ICP-based registration through the M-estimation principle [43] and signal-to-noise ratio parameter [35, 44].

Optimization methods and heuristic algorithms are other widely used approaches for rigid registration of scanned point cloud to CAD model such as the quasi-Newton optimization algorithm [45], fruit fly optimization algorithm [46, 47], Genetic algorithm [48, 49], and improved Wale optimization algorithm [50].

When registration of damaged blades, the original ICP algorithm attempts to best-match the whole scan data with its nominal model both in damaged and undamaged regions to globally minimize the least-squares objective function. Due to the fact that the least-squares minimization approaches are precise for registration of two identical geometric shapes, any nonconformities between the scanned point cloud and CAD model leads to averaging-out the individual distances between corresponding pairs for the sake of minimizing the objective function. As a result, the approximated errors at the material-missing areas become smaller than the actual errors, and the estimated errors at the non-defective regions become larger than the actual errors. Recently, various studies have been carried out to eliminate the alignment averaging-out errors through the elimination of data points of damaged regions from the registration process. Zhang et al. [13] and Liu et al. [51, 52] extracted the airfoil sections in the non-defective regions of the polygonal mesh model of the scanned damaged blade to align the point cloud data and nominal model. They employed the geometric features of extracted cross-sectional data, i.e., convex hull centroid and the centroid of minimal area bounding-box, for best-matching the two datasets. Calculation of the centroid location from the polygonal model is likely to be subject to area bias and centroid miscalculation [6]. In the related work, Li et al. [29] proposed a modified ICP algorithm to align the scan data with the nominal model based on the curvature and distance of each measured data point from its corresponding closest point on the nominal model. The point-to-point evaluation of geometric features of corresponding pairs makes the algorithm sensitive to noise. The performance of the methods presented in [13, 29, 51] depends on the user-defined thresholds. In addition, these methods require manual settings for the alignment of two geometric representations.

The literature review conducted on existing rigid registration of damaged blades reveals that there is still a gap towards reducing the least-squares minimization averaging-out errors, automating the rigid alignment, and enhancing the robustness of the registration algorithm in the presence of noise.

The scan-to-CAD rigid alignment methodology in this thesis thus aims to automatically best-match the point cloud of the damaged blade with its CAD model while avoiding the averaging-out errors resulted from corresponding pairs of damaged regions. The proposed algorithm starts with a rough matching to initially estimate the transformation between the collected dataset and the CAD model and bring two datasets sufficiently close to each. Then, the original ICP is developed for fine alignment of the whole scanned point cloud (i.e., damaged and undamaged regions) to the CAD. This thesis proposes a new fine-tuned alignment scheme integrating into coarse and fine registrations in order to remove the averaging-out errors resulted from the original ICP through best-matching only the reliable data points of undamaged regions with the CAD model. The fine-tuned registration algorithm applies a novel correspondence search to detect the unreliable measured data points belonging to the defective regions and their corresponding points on the CAD model based on the geometric properties of the local neighborhood of points. Hausdorff distance is utilized for a group-to-group geometric dissimilarity evaluation of each corresponding pair in terms of Euclidean distance and curvature. The devised correspondence search algorithm combines the Euclidean Hausdorff distance and curvature Hausdorff distance to define the geometric dissimilarity function and automatically computes the geometric dissimilarity threshold value based on the data itself in order to identify and remove the unreliable corresponding pairs from the alignment process without the need for user-defined parameters.

2.2 Airfoil Profile Reconstruction from Unorganized Sectional Data Points

Reconstruction of airfoil profile from unorganized scattered sectional data points is a fundamental task in the 3D scanning-based section-specific inspection of the aeroengine blades to check the conformance of the airfoil profile to the specified tolerances [6].

Existing solutions for smooth curve reconstruction from a noisy and unorganized 2D point cloud can be classified into three main categories: global nonlinear optimization approaches to fit a B-spline curve, heuristic algorithms, and skeleton extracting-based approaches.

In the first category, a B-spline curve is fitted to the scattered 2D data points through solving a nonlinear optimization problem in which the parameter value at each point, number and location of the control points, and knot vector are the unknowns of the problem. The iterative least-squares minimization methods usually are applied to solve the non-linear optimization problem [53, 54]. The prevalent method for solving this problem is to separately optimize the parameter values and control points. In each iteration of the curve estimation algorithm, the parameter values are determined by projecting each sectional data point onto the B-spline curve, and then, the location of control points of the fitted curve is computed by minimizing the least-squares objective function for the known parameter values [53, 55]. Some researchers have also tried to find the optimal solution for parameters and control points simultaneously using Gauss-Newton method [56] and L-BFGS optimization method [57].

The non-linear optimization algorithms will converge properly only if a suitable initial curve sufficiently close to the target shape is given [58, 59]. Moreover, due to sensitivity of the curve reconstruction result to outliers, it is essential to remove the outliers from the scattered set of data points.

As another solution, the heuristic algorithms are utilized to approximate a B-spline curve from 2D scattered data points. These algorithms (e.g., genetic algorithm [60], Simulated Annealing [61], and bat algorithm [62]) usually compute the optimal values of unknown variables required for B-spline curve fitting i.e., parameter values of each data point, control points, and B-spline knots. These methods are computationally expensive and can be affected by noise and outliers.

Instead of solving the global nonlinear optimization problem or applying heuristic algorithms, some research works in literature have tried to address the curve reconstructing on the scattered data points through refinement (skeletonize) of the unorganized 2D datasets and fitting an appropriate B-spline on the refined data points. The moving least-squares (MLS) method is one of the useful approaches for smoothing and curve approximation from scattered data points [63]. Lee [64] applied a variant of MLS technique to iteratively project each unorganized data point on the fitted curve to its neighborhood. The support domain size is specified based on covariance analysis of noisy data points to prevent the adverse effects of unwanted points in the local curve fitting. The algorithm expands the support domain gradually to get a suitable radius for which the correlation of data points within the support domain is larger than a pre-specified value. The presented method by Lee [64] requires several user-defined parameters and thresholds which makes this method far from being fully automatic.

Cheng et al. [65] filtered out the noise from the 2D data points using a clustering approach and estimating new points close to the underlying geometry. The new data points are decimated and employed to construct the output polygonal curve using NN-crust [66] algorithm. Ohrhallinger et al. [67] employed the Fitconnect [68] method to reconstruct connectivity between noisy points using HNN-crust algorithm [69], and then the ordered consistent local fits are denoised by blending them together. Some other methods mainly crust and β-skeleton [70] have also been employed in the literature to generate the polygonal curve from 2D unorganized data. In general, the sampling density is an influential parameter on the polygon reconstruction from 2D datasets, which is defined based on the local feature size of data [70].

Lin et al. [71] reconstructed the curve from the 2D unorganized data points using an interval B-spline curve. In their method, 2D data points are clustered into a rectangle sequence to determine the order of the data points which implies the shape of the point cloud. Then, the quasi-centric point sequence and the boundary curves of the point set are computed based on which a centric interval B-spline curve is generated as the final reconstructed curve.

Wang et al. [72] constructed a quadtree of 2D data points and smoothed the grid-like boundaries of the quadtree using a modified Laplacian method, and then extracted the skeleton of the point set through the Voronoi diagram of the smoothed boundaries. Rupniewski [73] selected a number of balls centered at the noisy point set and iteratively reduced their number while moving towards the original curve with a minimum density. Then the rest of the sparse data points can be ordered for polygonal path generation.

All the skeleton extracting-based approaches need user interactions for selecting several parameters and thresholds which should be assigned properly to obtain reliable results. Therefore, the user-defined parameters make the existing methods not readily available for airfoil profile reconstruction for computer-aided inspection of blades. In this application, automation is crucial.

In summary, the existing methods for curve reconstruction from noisy and unorganized 2D data points require some manual interactions and user-defined information such as an initial curve (aka active curve) in non-linear optimization methods or thresholds and parameter values in heuristic algorithms and skeleton extracting-based approaches. The value of these parameters highly depends on the profile geometry, noise, and density of the point set and should be adjusted for different case studies to get reliable results. In addition, there is no benchmark to help find a reliable set of parameter values and thresholds by trial and error for different datasets. Since automation is crucial in the computer-aided inspection of in-service and damaged blades, there is a definite need for the development of a new approach for fully automatic reconstruction of airfoil profile from unorganized noisy 2D sectional data points for section-specific geometric error evaluation.

This thesis aims to devise a fully-automated approach for reconstructing the airfoil profiles from unorganized and noisy sectional data points via thinning of the data points, ordering of thinned data, and fitting a smooth B-spline curve to ordered data points.

2.3 Repair Volume Construction

According to the review of the existing literature, repair volume in material-missing regions of damaged blades can be constructed by performing a Boolean difference between the scanned point cloud and a reference model which should represent the actual underlying geometry of the undamaged regions of the defective blade. The existing solutions for constructing the reference model can be classified into three categories: employing the original CAD model (or scan data of an intact blade), modifying the CAD model by utilizing the sectional profile information obtained from scan data, or applying reverse engineering-(RE) based methodologies to construct the reference model using the measured airfoil profiles.

The common approach to yield the repair volume of the material-missing region is to perform a Boolean difference between the scanned point cloud of the damaged blade and its original CAD model or scan data of an unused blade. Various representations of the CAD model and scanned point cloud of the damaged blade are usually applied for Boolean operation such as point cloud data [11], mesh model [51], voxel model [74], B-rep model [12] and etc. The 3D scanned point cloud of an intact blade also can be applied for comparison with the point cloud of the damaged blade [13, 52]. Some studies also attempted to construct the repair volume through the cross-sectional comparison between the damaged blade and CAD model. Liu et al. [51] proposed a shape-adaption algorithm to compare the polygonal cross-sections of the damaged blade with those of the nominal model to detect the defect segments, and then trim the nominal CAD model using the fracture surface to construct the repair volume. Zhang et al. applied single-dexel modeling [13, 75] and tri-dexel modeling [52] for damage detection and repair volume construction by comparing the intersection of casting rays with the nominal model and damaged blade model. Although the original CAD model and scan data of an unused blade are facile and easy-to-use models for comparison with the measured data of the damaged blade, the generated repair volume geometry in material-missing zones will not provide smooth and reliable continuity with unrepaired regions. Due to extreme working conditions, the geometric shapes of aero-engine blades significantly deviate and therefore CAD model or unused blade point cloud no longer represents the actual geometric shape of the defective blade. In addition, the captured data from the intact blade surface are contaminated by measurement noise and outliers.

In order to address the mentioned errors resulted from original CAD-based repair volume construction, some studies have tried to utilize the sectional profile information in undamaged regions close to the martial-missing areas to transform the deformations on the damaged blade onto the CAD model. These research works aimed to deform the CAD airfoil profiles corresponding to the undamaged regions of the defective blades in order to match these profiles to the measured sectional data; and then, interpolate or extrapolate the deformed CAD airfoil profiles to generate the actual geometric representation of defective blade in the material-missing region [14, 15, 76]. Praniewicz et al. [14] proposed an adaptive repair strategy in which the mean lines of the CAD profiles are manipulated to match to the corresponding mean lines on the measured profiles belonging to undamaged regions in order to get the deformation rules between two airfoil profiles (i.e., CAD profile and measured profile). Then, the CAD profile geometry within the damaged region is obtained via interpolation of the previous transformations to alter the final profile of the nominal model. Wu et al. [76] defined a fitting function based on the material mechanic deformations (i.e., bending and torsional deformations) of blades under the aerodynamic loads to fit the mapping relationship between the blade section curve deformation and blade height. The spline interpolation method is utilized to provide a transition between the undamaged and repaired regions of the welded blade. Yan et al. [15] combined the rigid registration with an offset factor in the normal direction of each point to calculate the rigid and deformation transformations between cross-section curves of the CAD model and measured data in undamaged regions. The geometric shapes of material-missing region are reconstructed through interpolating or extrapolating the airfoil profiles. Employing only several numbers of 2D measured airfoil profiles of the damaged blade to project the deformations onto the CAD airfoil profiles is not accurate enough for repair volume generation. Also, the accuracy of 2D cross-section airfoil profiles constructed using measurement data can significantly affect the reliability of constructed surface in the material missing area. Finally, interpolation or extrapolation of cross-section curves for surface reconstruction is a challenging and error-prone process which may not provide a reliable transition between repaired and unrepaired regions mainly for blade tip damages.

In the third category of methods, the geometric representation of repair volume is generated via scan data and independent from the original CAD model. In this approach, the repair surface geometry is created using RE-based methodologies in which the measured airfoil profiles lying immediately outside the damaged area are swept over the defective region. Gao et al. [77] and Yilmaz et al. [17] constructed the repair surface geometry by sweeping the measured airfoil profiles over the damaged region via a guide curve. Li et al. [29], Wilson et al. [16], and Piya et al. [78] extracted the Prominent Cross Sections (PCS) from the mesh model of the damaged blade and exported them into the CATIA to construct the blade surface. They computed the repair volume through a Boolean difference between the RE-based constructed surface and the mesh surface of the scanned damaged blade. Although RE-based methods do not need the CAD model for repair volume generation, the results of these methods can be affected by the quality of reconstructed airfoil profiles from the sectional data. In addition, RE-based methods utilize only a limited number of measured airfoil profiles in undamaged regions to generate a defect-free model of the defective blade, which is not accurate enough to yield the repair volume geometric representation. Finally, since only the airfoil profiles in top and bottom sides of material missing regions (not the data points in the vicinity of the damage zone) are employed for surface reconstruction, the constructed repair volume geometry cannot provide a smooth geometric transition at the interface of the constructed repair patch and surface of the damaged blade model.

In summary, all of the existing methods for repair volume generation employ the original CAD model or only a limited number of sectional profile information of scan data to construct the repair surface, which may lead to an inaccurate repair volume generation with unsmooth continuity at boundaries of the repaired region with unrepaired areas. This thesis aims to devise a novel methodology in which, instead of the limited number of sectional data, the whole scanned data points in undamaged regions of the defective blade are utilized to construct a damage-free digital twin of the defective blade for repair volume construction. A CAD-to-scan non-rigid registration algorithm is developed to gradually deform the CAD model to match with the scanned data while maintaining the local rigidity as much as possible.

Chapter 3 ARTICLE 1: ACCURATE REGISTRATION OF POINT CLOUDS OF DAMAGED AEROENGINE BLADES

Hamid Ghorbani, Farbod Khameneifar

Published in the *Journal of Manufacturing Science and Engineering, Transactions of the ASME,*
January 29, 2021

3.1 Abstract

This paper presents a novel method for aligning the scanned point clouds of damaged blades with their nominal CAD model. To inspect a damaged blade, the blade surface is scanned and the scan data in the form of a point cloud is compared to the nominal CAD model of the blade. To be able to compare the scanned point cloud and the CAD model, they must be brought to a common coordinate system via a registration algorithm. The geometric nonconformity between the scanned damaged blade and its nominal model stemmed from the damaged regions can affect the registration (alignment) outcome. The alignment errors then cause wrong inspection results. To prevent this from happening, the data points from the damaged regions have to be removed from the alignment calculations. The proposed registration method in this work can accurately and automatically eliminate the unreliable scanned data points of the damaged regions from the registration process. The main feature is a correspondence search technique based on the geometric properties of the local neighborhood of points. By combining the average curvature Hausdorff distance and average Euclidean Hausdorff distance, a metric is defined to locally measure the dissimilarities between the scan data and the nominal model and progressively remove the identified unreliable data points of the damaged regions with each iteration of the fine-tuned

alignment algorithm. Implementation results have demonstrated that the proposed method is accurate and robust to noise with superior performance in comparison with the existing methods.

3.2 Introduction

Aero-engine blades are likely to be damaged during aircraft flights, as they operate in harsh environments. Since they are expensive parts, the blades are repaired to be used again [79]. A crucial factor in the remanufacturing of damaged blades is that the repaired blade must preserve its original geometric shape within certain tolerances specified on the nominal model in order to achieve the efficiency as high as the newly manufactured one [80]. In general, the blade remanufacturing process starts with optical 3D scanning of the damaged blade to capture the geometry of the blade in the form of point cloud data. The reason for using optical 3D scanners (e.g., structured light scanners) is that these non-contact data acquisition techniques yield high-density point clouds (of at least hundreds of thousands of points) in a short period of time (i.e., just a few seconds) [3, 81]. Once the blade is scanned and the point cloud data is captured, very often the blade's point cloud is compared with the nominal CAD model of the blade in order to inspect the part, detect the defects, and construct the repair volume for repairing the defective regions through direct metal deposition (DMD) or hybrid remanufacturing consisting of DMD and machining processes [17, 75].

During the inspection of the damaged blades, in addition to the detection of defects, the inspection process checks for the geometric variations of the blade at the undamaged regions, namely out of tolerance with respect to the surface profile tolerance and the section-specific tolerances of the blade [9, 82-84], which helps to decide whether the blade is repairable or is scrap and should be replaced with a new part [79]. Figure 3.1 shows an outline of 3D scanning-based computer-aided inspection of a damaged blade.

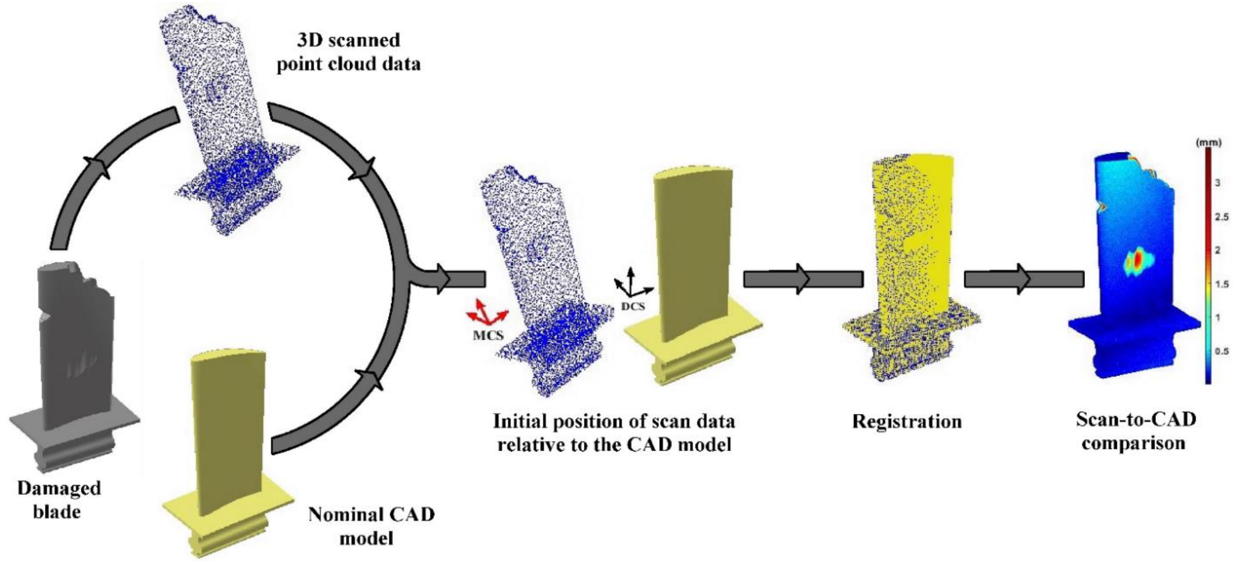

Figure 3.1 Outline of 3D scanning-based computer-aided inspection of a damaged blade.

The 3D scanned point cloud data of the damaged blade must be compared to the nominal CAD model of the blade for inspection. The first problem faced in the inspection is that the point cloud data from 3D scanning is not located in the same coordinate frame with the CAD model. The CAD model is in the design coordinate system (DCS), while the scanned point cloud is in the measurement coordinate system (MCS), which has an arbitrary relative position and orientation with respect to the DCS, as shown in Figure 3.1. A registration algorithm brings the measured point cloud in a common coordinate system with the nominal CAD model so that the two surfaces can be compared and a colormap representing the geometric errors of the part with respect to the CAD model can be generated (Figure 3.1). In the context of CAD-based inspection, registration algorithms are also called alignment or localization algorithms [7]. All these three terms (registration, alignment, localization) refer to the same process and are used interchangeably. The registration of point clouds of damaged blades is challenging and by no means a trivial task, because of the significant geometric nonconformity between the nominal CAD model and the measured point cloud in damaged regions. Accurate registration between the nominal CAD model and the scanned point cloud of the damaged blades is the key to guarantee an accurate geometric inspection, while the registration results can be significantly affected by the defects, depending on the location, size, and geometry of the damages on the blade surface.

The Iterative Closest Point (ICP) algorithm [8] and its variants [41, 42] are the most widely used methods for the registration of the scanned point cloud data of freeform surfaces including turbine blades [29, 35, 38, 85] and will be particularly addressed in this work. The ICP algorithm involves least-squares minimization, where the objective function (*E*) is defined as follows:

$$E = \sum_{i=1}^{N_P} \left\| \boldsymbol{R}.p_i + \boldsymbol{T} - q_i \right\|^2 \tag{3.1}$$

where $\boldsymbol{R}$ is a rotation matrix, $\boldsymbol{T}$ is a translation vector, p_i is any point of the scanned point cloud data and q_i is its corresponding point on the CAD model. N_P is the number of points in the point cloud. In essence, the ICP algorithm iteratively minimizes the combined squared distances between the measured data points and their closest points (in Euclidean distance sense) on the nominal model using a rigid body transformation comprising a translation and a rotation of measured points [8]. While the original ICP method [8] used the distance between a point in one set and its corresponding point on the other set, Chen and Medioni [41] utilized the distance between a point and the computed tangent plane at its corresponding point. Mitra et al. [42] utilized the distance between a point and the approximated local quadric surface at its corresponding point. It is known that any of these binary correspondence assignments are affected by noise and outliers in the point cloud data [86, 87]. Various studies have tried to exclude the outlier data points from the registration procedure using the least median squares regression estimation [43, 88], the M-estimation principle [89], or through heuristic techniques [90].

Since the ICP-based algorithms employ the closest point concept for establishing the correspondence between the two sets (i.e., data points set and the nominal model), its convergence depends on the initial alignment of the two. If the two sets are significantly misaligned, the convergence of the ICP algorithm cannot be guaranteed, since it may fall into the trap of a local solution [27]. For this reason, it is necessary to bring the two sets close to each other in a step known as coarse alignment. Some of the previous works [29-31, 91] have manually extracted and employed certain geometric features for the coarse alignment of the scanned point cloud and the CAD model. For example, the blade features like center points of the trailing edge and the leading edge of airfoil sections, chord line of airfoil sections, etc. can be extracted and used for the coarse alignment. Others have achieved the coarse alignment by aligning the intrinsic features of the underlying surface shape of the point cloud data extracted through shape analysis with the Delaunay Triangulation [37], or through feature points picked based on shape descriptor values [38, 92]. The reliable extraction of feature points from noisy point clouds is not a trivial task and remains a topic of further research.

Principal component analysis (PCA) has been demonstrated to be an effective solution to the problem of coarse alignment of the point cloud data in blade inspection (i.e., for the specific geometry of the airfoil blades) [35]. This statistical technique estimates the principal axes of a dataset. In the PCA method, it is assumed that the origin is at the centroid of the dataset and the three principal axes are the three eigenvectors of the covariance matrix $\boldsymbol{M}_c$ calculated as follows [39]:

$$\boldsymbol{M}_c = \sum_{i=1}^{N_P} (p_i - O)(p_i - O)^T \tag{3.2}$$

where p_i is the i^{th} point of the dataset P, N_P is the number of data points, and O is the centroid of the dataset P. The PCA-based coarse alignment brings the two datasets close to each other by translating the scan data to a position where it shares the same centroid with its nominal model and then rotating it to align its principal axes with those of the nominal model.

Once the two geometric representations are reasonably close, the ICP algorithm carries out the fine alignment. Least-squares minimization of the ICP method exhibits a high sensitivity to geometric nonconformities between the two geometric representations to be aligned. Therefore, when it comes to the alignment of the scanned point cloud of a damaged blade to its nominal CAD model, the measured data points of damaged regions affect the alignment results of the ICP. In each iteration of standard ICP, the algorithm attempts to best-match the data points in both damaged and non-defective (undamaged) regions with the corresponding points of the nominal model and globally minimize the least-squares objective function. This computation leads to averaging out the individual distances between corresponding pairs for the sake of minimizing the objective function. As a result, the estimated errors at the damaged regions become smaller than the actual errors, and the estimated errors at the undamaged regions become larger than the actual errors. Figure 3.2 shows the alignment between the point cloud data of the airfoil profile of a damaged blade and its nominal model to demonstrate the averaging-out errors. This figure illustrates the problem on a 2D profile for the sake of better visualization; nonetheless, the same situation of averaging-out errors occurs in 3D.

Figure 3.2(a) depicts the coarse alignment result where the point cloud data gets sufficiently close to the nominal model. Registration results after the fine alignment using the standard ICP and ideal fine alignment are respectively shown in Figure 3.2(b) and 3.2(c). As it can be seen, employing the standard ICP algorithm for fine registration results in averaging-out errors in the alignment process leading to smaller estimated errors than the actual ones in the damaged region and larger errors than actual in the undamaged regions [29], while an ideal alignment method should avoid these errors by best-matching only the measured data points of non-defective regions with the nominal CAD model.

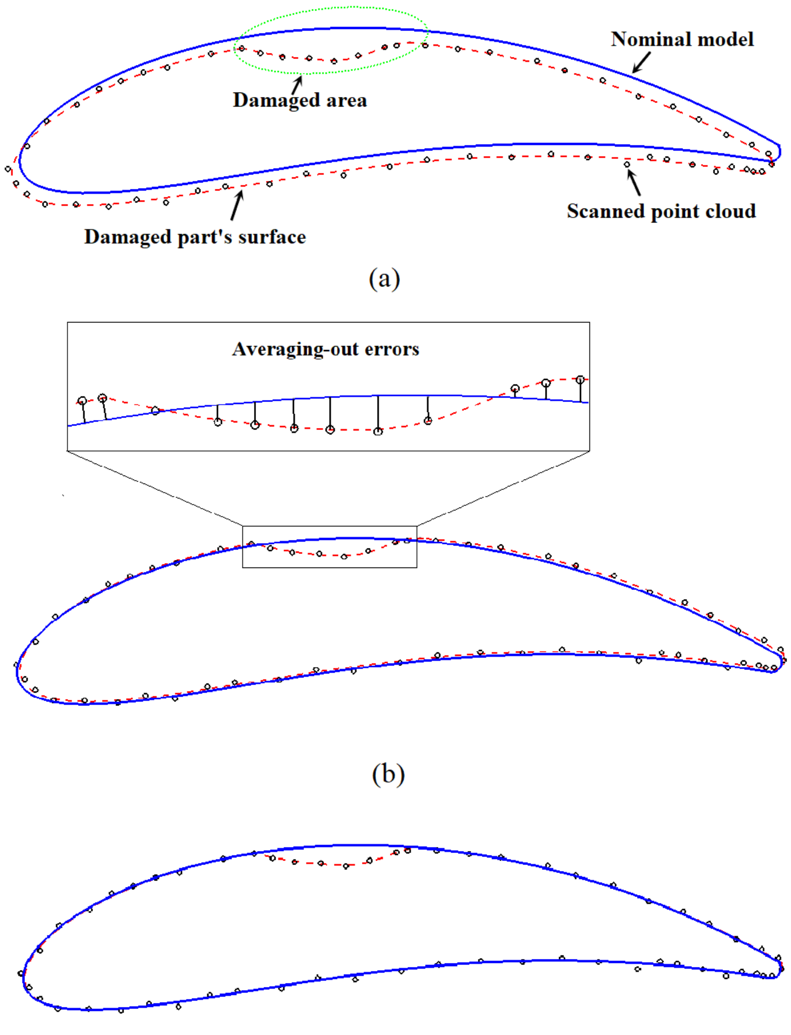

(a)

(b)

(c)

Figure 3.2 Alignment of the point cloud of a damaged profile and its nominal model: (a) result after coarse alignment, (b) result after fine alignment via the standard ICP algorithm, and (c) result after the ideal registration process.

In a related work, Li et al. [29] have discussed the above-mentioned problem of registration using the standard ICP and proposed a modified ICP algorithm to best-match the point cloud of a damaged part and its nominal model. Their proposed correspondence search approach is based on the evaluation of the curvature and distance of each measured point from its corresponding closest point on the nominal model. Their method uses two thresholds associated with the curvature constraint and the distance constraint that must be manually defined by the user. The performance of this method depends on the user-defined thresholds for curvature and distance constraints. In general, the point-to-point correspondence makes the algorithm more sensitive to the datasets variations. Zhang et al. [13] proposed a method based on the comparison of the cross-sectional overlapping area. They extracted an airfoil section in the non-defective region by the intersection of the polygonal mesh model of the scanned blade with a sectional plane, then aligned the scanned model and the nominal model by translating the dataset to a position where the former shares the same position of the convex hull centroid of the extracted cross-section with the latter. Once translated the dataset, they rotated the dataset around the convex hull centroid to achieve the optimum angle that maximizes the overlapping area between the damaged model cross-section and the nominal model cross-section. Similar to Zhang et al. [13], Liu et al. [51] used the cross-sectional overlapping area-based technique but with the multi feature-fitting method in which several cross-sections were used for the registration process instead of only one cross-section. Their algorithm computes the centroid of the polygonized cross-sectional contour and the centroid of the minimal area bounding-box as the features of each cross-section, and then best matches the feature points of cross-sections of the two models (i.e., scan data and its nominal model). Calculation of the centroid location of the airfoil section based on the polygonal model is likely to be subject to an error caused by biased area calculations [6]. In addition to area bias, measurement noise can also contribute to the errors of the centroid calculation [6]. Besides, these methods require manually setting the position of the planes that intersect the models in the undamaged regions.

In summary, the existing methods for alignment of point clouds of damaged blades either apply a point-to-point correspondence search approach to find the relationship between the scanned point cloud and the nominal model, which makes the correspondence search sensitive to the variations of the datasets, or they involve several intermediate calculations of airfoil sections features based on polygonal models, which introduces the aforementioned errors to the overall alignment procedure. In addition, the existing methods are not fully automatic approaches, as they require user-defined thresholds or other parameters that must be set manually.

This paper addresses the mentioned averaging-out errors resulted from the original ICP algorithm and proposes a novel fine-tuned alignment method to avoid these errors. The idea behind the proposed method is to incorporate measures of geometric dissimilarity in the correspondence search method in order to detect and remove the data points belonging to the damaged regions of the damaged blade and their corresponding points on the nominal model in order to avoid the averaging-out issue. Two main features of the proposed method are as follows:

- The proposed correspondence search algorithm uses two metrics, namely curvature Hausdorff distance and Euclidean Hausdorff distance, in the local neighborhood of the corresponding pairs in order to remove each dissimilar pair (the query point and its corresponding point on the CAD model) from the alignment process. A directionally-balanced local neighborhood is established around each query point of the point cloud by the Territory Claiming (TC) algorithm [93], as further explained in Section 3.3.2, and then the group-to-group dissimilarity evaluation of the points in the local neighborhood identifies the dissimilar pair. The philosophy behind the proposed group-to-group dissimilarity evaluation is that one point by itself does not help much for capturing the geometric variations, but when we gather a group of points (the query point and the points in its local neighborhood), they can capture the variations of the underlying surface more reliably. This significantly improves the capability of detecting and removing the unreliable pairs of points from the alignment process.

- The proposed method is fully automatic, as the algorithm automatically computes the required cut-off point based on the data itself in order to identify and remove the points from damaged regions without the need for any user-defined parameter. We explain the cut-off point identification approach in Section 3.3.4.

3.3 Proposed Methodology

The overall alignment procedure includes three main steps to be taken in the following order: 1) coarse alignment using the PCA method [39], 2) fine alignment via the standard ICP algorithm [8], and 3) fine-tuned alignment proposed in this paper. As explained earlier, in the coarse alignment step, PCA is employed to bring the scanned point cloud data sufficiently close to the CAD model. Then, in the next step, the standard ICP algorithm iteratively tries to align the point cloud data and the CAD model. Up to the end of this second step, the alignment procedure is the same as the ones traditionally used, as it was discussed in the introduction section. Although the ICP algorithm provides a relatively close alignment between the two sets, averaging-out errors prevent it from yielding accurate results (Case studies of Section 3.4 present the results of ICP fine alignment and compare it to the registration results after the proposed fine-tuned alignment). Therefore, the particularly important fine-tuned alignment step is proposed in this paper to remove the alignment averaging-out errors through the elimination of data points of damaged regions from the registration process and best-matching only the reliable data points of undamaged regions with the

CAD model in an iterative way. Section 3.3.1 gives an overview of the proposed fine-tuned alignment method, and the details of the algorithm are explained in the next subsections.

3.3.1 Overview of the proposed fine-tuned alignment

The fine-tuned alignment algorithm mainly includes two steps: correspondence search and transformation (i.e., translation and rotation matrices) calculation. A flowchart of the proposed fine-tuned alignment algorithm is shown in Figure 3.3. The inputs to the fine-tuned alignment algorithm are as follows:

- The measured point cloud data aligned with the CAD model through the standard ICP.
- The point-sampled CAD model hereinafter called CAD model data. The algorithm obtains this point cloud by uniform sampling of the nominal CAD model (i.e., the NURBS surface) with the average point spacing of the sampled CAD model point cloud data equal to the measured point cloud data. The reason for keeping the same average point spacing for the two datasets is to analyze the same surface area on both the nominal surface and the underlying surface of the scan data for the subsequent curvature and distance analysis.
- The local neighborhood and the Gaussian curvature at each data point of the measured point cloud and the CAD model data. This will be explained in detail in Section 3.3.2.

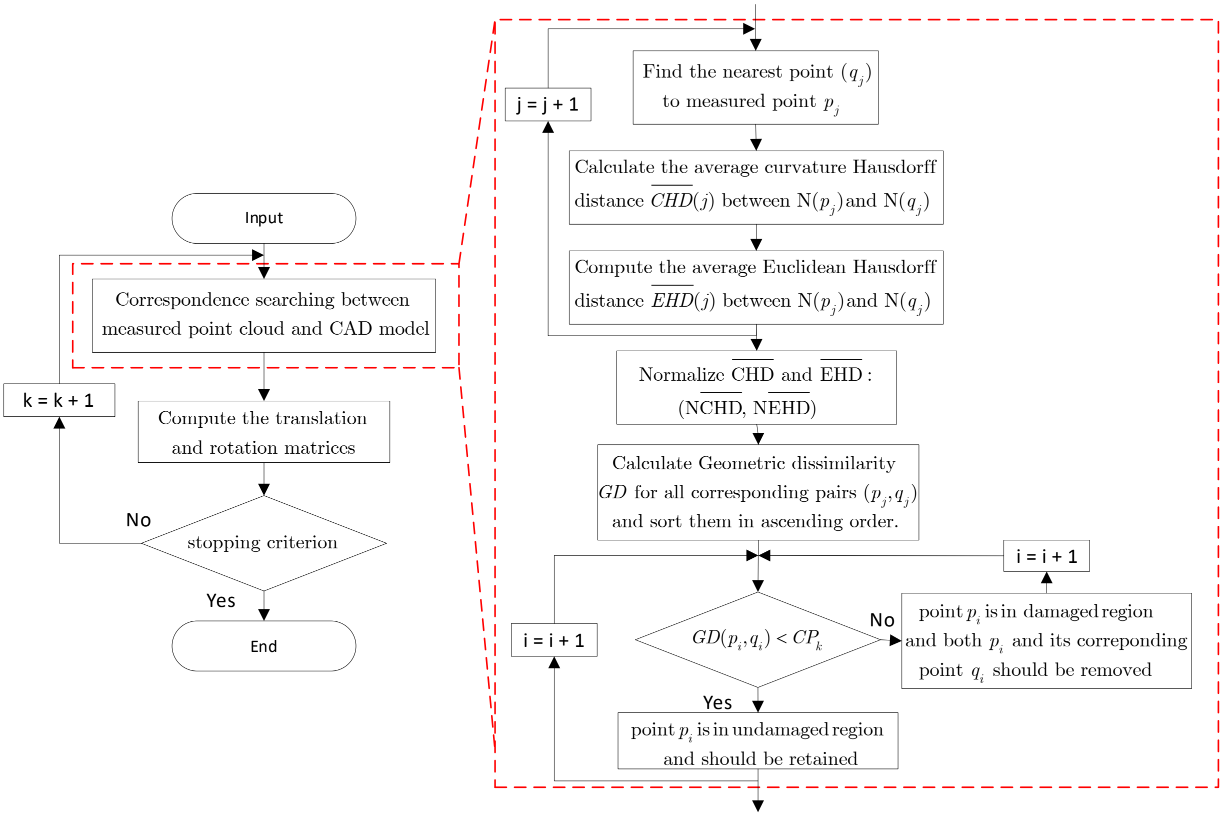

Figure 3.3 Flowchart of the proposed fine-tuned alignment algorithm.

Correspondence search is the key to identifying the unreliable pairs in order to remove them and improve the accuracy of the alignment process. To detect and eliminate the dissimilar pairs in the damaged areas, it is necessary to analyze the local geometric properties in the vicinity of points. The proposed algorithm compares the geometric properties of the local neighborhood of each measured data point with those of its nearest point on the CAD model to compute the geometric dissimilarity between the pair. Using this approach, a group-to-group evaluation of geometric properties is applied to assess the reliability of each pair. Hausdorff distance is utilized to compute the closeness between the local neighborhood of each measured data point and that of its closest point on the CAD model in terms of Euclidean distance and curvature. We use curvature because it is the intrinsic geometric property of a surface that can represent changes of the surface shape, is independent of the global coordinate frame, and is invariant to the rigid body transformation. Euclidean distance computes the positional distance and the curvature distance calculates the changes of the surface shape of the underlying local surface between each measured point and its corresponding closest point on the CAD model. By combining the curvature Hausdorff distance (*CHD*) and Euclidean Hausdorff distance (*EHD*), a geometric dissimilarity function is defined to measure the closeness between scanned point cloud data and the CAD model. Using the proposed geometric dissimilarity function for correspondence search, unreliable pairs with high geometric dissimilarity values are eliminated from the registration process; and consequently, averaging-out errors resulted from the original ICP algorithm are removed.

Once the reliable points are kept, the algorithm computes the rigid body transformation consisting of the rotation $\boldsymbol{R}$ and the translation $\boldsymbol{T}$ that minimizes the sum of the squared error between the corresponding closest points of the two datasets, just like in the original ICP as in Equation (3.1). Then, the computed rotation and translation are applied to the points to be registered. The proposed fine-tuned alignment algorithm employs a similar stopping criterion as in the original ICP based on the global root mean square error of matching points. The algorithm terminates the iteration when the change in the root mean square error between the current iteration and the last iteration falls below a threshold [8].

3.3.2 Curvature estimation and local neighborhood

We estimate surface curvatures via local quadric surface fitting, which is considered as one of the accurate and robust techniques for curvature estimation, especially when dealing with noisy point clouds [94]. For each point p_i and its local neighborhood, the underlying surface can be approximated by fitting, in a least-squares sense, the generic quadric surface of Equation (3.3) to the neighboring points of p_i.

$$S(x, y, z) = c_1x^2 + c_2y^2 + c_3z^2 + c_4xy + c_5yz + c_6zx + c_7x + c_8y + c_9z = 0 \tag{3.3}$$

The fitted quadric surface can be used to estimate the surface curvatures at point p_i. The closest point p_0 on the quadric surface S to the point p_i is calculated; the surface curvatures are computed for the surface S at p_0 and assigned back to the point p_i. The Gaussian curvature K of the quadric surface S at point p_0 is calculated by Equation (3.4):

$$K = \frac{LN - M^2}{EG - F^2} \tag{3.4}$$

where E, F, and G are the coefficients of the first fundamental form, and L, M, and N are the coefficients of the second fundamental form at p_0 [95]. For further details on curvature estimation, readers are referred to [94].

In practice, the accuracy of the estimated curvatures directly depends on the computed local neighborhood of points around the point of interest, especially in the case of noisy point clouds because of the uneven distribution of data points. It is important to establish a balanced neighborhood of points for unbiased local quadric surface fitting and curvature estimation [94]. In the present study, the Territory Claiming (TC) algorithm is applied for establishing the local neighborhood of each point for both curvature estimation and the calculation of Hausdorff distances. The TC algorithm yields a local neighborhood that covers the entire local surface around the query point in a directionally-balanced way and is robust towards noise [93].

3.3.3 Hausdorff distance computation

The Hausdorff distance is a mathematical metric to measure how far two sets are from each other. We employ the average Hausdorff distance to check closeness between the local neighborhoods of corresponding pairs. Average Hausdorff distance is more stable with respect to outliers, thus better shows the geometric relationships between two sets than maximal Hausdorff distance in the presence of noise [96, 97]. The average Hausdorff distance ($\overline{HD}(A,B)$) between two sets A and B is calculated by Equation (3.5) [97]:

$$\overline{HD}(A,B) = \frac{\sum_{a\in A}\min_{b\in B}\left\|a-b\right\| + \sum_{b\in B}\min_{a\in A}\left\|b-a\right\|}{\left|A\right| + \left|B\right|} \tag{3.5}$$

where | . | denotes the cardinality of a set, and || . || denotes the distance between elements of the sets (i.e., points), which can be determined by various distance definitions. This formulation is applicable for the computation of closeness between two datasets in terms of any geometric parameters such as Euclidean distance, curvature, etc.

For each measured point p and its corresponding closest point q on the CAD model, the average Hausdorff distance is computed between neighboring points $N(p_i)$ of measured point p and neighboring points $N(q)$ of point q. With the objective of detecting the geometric nonconformities in the damaged regions, the Gaussian curvature Hausdorff distance can detect the shape changes between local neighborhoods of the corresponding pairs of the scan data and the CAD model, while the Euclidean Hausdorff distance compares them based on positional distance. Therefore, both average Gaussian curvature Hausdorff distance ($\overline{CHD}$) and average Euclidean Hausdorff distance ($\overline{EHD}$) are computed for correspondence search between the scanned point cloud data and the nominal model.

3.3.4 Correspondence search algorithm

In the proposed correspondence search algorithm, a combination of $\overline{CHD}$ and $\overline{EHD}$ is applied for evaluation of dissimilarity between the local neighborhoods of each corresponding pair. This algorithm employs a dissimilarity deduction approach to eliminate the unreliable pairs from the alignment process. The algorithm includes the following steps as shown in the flowchart of Figure 3.3:

Step 1: In the kth iteration of the fine-tuned alignment algorithm, for each measured point p find the closest point q on the CAD model.

Step 2: For each corresponding pair (p, q), calculate the average curvature Hausdorff distance $\overline{CHD}(N(p), N(q))$ and average Euclidean Hausdorff distance $\overline{EHD}(N(p), N(q))$ between neighboring points of p and q (i.e., $N(p)$ and $N(q)$).

Step 3: Normalize $\overline{CHD}$ and $\overline{EHD}$ values using min-max normalization method of Equation (3.6):

$$\begin{aligned} N\overline{CHD}(N(p), N(q)) &= \frac{\overline{CHD}(N(p), N(q)) - \min(\overline{CHD})}{\max(\overline{CHD}) - \min(\overline{CHD})} \\ N\overline{EHD}(N(p), N(q)) &= \frac{\overline{EHD}(N(p), N(q)) - \min(\overline{EHD})}{\max(\overline{EHD}) - \min(\overline{EHD})} \end{aligned} \tag{3.6}$$

This normalization scales $\overline{CHD}$ and $\overline{EHD}$ values into the interval [0, 1] and makes the two variables unitless.

Step 4: Calculate the geometric dissimilarity $GD(p, q)$ between each corresponding pair (p, q). The proposed measure of geometric dissimilarity, defined by Equation (3.7), combines the normalized average curvature Hausdorff distance $N\overline{CHD}(N(p), N(q))$ and the normalized average Euclidean Hausdorff distance $N\overline{EHD}(N(p), N(q))$.

$$GD(p,q) = N\overline{CHD}(N(p), N(q)) + N\overline{EHD}(N(p), N(q)) \tag{3.7}$$

Step 5: Compute the cut-off point CP_k based on the GD values of all the corresponding pairs. If $GD(p, q) < CP_k$ is satisfied, point p is considered to be in the undamaged region, and the corresponding pair (p, q) is retained. If the condition $GD(p, q) < CP_k$ is not met for a point p, then the algorithm concludes that the point belongs to a damaged region as it has a relatively large dissimilarity, thus the algorithm removes the data point and its corresponding point.

To calculate the cut-off point, CP_k, in each iteration of the fine-tuned alignment algorithm, after computation of the geometric dissimilarity for all corresponding pairs, first the algorithm sequences the data points in ascending order of *GD* values. The *GD* versus the data point index (shown in Figure 3.4(a)) is a rotated L-curve. The corner of the L-curve separates the plot into two parts: a part that mainly includes data points with relatively large *GD* values belonging to damaged regions (shown in red in Figure 3.4) and a part that predominantly includes the points from undamaged regions with relatively small *GD* values (shown in blue in Figure 3.4). We thus propose to calculate the corner of the L-curve and set its corresponding *GD* value as the CP_k value. To calculate the corner of the L-curve, the algorithm finds the point on the L-curve with the minimum distance from the point P_k, shown in Figure 3.4(b). Since the data points indices have a broad range of values, to ensure that the computation of corner point is independent of the index scale, it is required to scale the data point index range into the interval [min(GD), max(GD)] to have both data point indices and GD in the same range of values as shown in Figure 3.4(b).

The min-max normalization method of Equation (3.8) is used to obtain the values of the scaled data point index (*SIDX*):

$$SIDX = \min(GD) + \frac{(IDX - \min(IDX)(\max(GD) - \min(GD))}{\max(IDX) - \min(IDX)} \tag{3.8}$$

where *IDX* is the data point index. Employing the scaled data point indices and sorted GD values, the point P_k is defined as [max (*SIDX*), min (GD)].

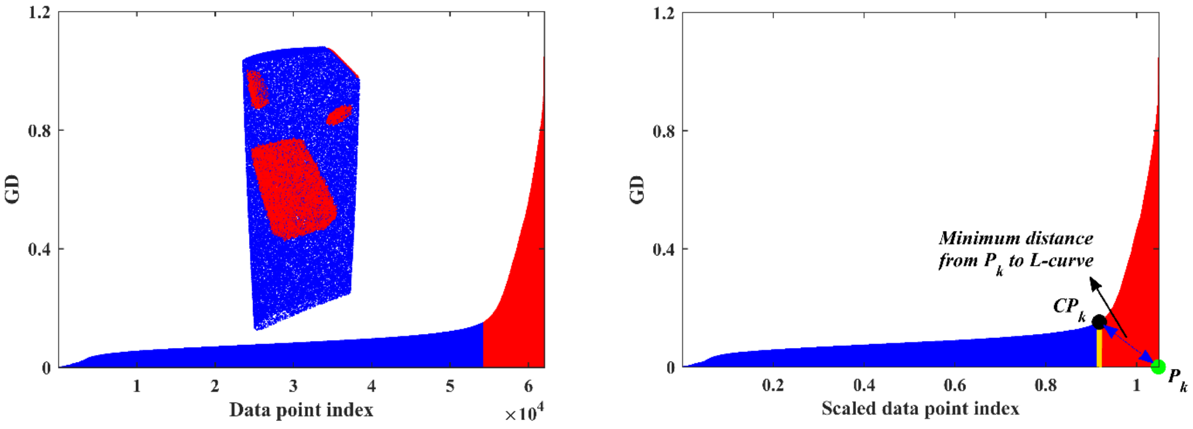

(a) (b)

Figure 3.4(a) Geometric dissimilarity (GD) of the corresponding pairs in ascending order, and (b) GD value of corresponding pairs versus the scaled data point index. Points and values belonging to damaged and undamaged regions are shown in red and blue, respectively.

3.4 Implementation Results and Discussion

Numerical case studies have been conducted to validate the proposed alignment method and compare it with existing approaches. For such validation and comparison, we use synthetic point cloud data generated by sampling simulated damaged blades. This is because actual deviation values between the simulated damaged blades and their nominal CAD model are known that can be used as the benchmark against which the registration outcomes can be compared.

The blade CAD model was created with the overall dimensions of the blade roughly corresponding to a cuboid of 45 mm in length, 15 mm in width, and 105 mm in height. To follow a typical blade surface design, a twist of 25 degrees from the blade bottom to tip was introduced by incrementally twisting the airfoil sections from the bottommost to the topmost section. To simulate the damaged blade surface, a systematic error was first superimposed onto the nominal blade surface, then certain defects were added on the surface. The systematic error was of a sinusoidal variation with the random amplitudes between 0.010 and 0.035 mm, which was superimposed onto the airfoil sections of the CAD model in the direction of the profile normal to emulate the combination of the typical manufacturing errors on the blade surface and the form deviations of the used blade during its service. It should be noted that these form deviations are different from the defects of the damaged blade. Next, geometric defects were added to the airfoil sections to simulate damages on the blade tip at the trailing edge as well as the pressure side of the blade surface. Using the NURBS surface interpolation of the airfoil sections data points, a simulated damaged blade surface was created for which the deviations from the CAD model are known and can be used as a reference. Then, the simulated damaged blade surface was randomly sampled to generate an ideal point cloud (without noise). Figure 3.5(a) shows the nominal CAD model. Figure 3.5(b) and 3.5(c) show the point clouds sampled from the two simulated damaged blades with their error colormap (based on the absolute deviations) with respect to the nominal CAD model. The point clouds of Figure 3.5(b) and 3.5(c) contain 61,165 points and 61,964 points, respectively. As can be seen in Figure 3.5(b) and 3.5(c), the simulated damaged blades contain voids and tip damage, which are common material-missing type damages on the damaged blades of aircraft engines. In order to investigate the effect of damage size on the results, we made the damaged regions of the second simulated damaged blade (Figure 3.5(c)) larger than the first simulated damaged blade (Figure 3.5(b)).

Real scanned point cloud data contain measurement noise. Therefore, the synthetic point clouds should also include the measurement noise for resembling the real scanned point cloud data. In order to generate noisy point clouds of the damaged blades, Gaussian deviates with different levels of known standard deviation (with the distribution’s mean at zero for all cases) were superimposed onto the ideal point cloud in random directions. Using this approach, noisy point clouds with the standard deviation of noise equal to 0.01, 0.02, 0.03, 0.04 and 0.05 mm were generated (10 sets for each level of noise). The specified noise level was decided based on the recent studies on the metrological performance of 3D scanners, in particular, structured light scanners [98].

The origin of the CAD coordinate system is at the centroid of the bottommost airfoil section (at Z=0) as can be seen in Figure 3.5(a). To introduce the initial misalignment to the synthetic point clouds, the point clouds were moved to an arbitrary position and orientation with respect to the CAD model via a rigid body transformation (i.e., with translation and rotation). The initial misalignment, position (X_0, Y_0, Z_0) and orientation $(\theta_x, \theta_y, \theta_z)$, of the synthetic point cloud data is set as (X_0, Y_0, Z_0) = (-20, -20, 20) mm and $(\theta_x, \theta_y, \theta_z)$ = (0.2, -0.3, 0.5) radian.

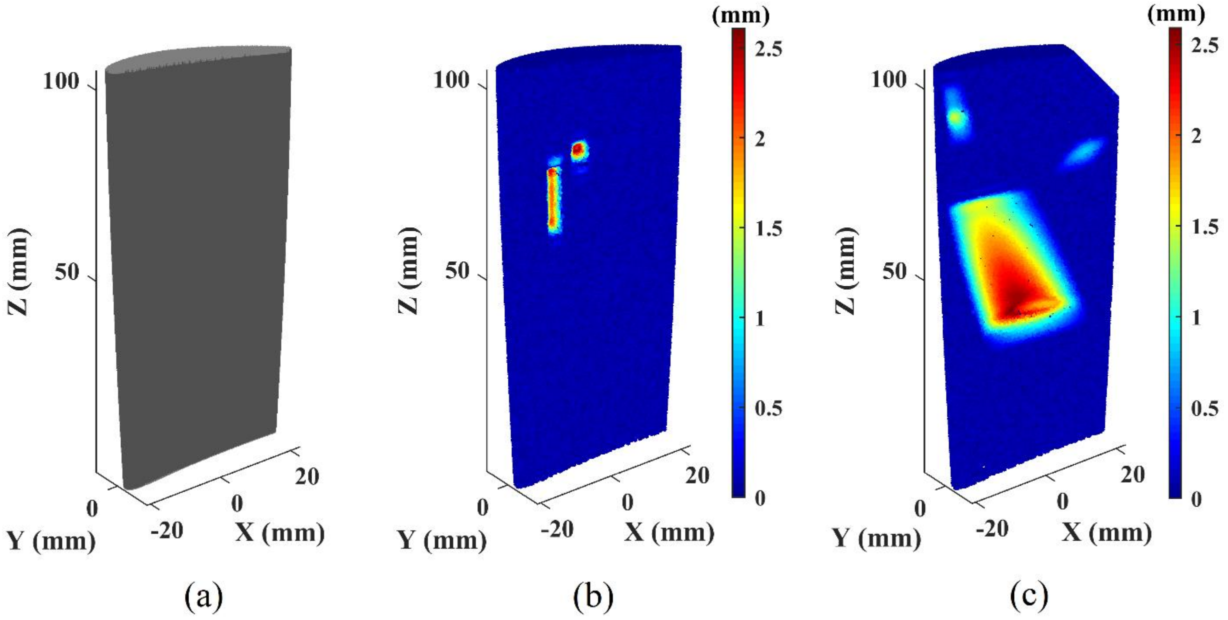

Figure 3.5(a) Nominal CAD model, (b) error colormap of the simulated point cloud (without noise) of the first damaged blade, and (c) error colormap of the simulated point cloud (without noise) of the second damaged blade.

Here, we compare the alignment results of the proposed method with those of the existing methods, namely the standard ICP algorithm [8], Zhang et al.'s method [13], Liu et al.'s method [51], and Li et al.'s method [29]. The standard ICP-based alignment method contains two main steps: rough and fine alignment. PCA method and the original ICP algorithm have been used, respectively, for rough and fine matching, as in [35]. The point-to-point error metric was utilized for the definition of the least-squares objective function to be minimized. The iteration is terminated when the change of the registration global error falls below the specified threshold $\mu = 10^{-6}$.The registration global error is defined as the root mean square error (*RMSE*) of scanned point cloud data from the nominal model after alignment. The thresholds used in each of the existing methods are the values recommended in the related references.

To locally investigate the alignment errors, the point cloud data are sectioned by 20 equidistant sectional planes from bottom (Z=5 mm) to top (Z=100 mm) of the blades and the alignment errors are analyzed for nearby data points of each sectional plane. Sectional planes are parallel to the XY-plane of the design coordinate system (nominal CAD model) and the data points in 0.1 mm distance from each sectional plane are specified as sectional data. The actual sectional error is defined as the root mean square error (*RMSE*) of sectional data points from the nominal model when both the sampled point cloud of the damaged blade and the CAD model are in the design coordinate system (before adding the initial misalignment to the data) as illustrated in Figure 3.5(b) and 3.5(c). Figure 3.6(a) and 3.6(b) show the actual sectional *RMSE* values for 20 sets of sectional data points of the first and the second simulated damaged blades of Figure 3.5(b) and 3.5(c), respectively. After alignment, the *RMSE* of the same sectional data points of the point cloud from the nominal model is calculated and compared to the actual sectional *RMSE* values. The deviation between the two is attributed to the alignment error.

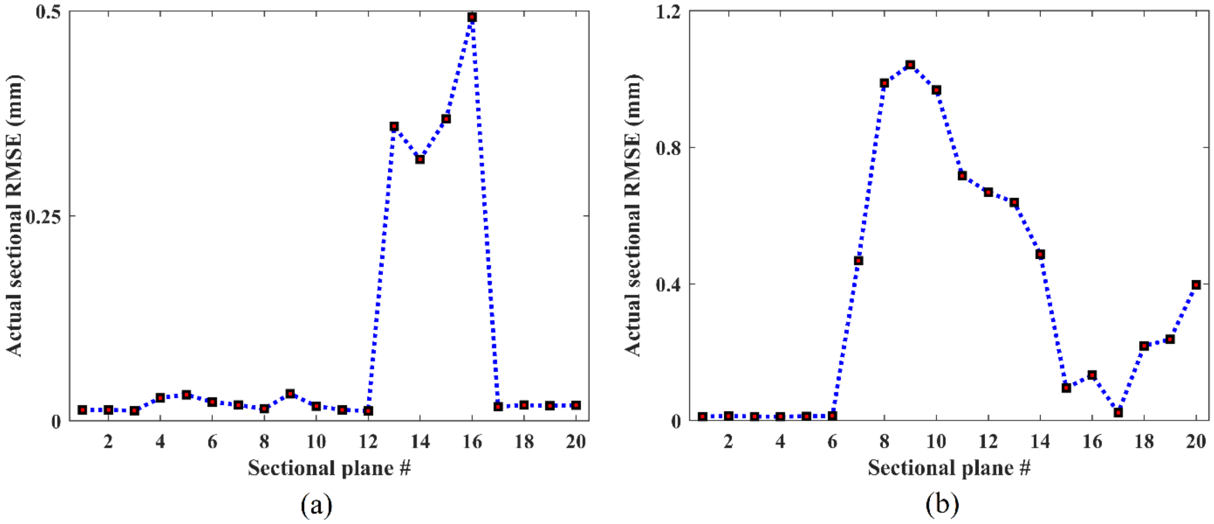

Figure 3.6 Actual sectional RMSE values of the simulated point cloud (without noise) of (a) the first damaged blade, and (b) the second damaged blade.

3.4.1 Alignment results for the point clouds of the damaged blades without noise

Figure 3.7(a) and 3.7(b) plot the deviation of the post-alignment sectional *RMSE* values from the actual sectional *RMSE*s for the point clouds (without noise) of the first simulated damaged blade (Figure 3.5(b)) and the second simulated damaged blade (Figure 3.5(c)), respectively. The results of the proposed method and the other four techniques are shown in the figure. It should be noted that the deviation is calculated as the post-alignment sectional *RMSE* minus the actual sectional *RMSE* for the sectional data points corresponding to each sectional plane. This way the deviation is a signed value, which can better show the averaging-out error.

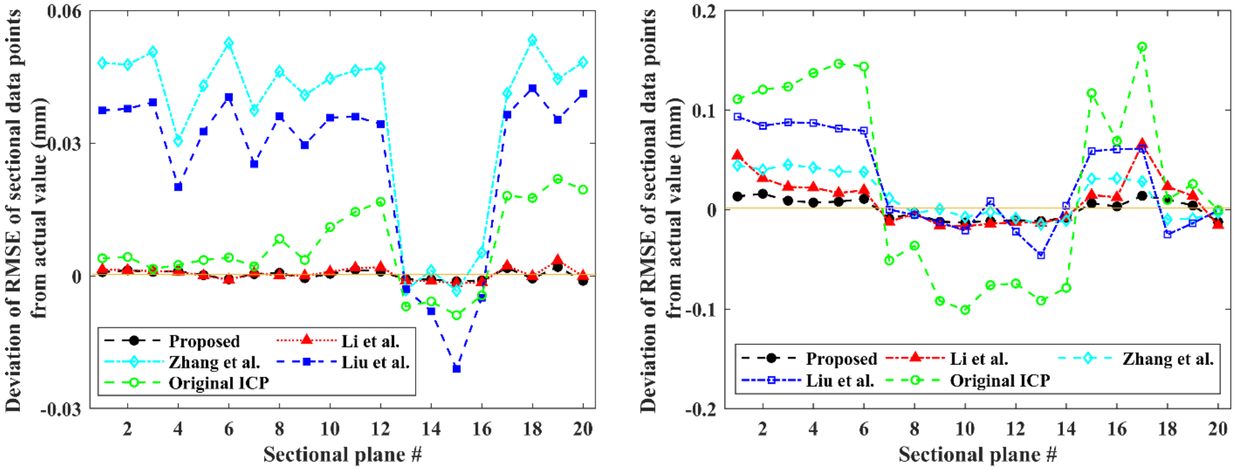

(a) (b)

Figure 3.7 Deviation of post-alignment RMSE of sectional data points (without noise) from actual value for (a) the first damaged blade, and (b) the second damaged blade.

As can be seen in the plots of Figure 3.7, the post-alignment sectional *RMSE* values of the original (standard) ICP method in damaged regions are smaller than the actual *RMSE* values and in undamaged regions are larger than the actual *RMSE* values. As discussed earlier, the standard ICP algorithm globally minimizes the least-squares objective function, which causes these averaging-out errors. This effect is even more noticeable for the second simulated damaged blade containing larger damages, as the post-alignment sectional *RMSE*s of original ICP significantly deviate from the actual sectional *RMSE*s (Figure 3.7(b)). In essence, the averaging-out errors increase as the size of damages on the blade surface increases. In the case of original ICP, the maximum deviations for the first damaged blade in the defective and non-defective regions are respectively 0.009 mm (15th sectional plane) and 0.022 mm (19th sectional plane), while for the second damaged blade, maximum deviations in the defective and non-defective regions are respectively 0.101 mm (10th sectional plane) and 0.164 mm (17th sectional plane).

The post-alignment sectional *RMSE*s of Zhang et al.'s [13] and Liu et al.'s [51] methods, also, have relatively large deviations from actual sectional *RMSE*s. The deviations of the post-alignment sectional *RMSE* values of Li et al.'s [29] method from actual ones are small for the first damaged blade (where the maximum deviation is 0.003 mm), while deviations are considerable for the second damaged blade with larger damages (where the maximum deviation is 0.066 mm). It should be noted that the performance of Li et al.'s [29] method for eliminating the unreliable data points highly depends on the selected user-defined thresholds for the curvature and distance constraints.

For the proposed method, the post-alignment sectional *RMSE* values are very close to the actual sectional *RMSE* values. Maximum deviations of the sectional *RMSE* values after the proposed alignment from the actual sectional *RMSE* values are 0.002 mm and 0.015 mm for the first and the second damaged blades, respectively. Table 3.1 indicates the global *RMSE* of simulated point clouds of damaged blades (without noise) from CAD model after each step of the proposed alignment scheme, namely after PCA, after Original ICP, and after the fine-tuned alignment. In addition, the percentage deviation of the global alignment *RMSE* after each step relative to the actual global *RMSE* is also indicated in Table 3.1. The actual global *RMSE* is specified by computing the root mean square error (*RMSE*) of the synthetic point cloud of the damaged blade from the CAD model when both are in the design coordinate system (before adding the initial misalignment to the data). An ideal registration method should result in the same global *RMSE* as the actual one. As expected, at the end of the second step (after the original ICP), the averaging-out errors cause the post-alignment global *RMSE* to be smaller than the actual global *RMSE*. After applying the fine-tuned alignment, only the reliable corresponding pairs of undamaged regions contribute to the registration process resulting in removing the averaging-out errors. The global *RMSE* after fine-tuned alignment nearly matches the actual global *RMSE* with only 0.0001 mm

(0.06 %) and 0.0041 mm (0.83 %) deviation in the case of the first blade and the second blade, respectively. Figure 3.8(a) and 3.8(b) illustrate the removed data points (in black) at the end of the last iteration of the fine-tuned alignment for the first and the second damaged blades, respectively. Using the fine-tuned alignment, more than 99% of data points of the damaged regions are removed from the synthetic point clouds of both damaged blades. As can be seen in the figure, some data points of the undamaged regions are also removed as unreliable points, which do not affect the accuracy of the alignment process as the removed undamaged points are a tiny portion of the whole data points of undamaged regions (1.6% and 0.7% of the points of undamaged regions in the case of the first and the second blade, respectively).

Table 3.1 Global *RMSE* of the point clouds of the damaged blades from the CAD model after each step of the proposed alignment scheme, and the actual (reference) global *RMSE*, and the percentage deviation of the global *RMSE* after each step relative to the actual global *RMSE*.

	Global *RMSE* (mm)				Deviation from Actual (%)		
	Actual	PCA	ICP	Fine-tuned	PCA	ICP	Fine-tuned
1st blade	0.1798	0.4455	0.1568	0.1797	147.78	12.79	0.06
2nd blade	0.4967	0.6379	0.4620	0.4926	28.43	6.99	0.83

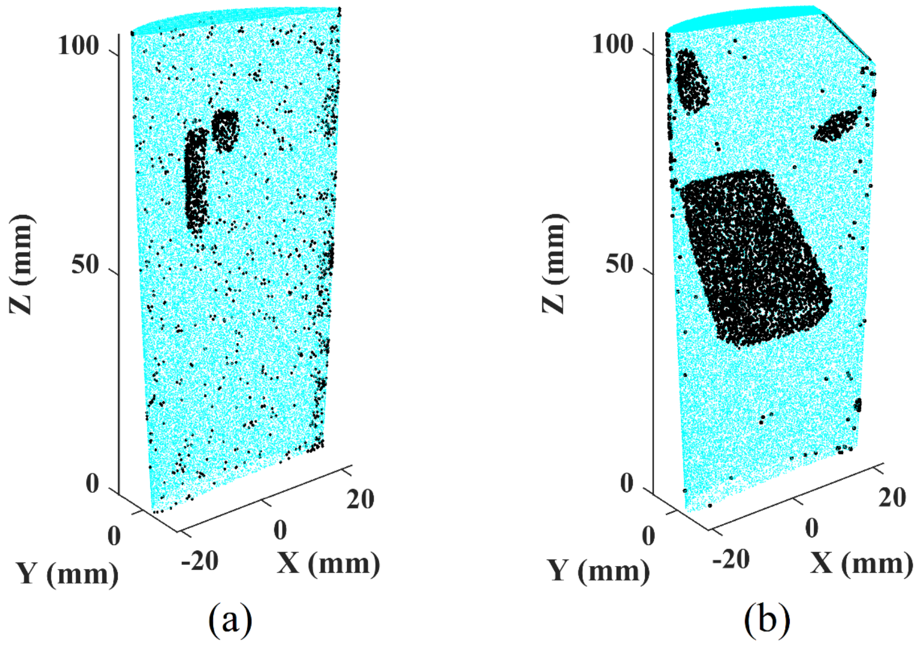

Figure 3.8 Removed data points (in black) after the last iteration of the fine-tuned alignment for (a) the first blade, and (b) the second blade.

3.4.2 Alignment results for the noisy point clouds of the damaged blades

Next, we evaluated the performance of the proposed method in the presence of noise and compared it to that of the existing methods. We used the generated synthetic noisy point clouds (10 sets for each level of noise as described earlier) for this evaluation. Figure 3.9(a) and 3.9(b) show the average of absolute deviations of post-alignment sectional *RMSE* values (of all 20 sections) from the actual sectional *RMSEs* for each method for different levels of noise (of 0.01, 0.02, 0.03, 0.04 and 0.05 mm noise), respectively for the first and the second damaged blades. For each alignment method, we have calculated the average of absolute deviations (average of 20 absolute values corresponding to the 20 sections) for each of the 10 synthetic noisy datasets of a specific level of noise and have reported the average of the 10 numbers in Figure 3.9 for each level of noise. We also added the case without noise (with 0 mm noise) to the plots for comparison of the results with noise and without noise.

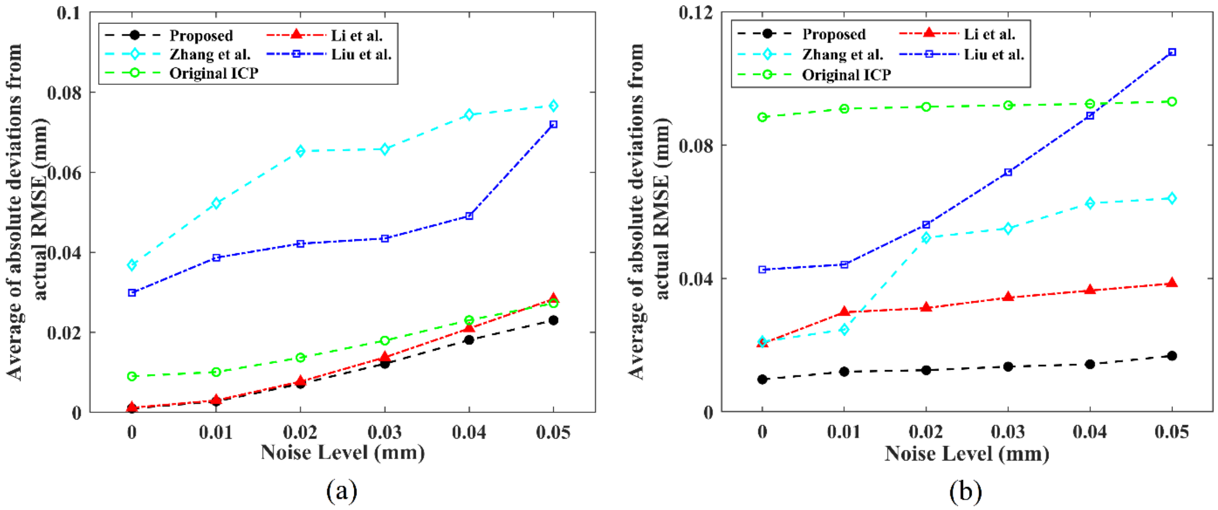

(a)

(b)

Figure 3.9 Average of absolute deviations of post-alignment sectional RMSEs from actual sectional RMSEs for different levels of noise: (a) first damaged blade, and (b) second damaged blade.

As seen in the plots of Figure 3.9, Zhang et al.'s [13] and Liu et al.'s [51] methods are the most sensitive to noise, as the alignment sectional *RMSE* values in these methods are more deviated from the actual sectional *RMSE* values than the other methods. This was expected because, in the presence of noise, the mesh reconstructed from the point cloud data becomes more distorted, which leads to centroid miscalculation, as the centroid is calculated based on the reconstructed polygonal model. The results of Figure 3.9(a) for the first damaged blade indicate that the measurement noise affects the performance of the original ICP algorithm, which is in agreement with the findings of the previous works on ICP [99]. Using the original ICP algorithm, the correspondence search is affected by noise, which causes the post-alignment sectional *RMSE* values to become more deviated from the actual ones as the noise level increases. However, this effect is not noticeable in the plot of Figure 3.9(b) for the second damaged blade since the larger size of the damages makes the averaging-out errors much larger than the effect of noise, therefore the effect of noise is negligible in that case in comparison with the averaging-out errors. The average of absolute deviations from the actual sectional *RMSE* values for the proposed fine-tuned alignment method is the smallest of all methods for all the tested synthetic point clouds of different levels of noise. Compared to Li et al.’s [29] method, for the first damaged blade, the proposed method results in an incremental improvement for the case without noise and for the low-noise data. The improvement becomes more significant when higher levels of noise are present in the point cloud data. For the second damaged blade containing larger damages, the proposed method yields significantly better results even in comparison with Li et al.’s [29] method.

The results of aligning the noisy point clouds with the nominal model using different methods demonstrated that the performance of the proposed fine-tuned alignment is superior over the other existing methods in the presence of noise as it was equally the case without noise.

3.5 Conclusion

An accurate and automatic method for alignment of the 3D scanned point clouds of damaged blades to the nominal CAD model has been presented in this paper. While most studies in the literature employ the iterative closest point (ICP) algorithm for alignment, the ICP-based algorithms suffer from averaging-out errors resulted from geometrical nonconformities between the measured point cloud in damaged regions and the CAD model. Because an ICP-based algorithm globally minimizes the distance of the data points of both damaged and undamaged regions from their corresponding closest points on the nominal model. Consequently, the estimated errors at the damaged and undamaged regions become, respectively, smaller and larger than the actual errors, which leads to wrong inspection results and mistaken repair process planning. The presented work addresses the problem of averaging-out errors and proposes an effective method to avoid them. The essential contribution of the proposed method lies at reliably eliminating the points of the damaged regions from the alignment process. By combining the average curvature Hausdorff distance and average Euclidean Hausdorff distance, a metric is defined to evaluate the geometric dissimilarity of the local neighborhood of corresponding pairs. Employing a dissimilarity deduction approach, the corresponding pairs with high geometric dissimilarity are gradually removed from the alignment process. The implementation results from various case studies of synthetic point clouds of simulated damaged aero-engine blades have demonstrated the effectiveness of the proposed method in eliminating the alignment averaging-out errors by removing unreliable corresponding pairs. The proposed method is deemed a more accurate approach for alignment of point clouds of damaged blades than the other existing methods.

Chapter 4 ARTICLE 2: AIRFOIL PROFILE RECONSTRUCTION FROM UNORGANIZED NOISY POINT CLOUD DATA

Hamid Ghorbani, Farbod Khameneifar

Published in the *Journal of Computational Design and Engineering,* February 28, 2021

4.1 Abstract

Airfoil blades are typically inspected in sections to verify their conformance to the geometric tolerances specified on their nominal design. To maintain the accuracy of geometric error evaluation, in particular, for the position and orientation errors of the airfoil sections, sectional airfoil profiles should be reconstructed from the inspection data points. This paper presents a new method to automatically reconstruct the airfoil profile from unorganized noisy sectional data points of 3D scanned blades. A three-step airfoil profile reconstruction approach is presented. First, the algorithm thins the scattered set of sectional data points by projecting them onto the local curves fitted to them. For this purpose, a recursive weighted local least squares scheme is proposed to fit local curves within the measurement uncertainty constraint of inspection data. Then, to order the thinned set of data points, the profile polygon is generated and imperfect nodes are modified by evaluation of the angular deviation of edges. Finally, a closed non-periodic B-spline curve is fitted to the thinned and ordered set of data points to construct the smooth airfoil profile. A series of case studies have been carried out to demonstrate the effectiveness of the proposed airfoil profile reconstruction method. Implementation results have demonstrated that the proposed method is accurate and robust to noise. In addition to blade inspection, other applications such as repair and adaptive machining of aero-engine blades can equally benefit from the proposed method for automatic airfoil profile reconstruction.

4.2 Introduction

Aero-engine blades are designed for efficient energy conversion and operation in intense conditions. These blades need to be manufactured under extremely tight tolerances. Once manufactured, the blades must be precisely inspected to verify their conformance to the specified tolerances [5]. In addition, in-service blades are susceptible to geometric deformations due to operation in harsh environments. Any deviation of the airfoil profile from its design specifications can adversely affect the performance and efficiency of the aero-engine. Therefore, in-service blades must also be accurately inspected during the maintenance, repair and overhaul (MRO) operations to check for their conformance to the specified tolerances. In addition to being used as a means of acceptance or rejection of the inspected part, the correct representation of geometric error distribution on the blade also provides the fundamental feedback for improving the associated manufacturing process. Accurate blade inspection is equally crucial for the MRO application for finding an effective strategy for the remanufacturing of repairable blades [1].

The blade tolerances are typically specified and evaluated in sections [5, 6]. Inspection data points are thus acquired for pre-specified sections during the data acquisition phase of inspection. Traditionally, contact probes on a coordinate measuring machine (CMM) were used for data acquisition. The CMM data acquisition is though relatively slow and needs complicated inspection planning [19]. Nowadays, blade manufacturers and the MRO industry mostly prefer using optical 3D scanners, since it is a much faster way of acquiring inspection data. 3D scanners provide hundreds of thousands of data points from the inspected part in a short period of time [3]. However, the point cloud collected by optical 3D scanning is a set of unorganized noisy points all over the blade surface rather than at the pre-specified sections. The cross-sectional 2D coordinate measurement data points for pre-specified sections are therefore extracted from the 3D point cloud data through the projection of nearby data points onto the sectional plane [9, 10]. Figure 4.1(a), (b), and (c) respectively show an airfoil blade, its 3D scanned point cloud data, and the cross-sectional 2D data points extracted via projection.

Before projection, the 3D scanned point cloud (as shown in Figure 4.1(b) for instance) has passed several pre-processing steps including smoothing and outlier removal, as well as registration. The raw scanned point cloud data of a blade is often contaminated by outliers (i.e., points with very high levels of noise) at the high-curvature features (i.e., leading and trailing edges) due to undesirable reflections in the scanning process [100]. An appropriate point cloud smoothing process is applied to reduce noises and remove outliers from the point cloud data while preserving the underlying geometry of the blade surface. Li et al. [101] proposed an adaptive bilateral smoothing method, which can effectively smooth the scanned point cloud of a blade and preserve high-curvature features. Li et al. [81] also proposed a clustering-based method for simplification (i.e., removing redundant points) of the blade point clouds. In both studies, in order to keep the underlying geometry of high-curvature regions (i.e., leading and trailing edges) and avoid the volume shrinkage, the information entropy in *k*-nearest neighbors (*k*-NN) is defined to get a balance between point smoothing and preserving the geometry using respectively two factors namely surface-smoothing factor and feature-preserving factor.

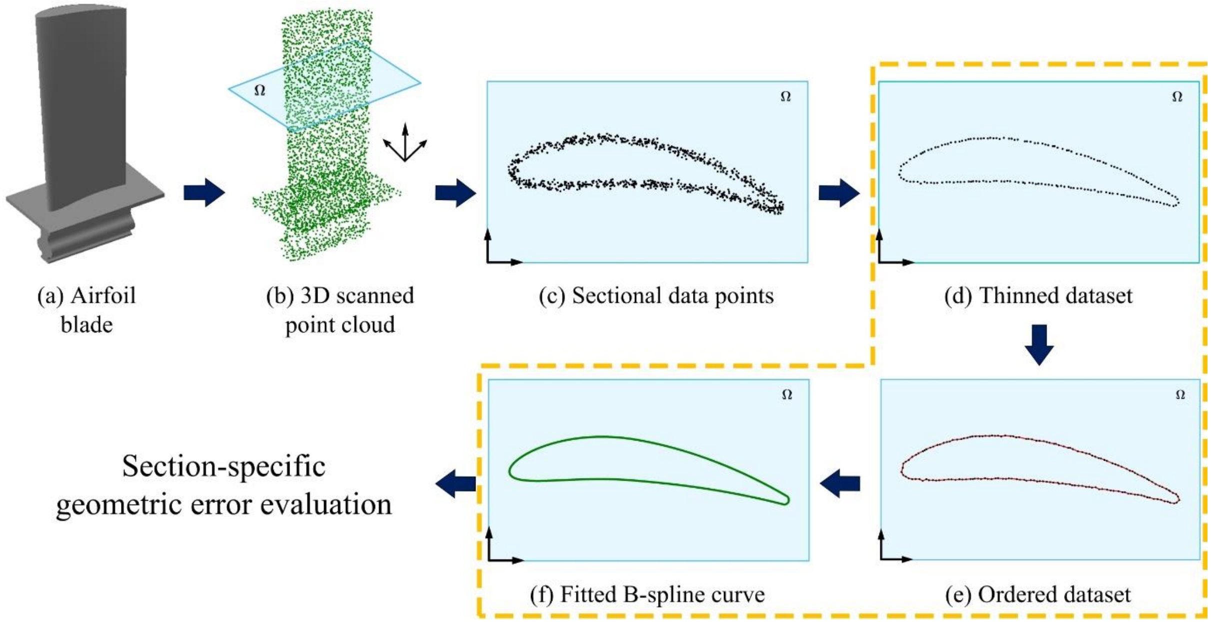

Figure 4.1 Outline of 3D scanning-based airfoil inspection. The framework proposed for airfoil profile reconstruction is shown inside the orange dashed-line frame.

Initially, the scan data lies in the measurement coordinate system (MCS), which is different from the design coordinate system (DCS) in which the CAD model lies. For inspection, it is required to bring the scanned point cloud data to a common coordinate system with the CAD model using an appropriate registration (aka alignment, localization, or matching) method. Traditionally, the iterative closest point (ICP) algorithm [8] and its variants [42] are the most widely used methods for registration of the scanned point cloud data of free-form surfaces including turbine blades. Li et al. [102] proposed a novel registration method to address the incorrect registration outcome due to missing points and uneven-density regions of the scanned point cloud data of blades. Their proposed algorithm successfully calculates the shape matching parameters using a weighted variance-minimization objective function. Xie et al. [103, 104] studied the convergence of the proposed variance-minimization matching (VMM) technique and presented a series of experiments to verify the performance of this very interesting method. In the case of damaged blades in repair and re-manufacturing applications, there is an extra challenge in registration arising from the geometric nonconformity between point cloud data of scanned damaged blade and its nominal CAD model. Ghorbani and Khameneifar [28] proposed a method for the alignment of damaged blades by using a correspondence search technique based on the geometric properties of the local neighborhood of points to remove the effect of the damaged regions from the registration outcome. In the present work, it is assumed that the scanned point cloud data is already registered to the CAD model, therefore lies in the design coordinate system. Sectional planes intersecting scanned point cloud data (as shown in Figure 4.1(b)) are specified in the design coordinate system of the CAD model. The 3D points are projected onto the pre-specified sectional planes to obtain the cross-sectional 2D coordinate measurement data points.

To ensure accurate evaluation of position and orientation tolerances of airfoil sections, the smooth airfoil profile should be reliably reconstructed from section-specific inspection data points [6]. Given that scanned data is subject to measurement uncertainty, actual sectional airfoil profiles of a blade can never be exactly generated from the data points. Nevertheless, the profile can be reliably approximated using a closed-curve fitting method, which directly targets airfoil profile reconstruction. In a related work, Khameneifar and Feng [84] have proposed a method for reconstructing the airfoil profile from 2D data points obtained by CMM measurement. A closed non-periodic B-spline curve is used in [84] to represent the reconstructed airfoil profile due to its versatility in closed curve approximation. B-spline is a sophisticated tool widely used by the scientific and industrial community for approximating airfoil profiles from CMM data points [23, 31, 105-107]. Fitting a B-spline curve to data points requires parameterization of the points (i.e., computing the parameter value for each point) [108]. In order to be able to parameterize the points, the point sequence should be readily available or to be determined. The difference between the conventional 2D point set of CMM measurement and the projected set of the 3D scanned blade is that there is a sequence in the CMM data points, which makes it readily available for parameterizing the points for curve reconstruction. However, for the projected set of data points from the 3D scanned point cloud, the order of points is unknown and should be defined. Otherwise, it would not be possible to parameterize them for the subsequent curve fitting. The unorganized (unordered) set of projected data points is also scattered as can be seen in Figure 4.1(c), which makes the point ordering a challenge.

A prevalent method for 2D curve reconstruction from a given set of points is to fit a B-spline curve to the points by solving a global nonlinear optimization problem in which the algorithm starts with an initial B-spline curve (aka active curve) and then tries to iteratively minimize the error between the fitted curve and data points [53, 54, 109]. The optimization algorithms will converge properly only if a suitable initial curve sufficiently close to the target shape is given. Also, the final curve reconstruction result is sensitive to outliers, which makes pre-processing of the scattered set of data points essential to identify and remove the outliers.

Some studies have tried to smooth and skeletonize the unorganized set of data points and then fit an appropriate curve on smoothed and skeletonized data [65, 71, 72]. Cheng et al. [65] proposed an algorithm to reconstruct the polygonal closed curves from 2D noisy samples in which the noise of samples is filtered out using a clustering approach and estimating new points close to the underlying geometry, and then, new data points are decimated to avoid jagged polygonal curve. They employed NN-crust [66] algorithm to construct the output polygonal curve. In addition to the NN-crust method, some other methods mainly crust and β-skeleton [70] and HNN-crust [69] have been employed in the literature to generate the polygonal curve from 2D unorganized data. In general, the sampling density is an influential parameter on the polygon reconstruction from 2D datasets, which is defined based on the local feature size of data [70]. Lin et al. [71] reconstructed the curves from the planar unorganized point cloud using an interval B-spline curve. In their method, the curve order implied in the shape of the point cloud is determined by clustering the data points into a rectangle sequence. Then, the quasi-centric point sequence and the boundary curves of the point set are computed based on which a centric interval B-spline curve is generated as the final reconstructed curve. Wang et al. [72] generated the quadtree of the point set and smoothed the grid-like boundaries of the quadtree using a modified Laplacian method, then extracted the skeleton of the point set through the Voronoi diagram of the smoothed boundaries. All these methods need user interactions for selecting several parameters and thresholds in order to yield suitable results, therefore they are not fully automatic.

The moving least squares (MLS) method is another approach for smoothing and curve approximation from scattered data points [63]. The basic idea of MLS is to estimate the local underlying geometry of each point through a simple curve fitting to the neighboring points within the support domain of the point of interest and move the point onto the approximated curve. MLS technique is widely used for curve and surface reconstruction [64, 110-112]. Alexa et al. [111] and Fleishman et al. [112] employed the MLS method to model the surfaces with sharp features. The accuracy of MLS approximation significantly depends on the shape and size of the support domain, especially when the distribution of data points is not uniform, which is the case for scattered and noisy datasets. It is essential to eliminate the influence of outliers and measurement noise on local curve approximation to get reliable results. Lee [64] proposed an improved MLS technique to reconstruct a curve from the 2D unorganized data points in which the size of the support domain is specified based on covariance analysis of data points in order to prevent the adverse effects of unwanted points in the local curve fitting. Starting from a small radius of the support domain, the algorithm expands the region to get a suitable radius for which the correlation of data points within the support domain is larger than a pre-specified value. Then, using the MLS scheme, the 2D data points are iteratively thinned in order to satisfy a user-defined approximation error. It should be noted that the presented method by Lee [64] requires several user-defined parameters and thresholds that should be assigned properly to obtain reliable results. These parameter values to adjust highly depend on the profile geometry, noise, and density of the point set and the problem is that there is no benchmark to help find a reliable set of parameter values and thresholds by trial and error for different datasets. Therefore, the user-defined parameters make the existing methods not readily available for our application of airfoil profile reconstruction for computer-aided inspection of blades. In this application, automation is crucial.

The motivation of the present work is to propose an airfoil profile reconstruction method in which the projected noisy sectional data points (Figure 4.1(c)) are automatically thinned and ordered, and then the smooth profile is approximated by the B-spline curve fitted to them, as shown in Figure 4.1(d-f). The three steps of the proposed framework are outlined as follows:

1. *Thinning*: The aim of thinning is to reduce the sectional point cloud to a thin curve-like set of points that is locally close to the skeleton of the airfoil profile. We propose a recursive weighted local least squares (RWLLS) method to fit a curve on an adaptive local neighborhood of each sectional point and project the point onto the curve. In the present work, the fitting error of the fitted curve is deemed equivalent to the measurement uncertainty of the inspection data points. A progressive fitting domain growing scheme is proposed to generate the fitted local curve that meets the measurement uncertainty constraint. This scheme ensures the consistency of the local curve-fitting while enabling automation of the thinning process. The algorithm eliminates the effects of outliers using a weighting function. Another feature of the proposed approach is the

normal map filtering to ensure the consistency of the normal vectors of the points of the thinned dataset that are used in the next step for ordering the points.

2. *Ordering*: The ordering of data points is done by establishing the connectivity between the points of the thinned dataset. Using the normal at each point derived from the normal map filtering procedure, an initial profile polygon is generated. Then, the imperfect nodes are modified by the evaluation of the angular deviation of edges at each node. This procedure removes unreliable points and their corresponding edges from the profile polygon.

3. *Smooth profile reconstruction using B-splines*: Once the thinned and ordered set of data points is obtained, the smooth airfoil profile is generated by fitting a closed nonperiodic B-spline curve using the algorithm proposed in [84].

We demonstrate that the proposed three-step method can automatically reconstruct an accurate airfoil profile from the unorganized set of sectional data points with the typical levels of measurement noise and density of 3D scanned point cloud data.

4.3 Proposed Methodology

We explain the proposed profile reconstruction method in detail in subsections 4.3.2 and 4.3.3, but before that, we briefly explain the data borrowed from the previous steps of point cloud processing in subsection 4.3.1.

4.3.1 Preliminaries

The main input to the profile reconstruction algorithm is $\mathcal{S} = \{s_1, s_2, s_3, \dots, s_n\}$, the set of 2D section-specific points (Figure 4.1(c)) obtained from the 3D point cloud data $V = \{v_1, v_2, v_3, \dots, v_N\}$ via projection [9]. The dataset V is supposed to be a cleaned point cloud data obtained by performing pre-processing for outlier removal and denoising at the leading and trailing edges. We borrow some information about the local underlying geometry of the point cloud through the local neighboring points of the original point υ_i and the normal vector at the point υ_i. This information will be used in the next step to thin the projected dataset in the way that conforms to the underlying local geometry of the 3D point cloud. The local neighborhood (i.e., the set of neighboring points) NB(υ_i) of each original point υ_i of the 3D point cloud is established using the Territory Claiming (TC) algorithm [93]. The TC algorithm yields a directionally-balanced local neighborhood around the query point. Then, the normal vector $\overrightarrow{N_{\upsilon_i}}$ at υ_i is computed through local quadric surface fitting to the neighboring points. The normal vector estimation procedure is as follows: A generic quadric surface is fitted to the neighboring points of υ_i, the closest point υ_{i0} on the quadric surface to the point υ_i is found, the normal vector of the quadric surface at point υ_{i0} is calculated, and finally, the calculated normal vector is assigned back to the point υ_i [94]. For further details on local quadric surface estimation, readers are referred to [93]. The sectional normal vector set $\mathcal{N}_{\mathcal{S}} = \{\overrightarrow{N_{s_1}}, \overrightarrow{N_{s_2}}, \overrightarrow{N_{s_3}}, \dots, \overrightarrow{N_{s_n}}\}$ is then computed by the linear projection of the normal vector of each projected data point onto the sectional plane. For each sectional data point s_i (which has been the point υ_i before projection onto the plane), those points of the neighboring points NB(υ_i) that are projected onto the sectional plane are grouped to form the sectional neighborhood NB(s_i) of the point s_i.

4.3.2 Thinning

In this work, the concept of weighted local least squares (WLLS) is used to fit a simple curve to the data points in the local neighborhood of each point $s_i \in \mathcal{S}$ as the approximant of the local underlying geometry, and then thin the 2D scattered point cloud by moving the point s_i in the direction of the sectional normal vector $\overrightarrow{N_{s_i}} \in \mathcal{N}_{\mathcal{S}}$ to a new position on this estimated curve. We propose a recursive weighted local least squares (RWLLS) technique, in which an adaptive fitting domain is employed whose size is progressively increased to get a fitted curve with high conformity to the underlying geometry. Also, we propose a new weighting function to reduce the influence of noise and outliers on the curve fitting results. In the proposed method, at first, a curve is fitted on the minimum possible neighboring points (depending on the degree of the fitted polynomial), and then, the fitting domain (the number of neighboring points) gradually increases to approximate the underlying curve with more points. The curve fitting procedure is terminated when the fitted residuals meet the stopping threshold.

Figure 4.2 shows the flowchart of the proposed approach for thinning the sectional data points. The thinning process contains three main steps: 1) weighting of data points; 2) RWLLS curve fitting to the neighborhood of each point; 3) points projection to get the thinned dataset and normal map filtering to obtain a reliable normal vector at each point to use in the ordering step.

4.3.2.1 Weighting function computation

The presence of measurement noise and outliers in the sectional data points can make the locally fitted least-squares curve on the points of fitting domain deviate from the underlying geometry of the airfoil profile. We propose a new weighting function to reduce the influence of measurement noise and outliers on the curve fitting results. A weight factor is assigned to each sectional data point s_i based on the distance of the point to its sectional neighborhood $\mathrm{NB}(s_i)$ in the direction of normal $\overrightarrow{N_{s_i}}$. At first, the sectional neighboring points $\mathrm{NB}(s_i)$ are projected onto the line *l* at point s_i which is parallel to the sectional normal vector $\overrightarrow{N_{s_i}}$, as shown in Figure 4.3. If the projection of data points in $\mathrm{NB}(s_i)$ onto the line *l* is depicted by $\mathrm{NB}'(s_i)$, the neighborhood distance of the point s_i is defined as the average Euclidean distance of s_i to point cluster $\mathrm{NB}'(s_i)$ on the line *l* as follows:

$$\bar{d}(s_i) = \frac{1}{\left|NB'(s_i)\right|} \sum_{s'_j \in NB'(s_i)} \left\| s_i - s'_j \right\| \tag{4.1}$$

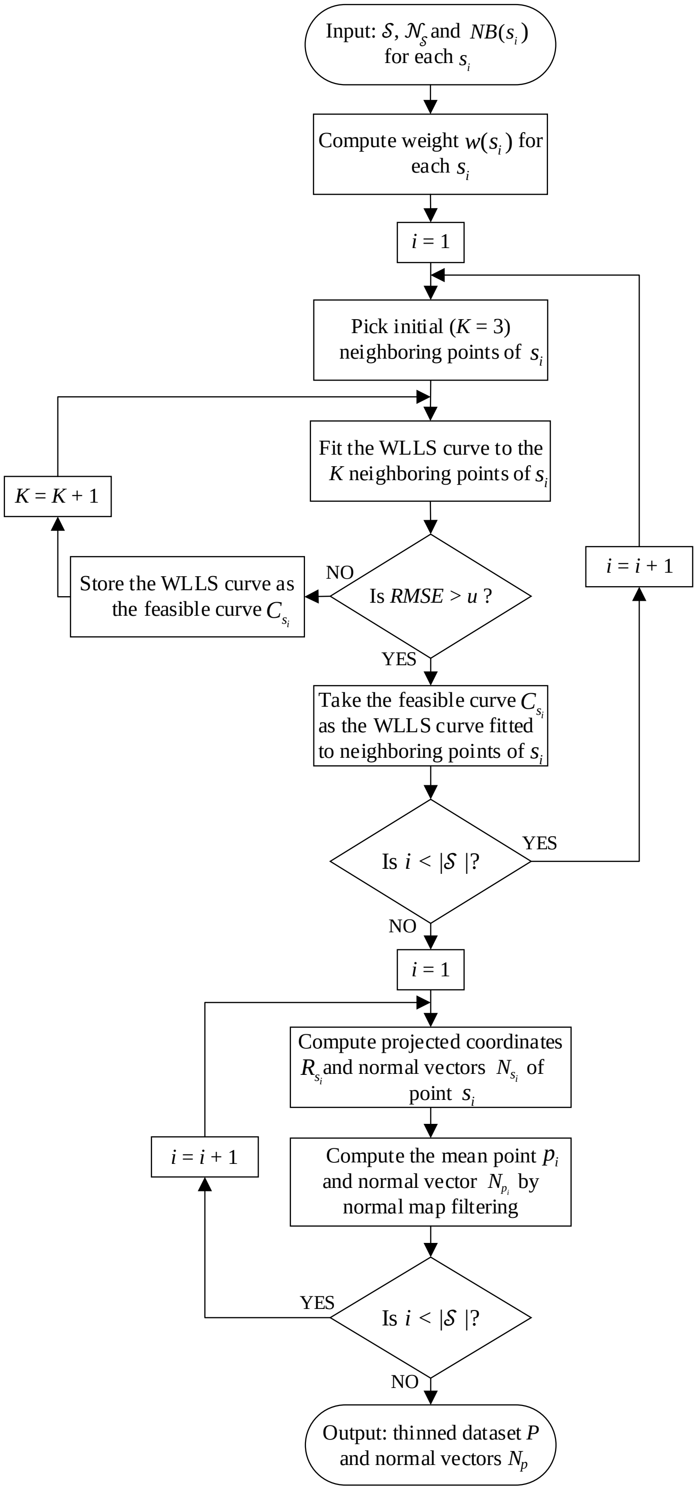

Figure 4.2 Flowchart of the proposed thinning process.

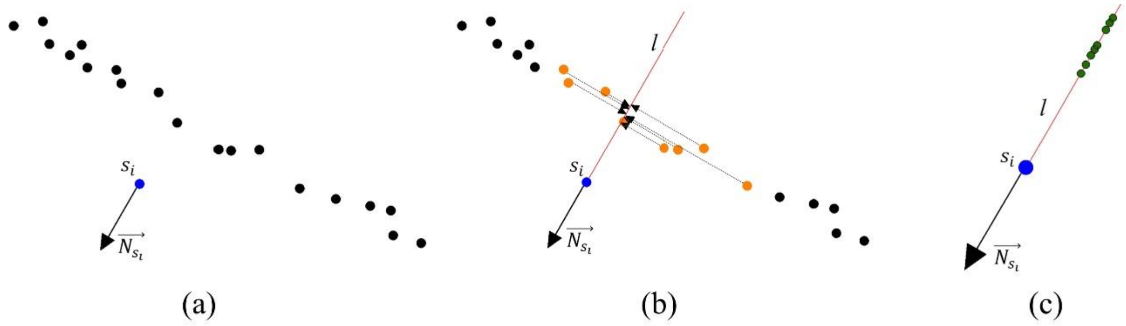

Figure 4.3 Illustration of weight factor computation. (a) For each sectional data point s_i and its normal vector $\overrightarrow{N_{s_i}}$, (b) all neighboring points are projected to the line *l* at point s_i. The line *l* is parallel to the normal vector $\overrightarrow{N_{s_i}}$. (c) The weight factor of point s_i is determined based on the distance of the point to its projected neighboring points cluster on the line *l*.

Then, the neighborhood inner distance is computed as the average distance between the sectional neighboring points of s_i in $\mathrm{NB}'(s_i)$:

$$\overline{D}(s_i) = \frac{1}{\left|NB'(s_i)\right|\left(\left|NB'(s_i)\right| - 1\right)} \sum_{s'_j, s'_k \in NB'(s_i), j \neq k} \left\| s'_j - s'_k \right\| \tag{4.2}$$

Finally, using the neighborhood distance $\bar{d}(s_i)$ and neighborhood inner distance $\overline{D}(s_i)$ the outlier factor $OF(s_i)$ value for point s_i is computed as:

$$OF(s_i) = \frac{\overline{d}(s_i)}{\overline{D}(s_i)} \tag{4.3}$$

If we regard the neighborhood of the point s_i roughly as local underlying geometry, the $OF(s_i)$ indicates how far the point s_i lies outside its local underlying geometry. The larger the $OF(s_i)$ is, the point s_i is more of an outlier. An exponential weighting function $w(s_i)$ is introduced to give weight to each sectional point based on its deviation from the local underlying geometry:

$$w(s_i) = \exp(\frac{-OF(s_i)}{\sigma_{out}}) \tag{4.4}$$

where σ_{out} is the standard deviation of outlier factor values of all points of the dataset $\mathcal{S}$. $w(s_i)$ is a value between 0 and 1. For a point s_i that is farther from the skeleton of the point set, the value of $w(s_i)$ is closer to 0. Employing this weighting function, the local curve fitting results will not be affected by outliers within the fitting domain.

4.3.2.2 Weighted local least squares (WLLS) approximation

At each point s_i, we fit a quadratic polynomial $\hat{f}(x) = c_1 + c_2 x + c_3 x^2$ to the fitting domain of s_i consisting of its K neighboring points $\{q_k = (x_k, y_k) | k = 1, \dots, K\} \in \mathcal{S}$ by finding the coefficients $\{c_1, c_2, c_3\}$ that minimize the following summation of weighted residuals [113, 114]:

$$\sum_{k=1}^{K} (\hat{f}(x_k) - y_k)^2 w(q_k) \tag{4.5}$$

Note that the weight $w(q_k)$ of each neighboring point is already computed by Equation (4.4) in the previous step. The algorithm begins with the smallest fitting domain containing the minimum possible nearest neighbors ($K = 3$) to fit a local least squares curve on the data points, and then refines the model gradually by adding one neighboring point at a time. In order to guarantee that the adaptive fitting domain is extended in both sides of the sectional normal direction of the query point, the k-nearest neighbors of the point are divided into two subsets using the sectional normal vector, and new fitting points are picked equally from each subset in terms of distance to the query point. By extension of the fitting domain (adding a new data point) it is required to update the least squares estimators. In this paper, the recursive least squares scheme is adopted for updating the least squares estimators in the WLLS method after adding a new sectional data point to the local curve fitting procedure. This increases the efficiency of the WLLS fitting process by avoiding more repetitive computations [115].

Considering that the scanned point cloud data is subject to measurement uncertainty, the actual point of each scanned data point is somewhere within a sphere centered at the measured point with the radius equal to the expanded uncertainty $3u$ (i.e., u is the standard uncertainty of the point cloud data) [9]. Having the data points and their associated set of uncertainty spheres directly projected onto the sectional plane, the sectional data points can be considered as points with a set of associated uncertainty circles centered at projected points with the radius equal to $3u$. The value of standard uncertainty u is given. For details on the given uncertainty value, readers are referred to [4]. In order to comply with the known uncertainty value of the point cloud data, in this study, the algorithm stops to extend the fitting domain for WLLS curve fitting when the root mean square value ($RMSE$) of the fitted residuals for the K neighboring points of the fitting domain gets larger than the standard uncertainty u of point cloud:

$$RMSE > u \tag{4.6}$$

In essence, the $RMSE$ value of the fitted residuals is equivalent to the standard deviation of normally-distributed fitted residuals. Therefore, as long as the $RMSE$ of fitted residuals is smaller than the standard uncertainty of the data points, the fitted curve is a feasible solution because it lies within the uncertainty interval (uncertainty circles) of points. In each iteration, when the $RMSE$ is smaller than standard uncertainty, the fitted curve is stored as the feasible curve C_{s_i} and the fitting domain is extended by adding a new neighboring point (i.e., the value of K increases to K+1). In the last iteration where the $RMSE$ of the fitted curve gets larger than u, the algorithm picks the feasible curve (C_{s_i}) stored in the previous iteration as the local curve fitted to the neighboring points of s_i and terminates the local curve fitting process (see Figure 4.2). As a result, the number of data points, *K*, within the fitting domain of sectional points is not fixed and varies for each sectional data point depending on the noise distribution, point spacing, and underlying geometry in the vicinity of that point.

4.3.2.3 Sectional data projection and normal map filtering

Each sectional point s_i is projected to its WLLS fitted curve in the normal direction. To ensure the smoothness of the resulting thinned dataset, it is required to make a connection between locally fitted curves. Besides, it is important to obtain a reliable normal vector at each point of the thinned dataset because the normal vector is used in the next step for ordering the data points and the consistency of normals affects the outcome of the ordering procedure. Thus, we generate a map of projections and normal directions based on all locally fitted curves containing the point of interest s_i within their fitting domain to make a connection between them and compute a final reliable normal vector at each point.

For each point s_i, the projection point s_i^0 and the unit normal vector $\overrightarrow{N_i^0}$ is approximated through fitting a local curve to the neighboring points in its fitting domain. Also, the point s_i could be included in the fitting domain of other sectional points for curve fitting. If the dataset $Q_{s_i} = \{ s_{1i}, s_{2i}, \ldots, s_{ji}, \ldots, s_{ri}\}$ $(s_{ji} = \{s \mid s \in \mathcal{S}, s_i \in \text{fitting domain of}\, s_j\})$ contains r sectional data points whose fitting domain contain the query point s_i, there exists a set of *r*+1 projection values $R_{s_i} = \{s_i^0, s_i^1, s_i^2, \ldots, s_i^j, \ldots, s_i^r\}$ and unit normal vectors $N_{s_i} = \{\overrightarrow{N_i^0}, \overrightarrow{N_i^1}, \overrightarrow{N_i^2}, \ldots, \overrightarrow{N_i^j}, \ldots, \overrightarrow{N_i^r}\}$ for the point s_i. Figure 4.4 shows WLLS fitted curves on the query point s_i (C_{s_i}) as well as on its neighboring points whose fitting domain include s_i $(C_{s_{1i}}, C_{s_{2i}}, \ldots, C_{s_{ri}})$. Figure 4.5(a) shows the projected coordinates and normal vectors for point s_i resulted from the local curves fitted on s_i.

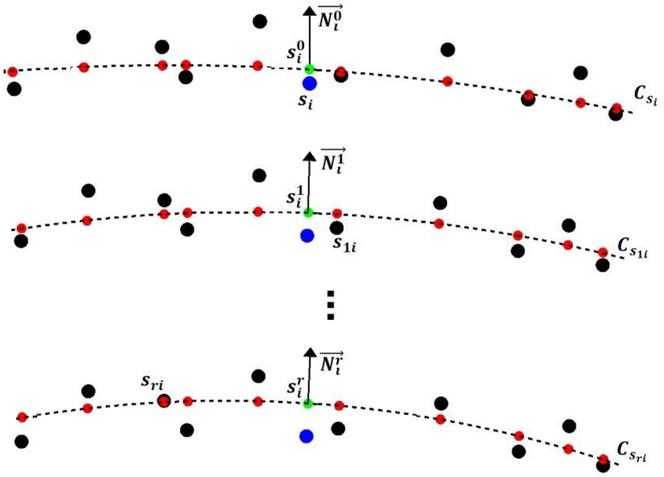

Figure 4.4 Projections and normal directions of point s_i after local curve fitting to the query point s_i and *r* sectional points whose adaptive fitting domain include the point s_i. Thus, we have *r*+1 projected coordinates (shown in green) and normal directions for point s_i.

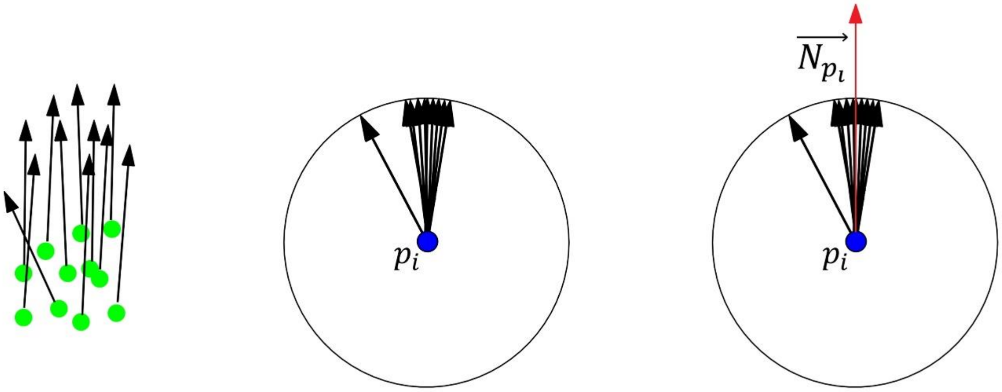

(a) (b) (c)

Figure 4.5 Normal map filtering: (a) After local curve fitting to point s_i and r sectional points whose fitting domain include point s_i, there are several projected coordinates and normal directions for s_i. (b) These coordinates and vectors are mapped into a unit circle whose center is the mean of the projected coordinates. (c) The center of the circle is the filtered thinned value of point s_i (denoted by p_i) for which the overall normal vector is $\overrightarrow{N_{p_i}}$.

To obtain the filtered unit normal direction, the projected points and normal vectors are mapped into a unit circle, called the normal map, as shown in Figure 4.5(b). The center of normal map circle, p_i, which is the mean value of projected data points in R_{s_i} is considered as the filtered thinned coordinate of the point s_i:

$$p_i = \frac{1}{(r+1)} \sum_{j=0}^{r} (s_i^j) \tag{4.7}$$

The overall normal direction $\overrightarrow{N_{p_i}}$ at the thinned point p_i, shown in Figure 4.5(c), is obtained iteratively by filtering the unit normal vectors in N_{s_i}. In each iteration, two normal vectors with the minimum angular difference are replaced with their summation. Using this approach, all normal vectors in the reliable direction (with small angular differences) are summed resulting in a vector with a large amplitude so that the effect of unreliable normal vectors (with a large angular difference) on the results will be negligible. As a result of averaging of projections and normal map filtering, the smoothness of the thinned dataset and the normal vectors will be improved.

4.3.3 Ordering

Once the previous step generates a sufficiently thin point cloud data $P = \{p_1, p_2, p_3, \ldots, p_n\}$ and corresponding normal vectors $N_p = \{\overrightarrow{N_{p_1}}, \overrightarrow{N_{p_2}}, \overrightarrow{N_{p_3}}, \ldots, \overrightarrow{N_{p_n}}\}$, we can order the points by arranging the connectivity of the data points. The flowchart of Figure 4.6 shows the proposed ordering process of thinned point cloud data via profile polygon generation. Point cloud ordering includes two main steps: initial profile polygon reconstruction and imperfect nodes modification.

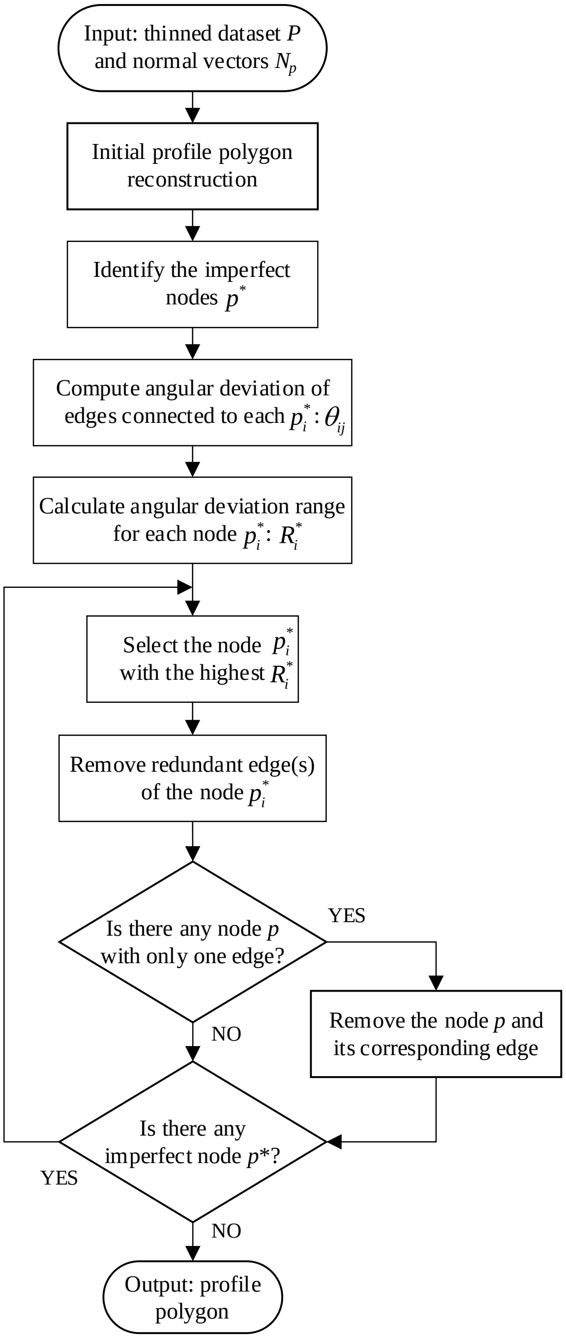

Figure 4.6 Flowchart of the proposed profile polygon reconstruction procedure for ordering thinned data points.

4.3.3.1 Initial profile polygon reconstruction

The normal map filtering method gives us a robust set of normal vectors N_p for thinned data points that can be effectively applied to establish directional connectivity between each point and its neighboring points. For each thinned data point p_i, the normal vector $\overrightarrow{N_{p_i}}$ divides the neighborhood into two regions H and H'. In each region, we take the nearest point to the query point p_i as adjoined points of point p_i. Figure 4.7(a) shows the adjoined points (in blue) of the thinned data point p_i (in red). Applying this procedure, the profile polygon is generated in which each point is connected to its adjoined points through two edges. Ideally, each node of the generated profile polygon should include exactly two incident edges. However, in practice, a few points away from the underlying geometry can lead to polygon loops. In this case, as can be seen in Figure 4.7(b-d), some polygon nodes, called imperfect nodes, contain more than two edges. To avoid polygon loops, it is essential to modify the connections of imperfect nodes and remove their corresponding redundant edges from the reconstructed profile polygon.

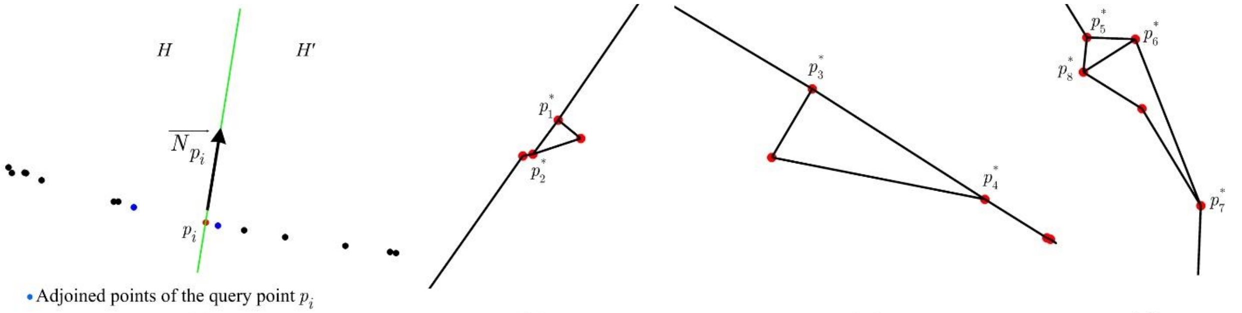

(a) (b) (c) (d)

Figure 4.7 Profile polygon generation: (a) Using the normal vector of thinned points obtained by normal map filtering, each point p_i is connected to its adjoined points in two sides of the normal direction. (b), (c) and (d) show cases of imperfect nodes (p_1^* to p_8^*) after profile polygon reconstruction. These nodes should be modified to get a reliable profile polygon.

4.3.3.2 Imperfect nodes modification

For the profile polygon formed by dataset $P = \{p_1, p_2, p_3, \dots, p_n\}$ and the edge set $E = \{e_1, e_2, e_3, \dots, e_m\}$ $(m \geq n)$, the incident edge set $e(p_i)$ is the set of edges that the point p_i shares with other points: $e(p_i) = \{\, e_{ij} = (p_i, p_j) | e_{ij} \in E, p_j \in P, p_i \in P\}$. The imperfect nodes p^* are the vertices (nodes) with more than two incident edges: $I = \{p^* \mid |e(p^*)| > 2, p^* \in P\}$.

To modify the connections of imperfect nodes, a parameter is specified to compute the deviation of incident edges of each imperfect node from the underlying curve and remove the edge(s) with a larger deviation. The angular deviation (θ_{ij}) of each edge e_{ij} of the imperfect node p_i^* from the underlying curve is computed as the angle between the edge vector $\overrightarrow{e_{ij}}$ and the tangent vector $(\overrightarrow{T_{p_i^*}})$, which is perpendicular to the normal vector $\overrightarrow{N_{p_i^*}}$:

$$\theta_{ij} = \mathrm{acos}\left(\frac{\vec{e}_{ij} . \vec{T}_{p_i^*}}{\left|\vec{e}_{ij}\right| . \left|\vec{T}_{p_i^*}\right|}\right) \tag{4.8}$$

Therefore, for each imperfect node p_i^*, there is a set θ_i^* containing the angular deviation values for all edges in the edge set $e(p_i^*)$.

The algorithm gives priority to modifying the nodes with higher angular deviations. We compute the angular deviation range R_i^* for each imperfect node p_i^* as follows:

$$R_i^* = \max(\theta_i^*) - \min(\theta_i^*) \tag{4.9}$$

Then, the imperfect nodes are sequenced in descending order of R_i^* values. That is, we first modify the imperfect nodes with higher R_i^* values and remove the edges with more deviation from underlying geometry as redundant edges. The node modification procedure is as follows:

1) In each region H and H′ around p_i^*, constructed by the normal vector $\overrightarrow{N_{p_i^*}}$, the edge with the smallest angular deviation value θ_{ij} is selected as a valid edge and other edges are removed as redundant edges.

2) If there is any node with only one edge, the node and its corresponding edge are considered as redundant elements and removed from the airfoil polygon.

The algorithm continues to modify the nodes from the highest R_i^* value to the lowest one. Finally, the algorithm terminates modification when there is no imperfect node with more than two incident edges.

Figure 4.8 illustrates the modification of the imperfect node p_i^* with 3 incident edges $(p_i^*, q_1), (p_i^*, q_2)$ and $(p_i^*, q_3),$ namely e_{i1}, e_{i2}, e_{i3}. As can be seen in Figure 4.8(b) and Figure 4.8(c), the edge (p_i^*, q_1) in the region H and (p_i^*, q_3) in the region H' are selected as valid edges for node p_i^* and the edge (p_i^*, q_2) is removed from the reconstructed polygon. By eliminating redundant edge (p_i^*, q_2), the data point q_2 contains only one edge; thus, the algorithm removes the point q_2 and its corresponding edge (q_2, q_3) from the airfoil profile polygon.

Figure 4.9 shows the 3 cases of imperfect nodes and modification results for each of the nodes. It is seen that the proposed method can precisely remove the redundant points and their corresponding edges from the polygon dataset of the airfoil profile.

After establishing the connectivity of the thinned dataset of points through the generated polygon, points that are excluded from the polygon are removed from the thinned dataset. The remaining points are the nodes of the polygon, which are readily ordered in a proper sequence.

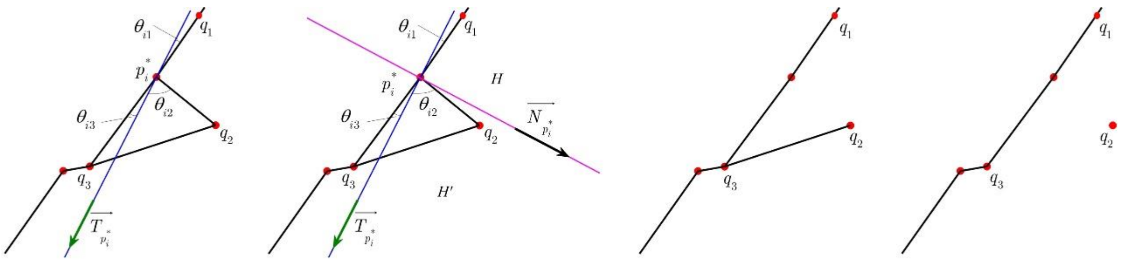

(a) (b) (c) (d)

Figure 4.8 Imperfect nodes modification: (a) For edges of the imperfect node p_i^* the angular deviations θ_{i1}, θ_{i2} and θ_{i3} are computed. (b) Then, in each region H and H', constructed by the normal vector $\overrightarrow{N_{p_i^*}}$, the edge with the smallest angular deviation value is selected as a valid edge (edges (p_i^*, q_1) and (p_i^*, q_3)), and (c) the redundant edge (p_i^*, q_2) is removed. (d) In the profile polygon, if there is any node (q_2) with only one edge, the node and its corresponding edge are removed from the polygon.

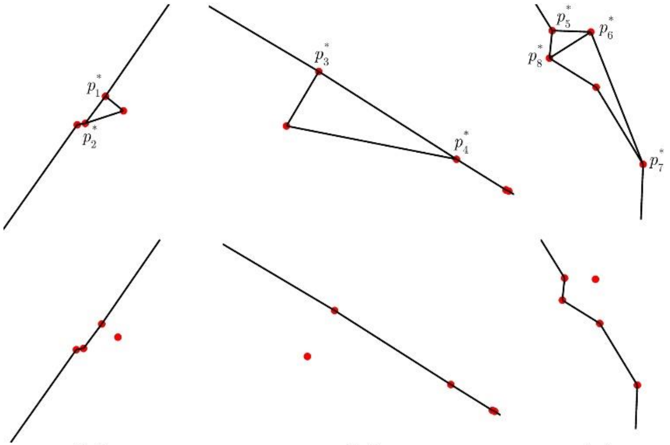

(a) (b) (c)

Figure 4.9 Modification of imperfect nodes of Figure 4.7.

Finally, we generate the smooth airfoil profile from the ordered data points using the B-spline curve fitting method of Khameneifar and Feng [84]. Given the set of ordered data points, a C^2-continuous closed non-periodic cubic B-spline curve is computed through curve approximation to best fit the data points while employing the smallest possible number of curve segments to avoid unwanted undulations. For a given number of curve segments, the B-spline curve fitting approach involves four main steps: (1) the start point is selected as the point with minimum curvature variance along the airfoil profile, (2) the parameter value for each data point is computed through chord length parameterization method [116] starting from the selected start point, (3) the knot vector is generated using the knot placement method by De Boor [117] to compute the B-spline basis functions, and (4) the least-squares minimization problem is solved to calculate the set of control points of the B-spline curve. Once the control points are computed, the B-spline curve is obtained. The minimum possible number of control points to construct a closed cubic B-spline curve of C^2 continuity is six, which means that at least three curve segments are needed to construct such a piecewise composite curve. Therefore, the progressive curve fitting algorithm starts with a curve composed of three segments (six control points). The resulting fitted curve is then checked against the feasibility condition. The feasibility condition is that the RMS of the fitted residuals must be smaller than the standard uncertainty of data points. If the feasibility condition is not met, one more curve segment (control point) is added and a new curve is fitted. This iteration continues until the feasibility condition is satisfied. For details on the applied B-spline curve fitting method, readers are referred to [84].

4.4 Results and Discussion

4.4.1 Simulated input data

Numerical case studies have been conducted to validate the proposed method. For such validation, we use synthetic point cloud data generated by sampling a simulated in-service blade. This is because actual airfoil profiles of the simulated blade are known that can be used as the benchmark against which the airfoil profile reconstruction outcomes can be compared to assess the performance of the proposed algorithm. The blade CAD model was created with the overall dimensions of the blade roughly corresponding to a cuboid of 45 mm in length, 15 mm in width, and 105 mm in height. To follow a typical blade surface design, a twist of 25 degrees from the blade bottom to tip was introduced by incrementally twisting the airfoil sections from the bottommost to the topmost section. To simulate the in-service blade surface, certain form deviations were superimposed onto the nominal blade surface. First, a sinusoidal variation with the random amplitudes between 0 and 0.005 mm was superimposed onto the airfoil sections of the CAD model in the direction of the profile normal to emulate the combination of the typical manufacturing errors on the blade surface. Then, a sinusoidal variation with the amplitude of 0.09 mm was added to a portion of the pressure and suction sides of the blade close to its tip to resemble a typical geometric deformation on a used blade during its service. Using the NURBS surface interpolation of the airfoil sections, the simulated in-service blade surface was created, which is then used as a reference. Figures 4.10(a) and 10(b) respectively show the nominal CAD model and the simulated in-service blade with its error colormap with respect to the nominal CAD model.

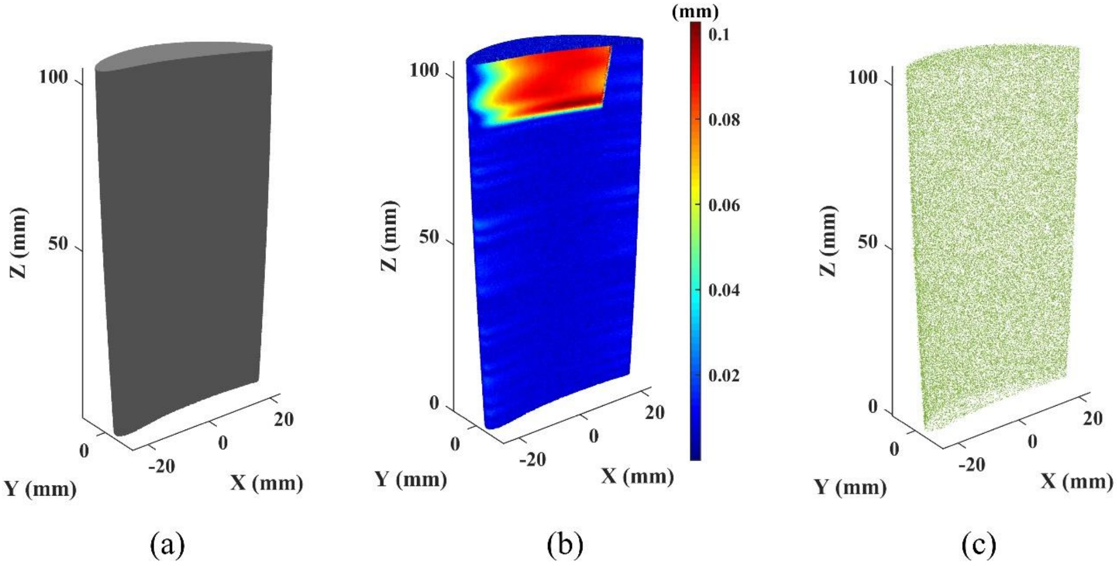

(a) (b) (c)

Figure 4.10(a) Nominal CAD model of the blade, (b) error colormap of the simulated in-service blade, and (c) synthetic point cloud with a noise level of 0.015 mm and point spacing of 0.1 mm.

Next, the simulated in-service blade surface was randomly sampled to generate an ideal (noise-free) point cloud. In practice, the scanned point cloud data contain measurement noise. Therefore, the synthetic point clouds should also include the measurement noise for simulating the real scanned point cloud data. In order to generate noisy point clouds of the simulated blade, Gaussian deviates with different levels of known standard deviation (with the distribution's mean at zero for all cases) were superimposed onto the ideal point cloud in random directions. In the present work, the superimposed Gaussian deviates generate point clouds with the standard deviation of noise (i.e., standard uncertainty) from 0.01 mm to 0.03 mm, which is the typical range of noise observed on scanned point clouds according to the recent studies on the metrological performance of 3D scanners [98].

The density of the scanned point cloud data is another influential factor in the airfoil profile reconstruction results. In the present work, we generate noisy point clouds of the simulated blade with various density levels. The average point spacing between the data points (aka resolution) is set from 0.1 to 0.2 mm, which is the typical range of resolution of point clouds obtained by optical 3D scanners. Table 4.1 lists the noise levels and the point spacing values of the generated point clouds in this work. The proposed profile reconstruction method is tested on 250 sets of point cloud data with 5 various noise levels and 5 point spacing values (10 sets for each type). Figure 4.10(c) shows the synthetic point cloud of the blade with 0.015 mm standard deviation of noise and point spacing of 0.1 mm.

To comprehensively evaluate the performance of the proposed method in both deformed and non-deformed regions of the in-service blade, the airfoil profile is reconstructed for three profiles, namely the innermost, intermediate and outermost airfoil sections of the blade at Z = 7 mm, Z = 52.5 mm, and Z = 98 mm, respectively. The actual airfoil profiles of the simulated blade are known for the three sections.

For each of the 250 sets of point clouds (10 sets of each noise level and point density), the sectional data points for Z = 7 mm, Z = 52.5 mm, and Z = 98 mm sections were obtained by applying the method of [9] to project the nearby data points onto each specified sectional plane. Each set of acquired sectional data points is an input to the profile reconstruction algorithm.

Table 4.1 Range of noise level and point spacing of the generated synthetic point cloud data.

Parameter	Range
Noise level (mm)	0.01, 0.015, 0.02, 0.025, 0.03
Point spacing (mm)	0.1, 0.125, 0.15, 0.175, 0.2

4.4.2 Profile error evaluation

To assess the accuracy of the proposed profile reconstruction method, a comparison is made between the reconstructed airfoil profile and the actual profile. As an example, Figure 4.11 shows the profile reconstructed from sectional data points and the known actual profile at the leading edge (LE), trailing edge (TE), suction side (SS), and pressure side (PS) of the airfoil for the outermost airfoil section of the blade. The point cloud of Figure 4.11 was one of the point clouds with the point spacing of 0.1 mm and the noise level of 0.015 mm. As can be seen in the figure, the proposed method effectively removes the influence of outliers and noise on the profile reconstruction procedure and there is a high degree of conformity between the reconstructed airfoil profile and the actual one. The computation times of the three main steps of the proposed method namely thinning, ordering, and B-spline curve fitting procedures for reconstruction of the airfoil profile shown in Figure 4.11 are listed in Table 4.2. Test computations were carried out in MATLAB R2018a on a PC with a 3.6 GHz Intel Core i7-7700 processor and 32 GB of RAM without parallel computing. It is seen that the thinning process is the most time-consuming step of the algorithm because of the iterative weighted local least squares curve fitting procedure employed for each sectional data point. Figure 4.12 shows the deviation of the reconstructed airfoil profile from the corresponding actual profile for noise levels and point spacings listed in Table 4.1. Each plotted value in Figure 4.12 is the mean value of profile deviation in innermost, intermediate, and outermost airfoil sections (mean of 30 profile deviations). The error bars represent the standard deviation of profile errors. Table 4.3 presents the maximum deviation of the reconstructed profiles from their corresponding actual profiles for different levels of noise and point spacing.

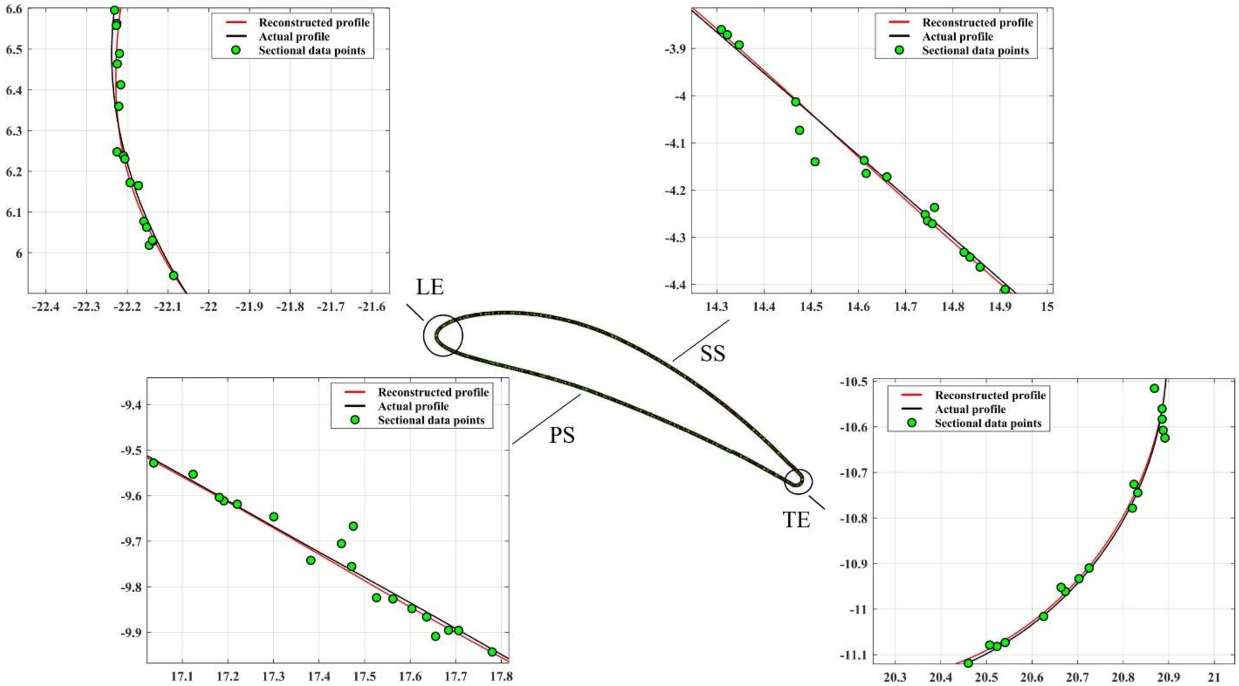

Figure 4.11 Actual and reconstructed airfoil profiles and sectional data points at the leading edge (LE), trailing edge (TE), suction side (SS), and pressure side (PS) of the outermost airfoil section of the blade (i.e., the deformed region of the blade). The noise level and point spacing of the point cloud data are 0.015 mm and 0.1 mm, respectively. The unit of the plots is mm.

Table 4.2 Computation time of the proposed algorithm for the case shown in Figure 4.11.

No. of data points	Thinning (s)	Ordering (s)	B-spline curve fitting (s)	Total (s)
1,685	34.28	0.24	1.83	36.35

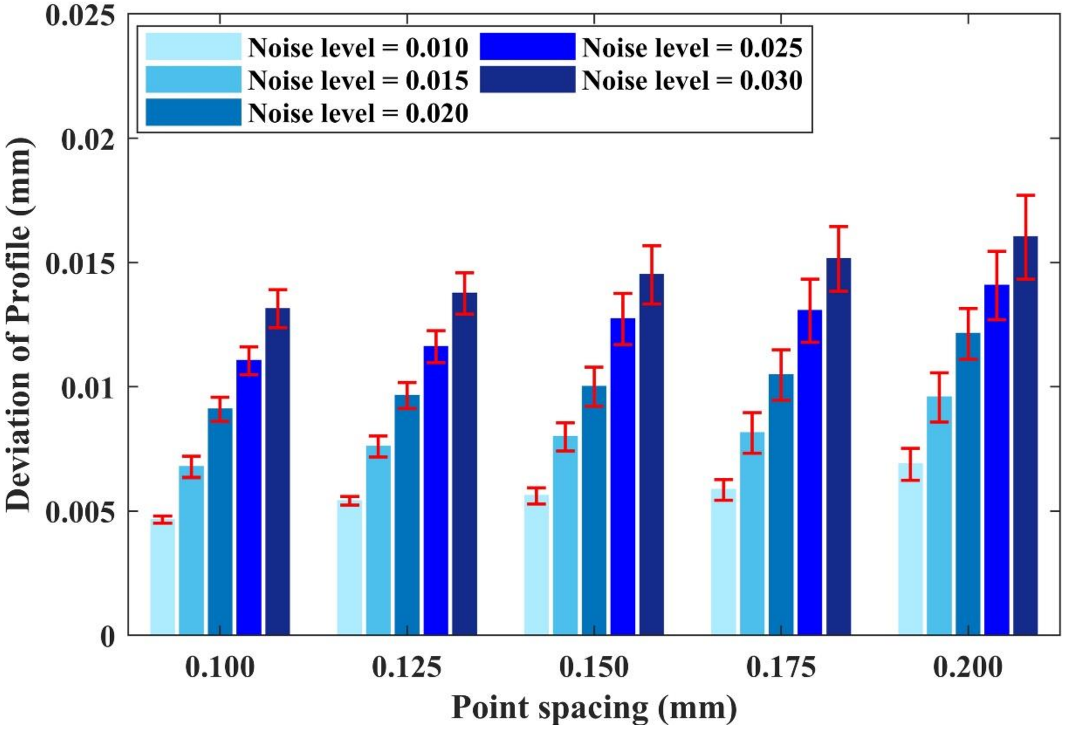

Figure 4.12 Deviation of the reconstructed airfoil profile from the actual airfoil profile for different levels of noise and point spacings. Each displayed value is the mean of profile deviations in innermost, intermediate, and outermost airfoil sections. The error bars represent the standard deviation of profile errors. The unit of noise levels is mm.

As expected, by increasing the noise level and point spacing the reconstructed airfoil profile deviates more from the actual profile. It should be noted that when the point spacing of the point cloud data is increased, farther points are projected onto the sectional plane and the projection uncertainty will increase [9]. Thus, projected sectional data points deviate more from the original underlying geometry. In addition to noise level and point density, the underlying geometry of the sectional data points is another key element affecting the accuracy of the reconstructed airfoil profile.

Table 4.3 Maximum deviation (in mm) of the reconstructed airfoil profile from the actual profile for different levels of noise and point spacing.

Point spacing (mm)	Noise level (mm)				
	0.010	0.015	0.020	0.025	0.030
0.100	0.016976	0.019402	0.041759	0.064732	0.073552
0.125	0.019125	0.023564	0.046539	0.071692	0.080025
0.150	0.022031	0.029395	0.051464	0.077300	0.087039
0.175	0.025457	0.034121	0.058532	0.081763	0.096462
0.200	0.030882	0.043750	0.075263	0.094395	0.110774

Around the trailing edge and leading edge, where the curvature of the underlying geometry is high, both the weighted local least-squares fitting and normal map filtering results are more sensitive to the noise and point spacing of the point cloud data. For sparser and noisier sectional data, the fitted local curves in the high-curvature regions are less precise; and consequently, the normal vectors computed for normal map filtering at the high-curvature regions are less accurate than those of the less-curved regions. That is, the airfoil profile reconstructed by the proposed algorithm deviates more from the actual profile in the leading and trailing edges than the suction and pressure sides.

As mentioned earlier, the accuracy of the reconstructed airfoil profile is particularly important in the evaluation of the position and orientation errors of airfoil sections. For evaluating the position error of each airfoil section, the centroid location of the reconstructed airfoil profile is calculated, because its deviation from the reference CAD centroid position will be compared to the specified position tolerance to decide whether the airfoil section is in-tolerance for the position tolerance. Then, the reconstructed profile is translated to share the same centroid with the CAD profile, and a rotation-only rigid body transformation best matches the reconstructed profile to the CAD profile to estimate the orientation of the airfoil profile, which is compared to the specified orientation tolerance to decide whether the airfoil section conforms to the orientation tolerance. Details of the evaluation of position and orientation errors of airfoil sections can be found in [6].

The centroid location and the orientation angle of the airfoil profile were computed based on the reconstructed profiles for the aforementioned innermost, intermediate, and outermost airfoil sections and compared to their corresponding actual values known for the simulated blade. Figure 4.13 and Figure 4.14, respectively, show the deviation of the estimated centroid location and orientation angle based on the reconstructed airfoil profile from their actual values for different levels of noise and point spacing. Again, the plotted values are the mean values of deviations for innermost, intermediate, and outermost sections (mean of 30 deviations) and error bars represent the standard deviations.

It is seen in Figure 4.13 and Figure 4.14 that the evaluated centroid location and orientation angle become less reliable with higher noise levels and point spacings. The reliability of the estimated centroid location and the orientation angle is crucial for preventing false rejection (or acceptance) of geometrically acceptable (or unacceptable) blades as well as preventing incorrect modifications to the related manufacturing process or incorrect process planning for the repair of in-service blades. The maximum value of absolute error in the estimated centroid location and orientation angle should not be larger than the Maximum Permissible Error (MPE) in order for the estimated features to be considered reliable for the evaluation of the position and orientation tolerances. As a generally accepted rule-of-thumb in industry, the ratio of MPE to the tolerance value is 1:10. The specified position and orientation tolerances of the airfoil sections of the blade used in this study are 0.025 mm and 0.09 degrees respectively. Therefore, the MPE value of the estimated centroid location is 0.0025 mm, and the MPE value of the estimated orientation angle is 0.009 degrees. Tables 4.4 and 4.5, respectively, present the maximum error of the estimated centroid location and orientation angle based on the reconstructed airfoil profile from their actual values for different levels of noise and point spacing.

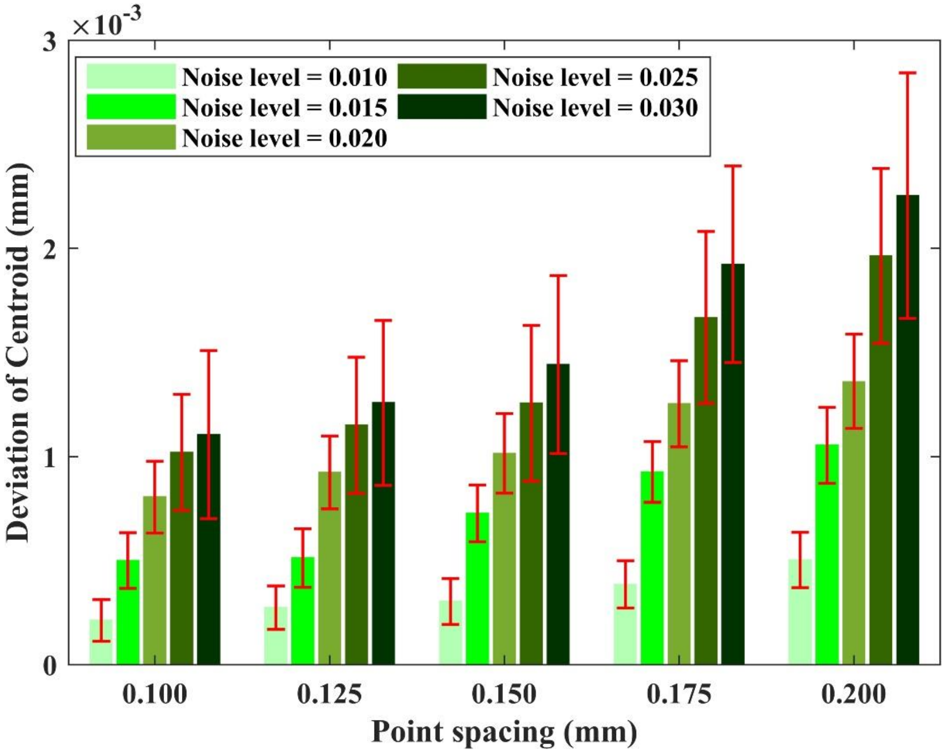

Figure 4.13 Deviation of the computed centroid location from its reference location for different levels of noise and point spacings. Each displayed value is the mean of deviations and error bars represent the standard deviations. The unit of noise levels is mm.

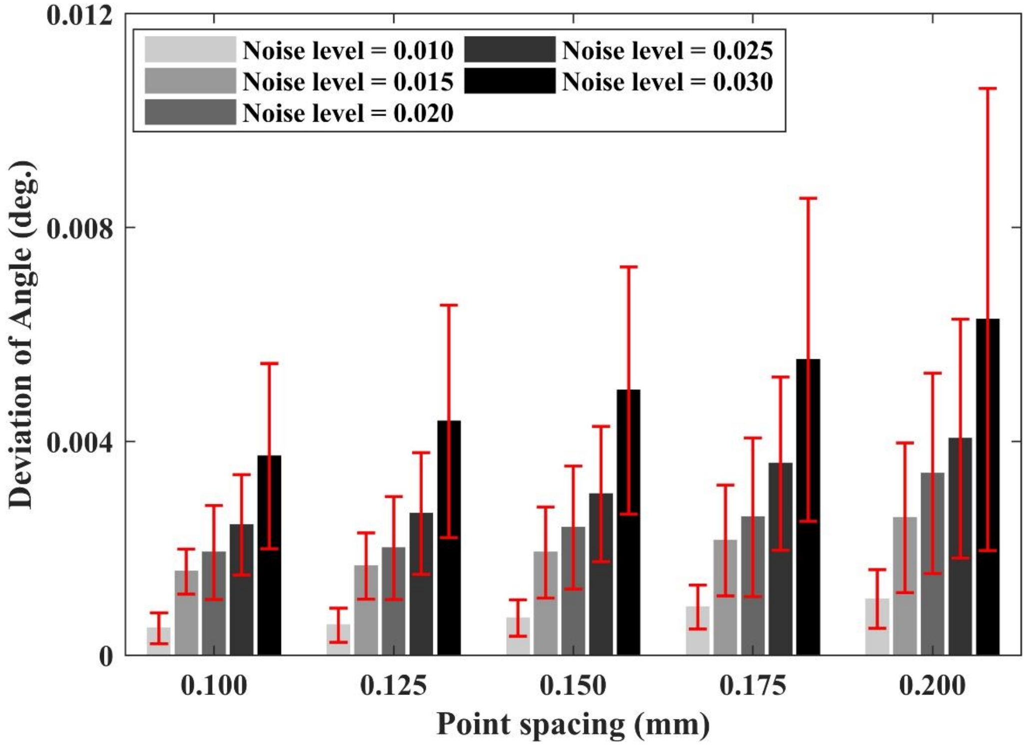

Figure 4.14 Deviation of the calculated orientation angle from its reference value for different levels of noise and point spacings. Each displayed value is the mean of deviations and error bars represent the standard deviations. The unit of noise levels is mm.

Table 4.4 Maximum deviation of the computed centroid location (mm) from its reference location for different levels of noise and point spacings.

Point spacing (mm)	Noise level (mm)				
	0.010	0.015	0.020	0.025	0.030
0.100	0.000428	0.000753	0.001088	0.001594	0.001721
0.125	0.000485	0.000810	0.001210	0.001685	0.001867
0.150	0.000546	0.000951	0.001574	0.001992	0.002213
0.175	0.000625	0.001127	0.001606	0.002285	0.002664
0.200	0.000703	0.001356	0.001747	0.002518	0.003207

Table 4.5 Maximum deviation of the calculated orientation angle (deg.) from its reference value for different levels of noise and point spacings.

Point spacing (mm)	Noise level (mm)				
	0.010	0.015	0.020	0.025	0.030
0.100	0.001192	0.002037	0.003592	0.004732	0.007528
0.125	0.001245	0.002713	0.004127	0.005602	0.008364
0.150	0.001536	0.003615	0.004635	0.005718	0.008771
0.175	0.001791	0.004244	0.006621	0.007310	0.011120
0.200	0.002133	0.005614	0.007105	0.009162	0.014698

By comparing the values of Tables 4.4 and 4.5 with the MPE values of the estimated centroid location and orientation angle, it is concluded that in this particular case study, for the noise levels equal to or less than 0.030 mm, reasonably dense point clouds with an average point spacing not larger than 0.150 mm (average point density not lower than 44 points/mm^2) are appropriate and result in accurate reconstructed profile and satisfactory estimated features. The datasets with an average point spacing up to 0.175 mm (average point density not lower than 33 points/mm^2) are permissible for the noise levels up to 0.025 mm, and the datasets with an average point spacing up to 0.200 mm (average point density not lower than 25 points/mm^2) are permissible for the noise levels up to 0.020 mm. The use of the datasets with 0.025 mm noise level and 0.200 mm point spacing, as well as the datasets with 0.030 mm noise level and point spacing over and equal to 0.175 mm must be avoided because for those datasets the maximum errors of both the estimated centroid location and orientation angle are larger than their corresponding MPE values.

The results suggest that it is essential to employ sufficiently dense point cloud data with a reasonable level of noise to be able to guarantee the accuracy of profile reconstruction and feature estimation. This further emphasizes the importance of pre-processing of point cloud data, especially for noise reduction, as well as other effective solutions like data fusion to improve the quality of acquired point cloud data in terms of noise and density. The current metrology-grade 3D scanners provide us with point cloud data in the range of density and noise that is deemed permissible for the case study presented in this paper. The minimum required density and maximum tolerable noise depend on the geometry.

The presented numerical simulation scheme for validation can be likewise employed to find the limits of allowable point cloud density and noise for any other specific airfoil geometry based on maximum permissible errors.

4.5 Conclusions

An accurate and automatic method for airfoil profile reconstruction from unorganized noisy sectional data points of scanned blades has been presented in this paper. The essential contribution of the proposed method lies in automatically thinning the noisy set of sectional data points within the measurement uncertainty constraint of inspection data using a recursive weighted local least squares technique and generating a reliable profile polygon from thinned data to order the dataset with no user interaction. After thinning and ordering the unorganized set of sectional data points, the smooth airfoil profile was generated by fitting a closed nonperiodic B-spline curve on the ordered data. The implementation results from various case studies on synthetic point clouds of a simulated in-service blade have demonstrated the effectiveness of the proposed method in reliably thinning and ordering the sectional data and eliminating the adverse effects of outliers and noise on the reconstructed airfoil profile. The results have substantiated the accuracy and consistency of the proposed method for airfoil profile reconstruction from data points with the typical levels of noise and density of 3D scanned point clouds.

The proposed airfoil profile reconstruction method enables accurate estimation of the centroid location and orientation angle of airfoil sections, which has a high practical significance for precision inspection of aero-engine blades using non-contact 3D scanning techniques. Moreover, the application of the proposed airfoil profile reconstruction method is not limited to quality inspection, as it can be equally used in other applications that benefit from airfoil profile reconstruction, including repair and adaptive machining of aero-engine blades [14, 25, 118].

Chapter 5 ARTICLE 3: CONSTRUCTION OF DAMAGE-FREE DIGITAL TWIN OF DAMAGED AERO-ENGINE BLADES FOR REPAIR VOLUME GENERATION IN REMANUFACTURING

Hamid Ghorbani, Farbod Khameneifar

Submitted to the *Robotics and Computer-Integrated Manufacturing, November 25, 2021*

5.1 Abstract

Accurate repair volume generation from 3D scan data of damaged aero-engine blades is of great importance in additive or hybrid remanufacturing for restoring the blades to a like-new condition. In addition to material-missing damages, the blade's surface also deforms due to working in harsh environments, which makes it deviate from the nominal design geometry. Therefore, the Boolean operation between the nominal CAD model and the scanned point cloud of the damaged blade does not yield an accurate repair volume. This paper presents a new methodology to construct an accurate damage-free digital twin model of the defective blades that contains the deformations of the blade's undamaged regions. The Boolean difference between the scan data of the damaged blade and its damage-free digital twin yields the repair volume with a smooth geometric transition at the interface of the repair patch and unrepaired regions. At first, the data points of damaged regions of the blade surface are detected and eliminated from the scan through a region growing segmentation. Then, a CAD-to-scan non-rigid registration algorithm deforms the nominal CAD model of the blade to best match it to the scanned point cloud in the undamaged regions. The non-rigid registration algorithm iteratively minimizes the distance between two datasets under the local rigidity constraint to avoid shrinkage and expansion of the deformed CAD model. A constrained point-to-surface weighted correspondence search method is proposed to reduce the influence of

noise and unreliable correspondences on the non-rigid registration. The results of numerical and experimental case studies have demonstrated that the proposed method is accurate and robust to noise, and it can be effectively applied to construct a damage-free digital twin model for repair volume generation.

5.2 Introduction

Operating in high temperature and pressure environments, aero-engine blades are likely to be damaged and deformed from their design geometric shapes over time. Since blades are made of expensive and difficult-to-cut materials requiring high financial cost of requisite manufacturing processes, the remanufacturing of damaged blades is of great interest for the maintenance, repair, and overhaul (MRO) industry to extend the service life of blades [1]. In general, the remanufacturing process starts with measuring the surface of the damaged blade using contact or non-contact measurement instruments to capture the geometry of the blade in the form of point cloud data. Non-contact data acquisition using optical 3D scanners is preferred, as 3D scanners can quickly capture high-density point clouds [3]. Once the damaged blade is scanned, the captured point cloud is often compared to the nominal model to extract the material-missing regions and obtain the repair volume for additive restoration using directed energy deposition (DED) process. A secondary CNC machining/grinding process is required to remove excess material remaining on the deposited blade [14]. The crucial factor in remanufacturing of damaged blades is that the repaired blade must preserve its original geometric shape within certain tolerances specified on the nominal model as well as provide a smooth continuity between repaired and unrepaired regions [119]. Due to extreme working conditions, in addition to material missing type damages, the geometric deformations happen on the surface of aero-engine blades in undamaged regions such as distortion, expansion, and contraction [15]. Thus, the nominal CAD model or the reverse engineering-based (RE-based) model reconstructed from the scan data of an intact (newly-manufactured) blade no longer represent the current geometric shape of the defective blade. To yield an accurate representation of the repair volume with a smooth continuity between repaired and unrepaired regions, it is essential to compare the 3D scanned point cloud of the defective blade with its damage-free digital twin. The damage-free digital twin of the defective blade is a 3D model of the current state of the blade without material-missing damages while containing the geometric deformations on the undamaged areas.

Figure 5.1 shows the outline of 3D scanning-based repair volume generation for damaged aero-engine blades in the presence of the nominal CAD model of the blade. A novel methodology is proposed in this paper to construct a damage-free digital twin of the damaged blade through CAD-to-scan non-rigid registration. As illustrated in Figure 5.1, the framework proposed in this work for repair volume construction of damaged blades mainly includes three steps: 1) Scan-to-CAD rigid registration to bring the measurement data into a common coordinate system with the CAD model, 2) CAD-to-scan non-rigid registration to gradually deform the CAD model to match with the scanned data and obtain a damage-free digital twin of the defective blade, and 3) Boolean operation between the constructed damage-free digital twin and the scan data to yield the parameterized geometric representation of the repair volume.

Initially, as illustrated in Figure 5.1, the scanned point cloud data of the damaged blade and its nominal CAD model lie in two different coordinate systems namely measurement coordinate system (MCS) and design coordinate system (DCS). Before comparison of two datasets, a scan-to-CAD rigid registration is required to bring the scan data to a common coordinate system with the CAD model. The Iterative Closest Point (ICP) algorithm [8] and its variants [38, 41] are widely used for the global rigid registration of the scanned point cloud data of blades [28, 29, 33].

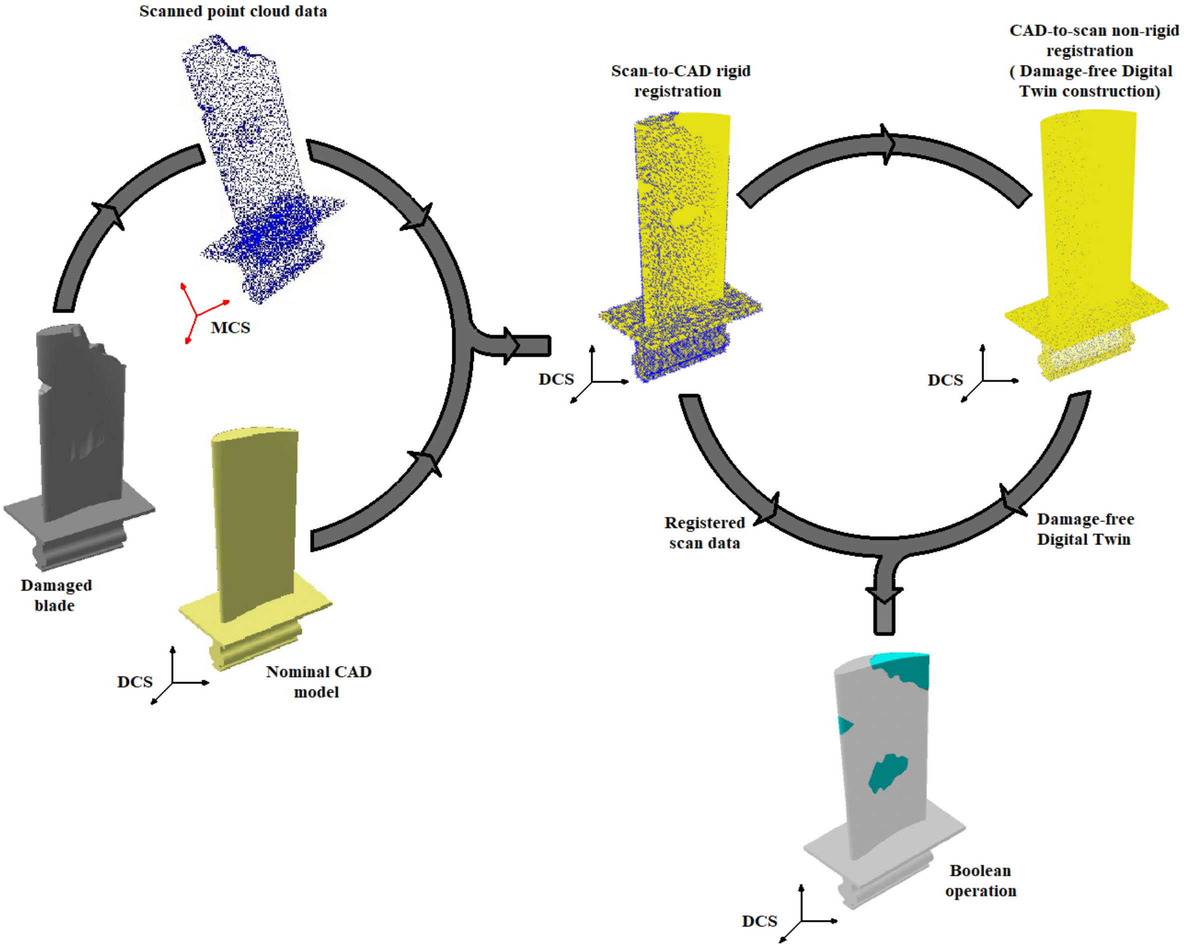

Figure 5.1 Outline of 3D scanning-based repair volume generation for damaged blades.

ICP-based algorithms iteratively minimize the combined squared distances between the measured data points and their closest points on the nominal model using a rigid body transformation comprising a translation and a rotation of measured data points. When it comes to scan-to-CAD registration of damaged blades, the geometric nonconformity between two datasets in the damaged regions (mainly material-missing regions) causes averaging-out errors on ICP-based rigid registration results [28, 29]. Recently, Ghorbani and Khameneifar [28, 120] developed a fine-tuned registration methodology to iteratively eliminate the unreliable scanned data points of the damaged regions from the rigid scan-to-CAD registration process using a group-to-group evaluation of

Euclidean distance and curvature of the local neighborhood of each measured data point and its nearest point on the CAD model resulting in more accurate scan-to-CAD rigid registration of damaged blades. In the present work, the scanned point cloud data has been registered to the nominal CAD model using the rigid scan-to-CAD registration method proposed by the authors in [28]. Thus, both scan data of the damaged blade and CAD model lie in the design coordinate system (DCS) after the scan-to-CAD rigid registration.

This paper aims to develop a novel methodology to construct a damage-free digital twin by accurately matching the CAD model with the scan data in the undamaged regions through incremental deformation of the CAD model towards the measured data. A stiffness term is applied in the objective function of the CAD-to-scan non-rigid registration algorithm to regularize the deformations of the CAD model to avoid shrinkage and expansion of the surface by preserving the local rigidity as much as possible. The main features of the proposed method for constructing the damage-free digital twin are outlined as follows:

- *Damaged regions' data points elimination*: a region growing segmentation method is employed to detect and remove the data points of material-missing areas of scanned point cloud data. We combine the Euclidean distance and normal vector angular difference to evaluate the geometric error between each measured data point and its nearest point on the CAD model and eliminate the measured data points with large geometric error under the proposed region growing segmentation framework. Since the scan data and the CAD model are aligned using the scan-to-CAD rigid registration in the previous step, the data points of the damaged regions can be accurately detected and eliminated using this segmentation approach before performing non-rigid registration.

- *CAD-to-scan non-rigid registration*: the aim of non-rigid registration is to project the deformations of the damaged blade surface onto the CAD model and get a damage-free digital twin of the defective blade. An accurate correspondence search method is developed to avoid the influence of unreliable corresponding pairs belonging to repair volume's geometry on non-rigid registration results. Instead of the closest point-to-point correspondence search, a point-to-surface correspondence search procedure is employed to reduce the influence of measurement noise and avoid shrinkage and expansion of data points set by finding the corresponding point of each CAD point on the quadric surface fitted to the local neighborhood of its nearest measured data point. The influence of unreliable correspondences in material-missing regions of the CAD model is eliminated through weighting of corresponding pairs and testing their reliability using medial axes mesh surface constraint. The non-rigid registration algorithm computes a transformation matrix for each CAD data point to match them with the measured data while preserving the local rigidity as much as possible.

5.3 Related Works

Traditionally, once the rigid scan-to-CAD registration is accomplished, a Boolean difference is performed between the scan data of the damaged blade and its nominal model to obtain the repair volume for additive restoration [12, 16, 29]. The original (nominal) CAD model [11, 12, 51, 74] or unused blade scanned data [13, 52] are used in the literature as nominal models for this Boolean operation. Zhang et al. [12] constructed the repair volume geometric model by a Boolean difference between the mesh model of the scanned damaged blade and the B-rep model of the original CAD model. Zheng et al. [11] generated the repair volume of the damage region through a distance-based comparison between measured data points and the CAD model when the damaged blade was aligned with the CAD using a best-fitting method. Zhang et al. [74] employed a voxel model of the measured damaged blade and the CAD model to extract the repair volume based on the constructive solid geometry (CSG) method. Zhao et al. [121] presented a non-layer-based additive manufacturing process called CNC accumulation for repair applications. They developed an in situ laser scanning system integrated with the CNC accumulation process to capture the geometric shape of damaged parts for related data processing, repair volume generation, and multi-axis tool path planning. They performed a Boolean difference between scanned surface mesh and CAD model to obtain the repair volume in triangulated mesh form for tool path planning. Liu et al. [51] proposed a shape-adaption algorithm to compare the polygonal cross-sections of the damaged blade with those of the nominal model to detect the defective segments, and then accordingly trim the nominal CAD model to construct the repair volume. Zhang et al. applied single-dexel modeling [13, 75] and tri-dexel modeling [52] for damage detection and repair volume construction by comparing the intersection of casting rays with the scan data of the damaged blade and a similar unused blade. As mentioned earlier, due to extreme working conditions, the geometric shape of aero-engine blades deviates from the original geometry, and therefore the nominal CAD model or unused blade's scanned point cloud are no longer appropriate for comparison with the damaged blade and generation of the geometric model of the repair volume.

To address the mentioned challenge of the CAD-based repair volume construction process, some researchers employed sectional profile information of damaged blades to take the deformations of undamaged regions into account when extracting the repair volume for damaged regions of the defective blade. Praniewicz et al. [14] proposed an adaptive repair strategy in which the airfoil profiles of the CAD model are aligned and deformed to best-match the measured sectional data in undamaged regions, and then the CAD profile geometry within the damaged region is manipulated via interpolation of the previous transformations to alter the final profile of the nominal model. To transform the deformations of the damaged blade onto the CAD model, the mean line of each CAD profile is manipulated to match the corresponding mean line of the measured profile. Wu et al. [76] analyzed the deformation mechanisms (i.e., bending and torsional deformations) of aero-engine blades under the aerodynamic loads to establish the relationship between the blade height and the cross-section curves deformation and utilized this relationship to transform the CAD model sections in order to obtain the airfoil profiles of the repair area. They used the spline interpolation method to provide a transition between undamaged and repaired regions of the welded blade. Yan et al. [15] combined the rigid registration with an offset factor in the normal direction of each point to iteratively align the cross-section curves of the CAD model and measured data in undamaged regions and deform the CAD cross-section via offsetting the data points. Then, the material-missing portions of the damaged blade are reconstructed through interpolating or extrapolating the airfoil profiles. The proposed methods in [14, 15, 76] have utilized several discrete 2D cross-section curves to capture the deformations of the blade surface. Using the cross-sectional data cannot provide complete information about the underlying geometry of the damaged blade and the reliability of the reconstructed surface in the damage region directly depends on the accuracy of constructed 2D cross-section airfoil profile. In addition, interpolation or extrapolation of cross-section curves for damage region reconstruction is a challenging and error-prone process that may not provide a smooth transition between repaired and unrepaired regions mainly for blade tip damages where there is no reliable 2D cross-section for surface reconstruction.

To construct the geometric representation of the repair volume, some researchers have tried to utilize the RE-based methodologies to create the blade surface in damaged regions using the point cloud data captured from the defective blade surface [16, 29]. In the RE-based approaches, the repair surface geometry in defective regions is obtained by sweeping the airfoil profiles generated in undamaged regions and extrapolating over the defective areas. Li et al. [29], Wilson et al. [16], and Piya et al. [78] extracted the repair volume through a Boolean difference between the RE-based constructed surface of the damaged region and the mesh surface of the scanned damaged blade. Gao et al. [77] and Yilmaz et al. [17] applied the RE-based methodology to generate a defect-free model of the damaged blade and compared it with the scanned welded blade to capture the geometry of excessive material and generate machining toolpaths. Due to employing only a limited number of airfoil profiles in undamaged regions to generate a defect-free model of the defective blade, Boolean operation between RE-based constructed surface and the defective blade cannot yield an accurate representation of repair volume geometry on the damaged region. In addition, since only the airfoil profiles in top and bottom sides of damaged regions (not the data points in the vicinity of the damage zone) are employed for surface reconstruction, the constructed repair volume geometry cannot provide a smooth geometric transition at the interface of the repair patch and the undamaged surface of the blade.

In a related work, Su et al. [122] proposed a method to construct the deformed blade model of scanned deposited blade to capture the geometry of the excess materials on repaired regions and restore the airfoil blade through machining process. They segmented the 3D scanned blade data points and nominal CAD model into four patches and proposed a non-rigid registration method to obtain the deformation rule between scanned point cloud data and nominal model in suction side and pressure side while maintaining local rigidity. Then, a reverse mapping is utilized to best match the vertices of the suction side and pressure side of the nominal model to those of the scan data. The deformed blade model is constructed by stitching the rest of the nominal model (i.e., leading edge, trailing edge, and the region belonging to the repair volume geometry) to the matched suction side and pressure side of the nominal model. They employed the point-to-point correspondence search for non-rigid registration which can be affected by measurement noise. In addition, the proposed method in [122] is not applicable for repair volume construction of tip damages containing leading and trailing edges of the damaged blade.

5.4 Proposed Methodology

The proposed algorithms for the elimination of data points of damaged regions and CAD-to-scan non-rigid registration are explained in detail in Section 5.4.2 and 5.4.3, respectively, but before that, we briefly explain the data borrowed from the previous steps of point cloud processing in Section 5.4.1.

5.4.1 Preliminaries

The main inputs to the algorithm are the scanned point cloud $P = \{p_1, p_2, p_3, \dots, p_n\}$ and CAD model data points $Q = \{q_1, q_2, q_3, \dots, q_m\}$ which both are in design coordinate system DCS after rigid scan-to-CAD registration. CAD model dataset is obtained by uniform sampling of the nominal CAD model (i.e., the NURBS surface) with the average point spacing of the sampled CAD model point cloud data equal to that of the measurement point cloud data. The scanned point cloud P is supposed to be cleaned point cloud data obtained by performing preprocessing for outlier removal and denoising at the leading edge and trailing edge. We borrow some information about the local underlying geometry of datasets P and Q through the local neighboring points of each data point. The Territory Claiming (TC) algorithm [93] is applied to establish the local neighborhood (*NB*) of each data point. TC algorithm yields a directionally-balanced local neighborhood around the query point [93, 94]. The normal vector sets of scanned point cloud $\mathbb{N}_P = \{\vec{n}_{p_1}, \vec{n}_{p_2}, \vec{n}_{p_3}, \dots, \vec{n}_{p_n}\}$ and CAD model $\mathbb{N}_Q = \{\vec{n}_{q_1}, \vec{n}_{q_2}, \vec{n}_{q_3}, \dots, \vec{n}_{q_m}\}$, also, are applied for geometric error calculation between two datasets in Section 5.4.2. The normal vector at each data point is computed through local quadric surface fitting to its neighboring points. The closest point on the fitted quadric surface to the point p_i is calculated, and then the normal vector is computed for the surface at that point and assigned back to the point p_i. This information will be used for the elimination of data points of damaged regions in Section 5.4.2 and the point-to-surface correspondence search in Section 5.4.3.1.

5.4.2 Elimination of data points of damaged regions

Since the proposed CAD-to-scan non-rigid registration algorithm deforms the CAD points set to match with their corresponding points on the measured point cloud, the presence of the data points of damaged regions in the non-rigid registration process results in wrongful corresponding pairs and deviation of the generated damage-free digital twin from the true geometric shape of the blade. To avoid the influence of the data points of damaged regions on the results, the scanned point cloud is segmented to identify the data points of defective regions (i.e., material-missing regions) and eliminate them from the CAD-to-scan non-rigid registration process. We employ a region growing segmentation method to divide the measured data into defective and non-defective regions using distance and normal vector comparison between each measured data point and its nearest point on the CAD model. After a scan-to-CAD rigid registration, both datasets are in DCS and the Euclidean distance of the measured data points from the CAD model in damaged regions is larger than the undamaged regions. Due to significant distortion of the damaged blade surface in the vicinity of the defective regions, employing a pure distance-based segmentation approach is not accurate enough to remove the data points of damaged regions, especially for the points close to the damage boundary. The normal vector direction of the measured data points is different from the CAD data points in the vicinity of the damage boundary. Therefore, in addition to distance, we also compare the normal direction of each measured data point p_i with those of its nearest point on the CAD model q_i to detect data points of damaged regions. Generally, in the damaged regions, the angular difference between the normal vector of the fitted local quadric surface at p_i , $\vec{n}_{p_i}$, and the normal vector of the fitted local quadric surface at q_i , $\vec{n}_{q_i}$, is larger than that of the points of undamaged areas. We combine the Euclidean distance $D_e(p_i, q_i)$ and normal vector angular difference $\theta_e(p_i, q_i)$ to evaluate the geometric error between points p_i and q_i. The geometric error is defined as the summation of normalized Euclidean distance $ND_e(p_i, q_i)$ and normalized angular difference between normal vectors $N\theta_e(p_i, q_i)$ at p_i and q_i as follows:

$$G_e(p_i, q_i) = ND_e(p_i, q_i) + N\theta_e(p_i, q_i) \tag{5.1}$$

$$\theta_e(p_i, q_i) = \mathrm{acos}\left(\frac{\vec{n}_{p_i} . \vec{n}_{q_i}}{\left|\vec{n}_{p_i}\right| . \left|\vec{n}_{q_i}\right|}\right) \tag{5.2}$$

The min-max normalization method is used to scale θ_e and D_e into the interval [0, 1] and make them unitless [123].

Figure 5.2 shows the flowchart of the region growing segmentation algorithm. The algorithm starts with a seed point representing the damaged region and grows the set of data points until it covers the entire damaged area. The algorithm first sorts the measured data points P in descending order ($\mathbb{Z}$) of the geometric error G_e and the measured point $\mathbb{Z}(1)$ with the largest G_e value and its neighboring points are added to the set $\{S\}$. In each iteration, the algorithm picks the data point p_i with largest G_e value from $\{S\}$ and compares the $G_e(p_i, q_i)$ value with the threshold value (*thr*). If $G_e(p_i, q_i) > thr$, the point p_i is added to the current damage region $\{R_d\}$ and its neighboring points $NB(p_i)$ are added to the set $\{S\}$. The value of threshold *thr* is selected by trial and error approach in which the region growing segmentation method has been performed on several test cases containing different sizes, geometries, and locations of material-missing damages to provide a reliable threshold value using which all damaged regions' data points are detected and stored in the set $\{R_d\}$. Figure 5.3(a) shows the geometric error G_e colormap of the point cloud of a simulated damaged blade with respect to its CAD model. Figure 5.3(b) plots the G_e values of the seed points versus the data point index in the tip damage zone using region growing algorithm. The tip damage zone is highlighted with a dashed-border rectangle in Figure 5.3(a). It is seen in Figure 5.3(b) that when the seed points grow to the undamaged region, the geometric error between the measured point and its closest point on CAD is reduced almost converging toward a fixed value. The region growing algorithm is terminated when the geometric error is smaller than a specified threshold value. Figure 5.3(c) depicts the data points of the damaged region obtained through the proposed region growing approach in the material-missing area highlighted with a dashed-border rectangle in Figure 5.3(a). All data points of the damaged regions of the defective blade are detected using the proposed region growing segmentation method and collected in dataset $\{R\}$.

By removing the data points of the damaged regions in $\{R\}$ from the scan data, we have a filtered point cloud of the defective blade in the design coordinate system (DCS) which includes only the undamaged regions' data points. The filtered scanned point cloud hereinafter called scanned point cloud data (or scan data), is used as a reference to deform the CAD model and construct the damage-free digital twin of the defective blade.

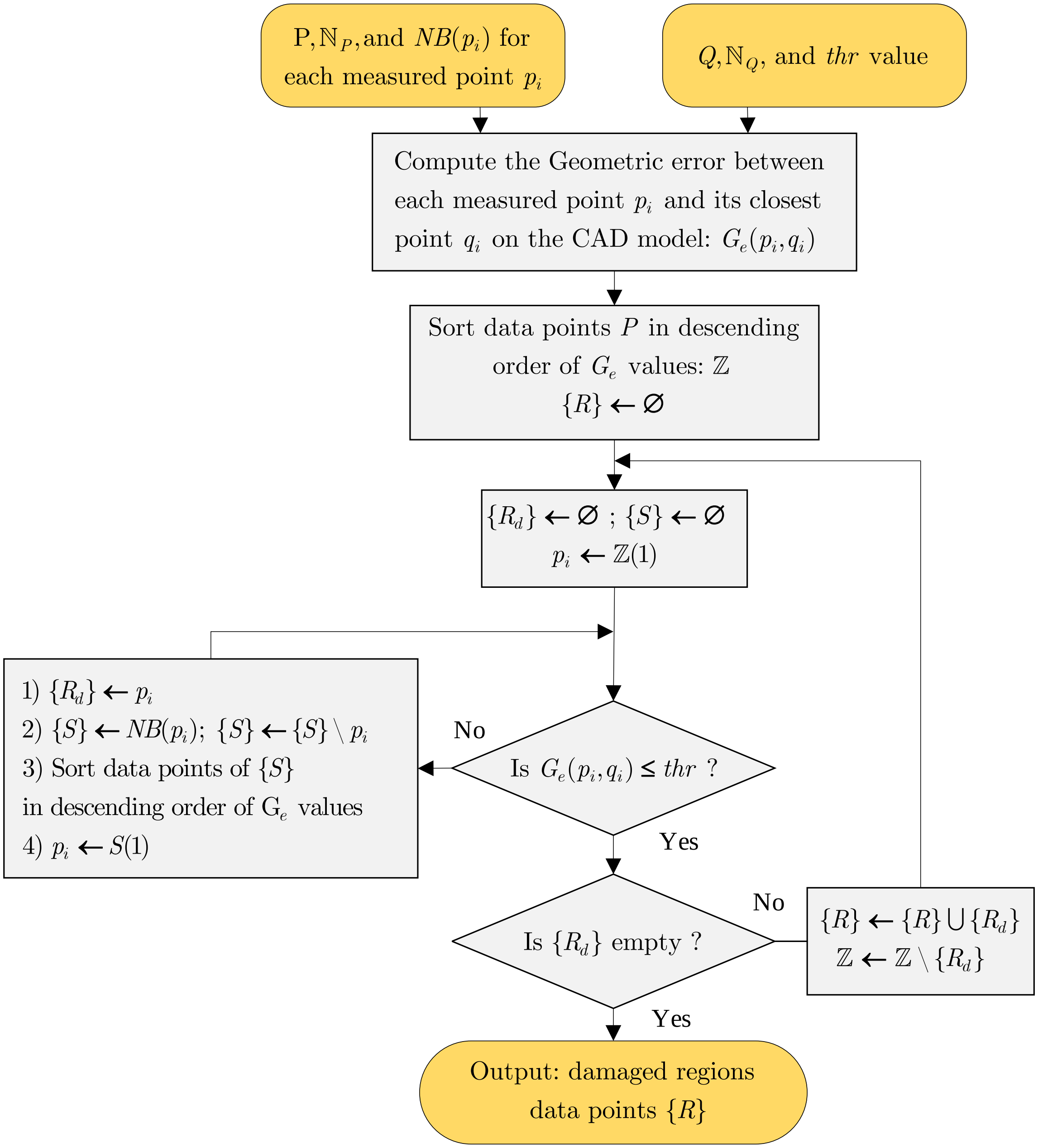

Figure 5.2 Flowchart of the region growing segmentation algorithm for detecting the data points of the damaged regions.

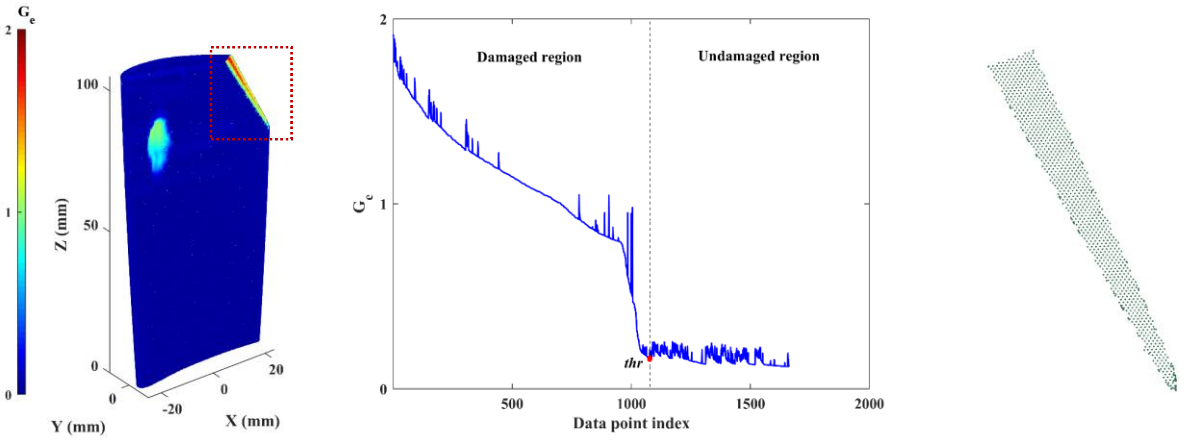

(a) (b) (c)

Figure 5.3(a) Geometric error (G_e) colormap of the point cloud of a simulated damaged blade with respect to its nominal CAD model, (b) G_e values of the seed points versus the data point index when expanding the damaged region depicted with dashed-border rectangle through region growing algorithm, and (c) the damaged region detected and removed from the point cloud data.

5.4.3 CAD-to-SCAN non-rigid matching

To construct a damage-free digital twin of the defective blade and obtain repair volume, a CAD-to-scan non-rigid registration methodology is proposed to specify the relationship between nominal model and scanned point cloud in undamaged regions where, due to harsh operation environment, the geometric shape of the aero-engine blade is different from the CAD model. The main idea behind the non-rigid registration is to find a transformation matrix for each corresponding pair in order to best match the CAD model to the scanned point cloud data while preserving the local rigidity. Figure 5.4 shows an intermediate step of the non-rigid registration in which the CAD data points move towards their corresponding points on the scanned point cloud using a locally affine transformation T_i. The algorithm mainly consists of two steps: correspondence search and transformation matrix computation for each CAD data point.

5.4.3.1 Correspondence search

The accuracy of the non-rigid registration highly depends on the reliability of corresponding pairs. Although the data points of damaged regions are removed from the measurement data before non-rigid registration, the correspondence search may face the following challenges:

- Since the measured point cloud of the damaged blade is noisy and often contaminated by outliers at high-curvature features (i.e., leading edge and trailing edge), the point-to-point correspondence search is often not able to provide a reliable correspondence for accurate projection of the nominal model towards the true underlying geometry of the measurement data. Due to employing the closest point-to-point correspondence search, shrinkage and expansion of the nominal model may occur when matching the nominal model onto the scanned point cloud [122]. Figure 5.4 shows the correspondences of CAD points obtained by the closest point search on the scan data. It is seen that due to using the closest point correspondence search approach, the CAD data points q_4 and q_5 have the same closest corresponding point p_6 on the scanned point cloud. As, later on, the transformation matrix deforms the CAD data points towards their corresponding points, using the closest point-to-point correspondence search, it may move more than one source point (CAD points) towards a scanned data point, leading to the shrinkage and expansion of the source dataset.
- For the CAD data points belonging to the repair volume geometry, there is no reliable corresponding point on the scanned point cloud data. As can be seen in Figure 5.4, the CAD data points q_6, q_7 and q_8 belong to repair volume patch for which there is no reliable correspondence on scanned point cloud; and consequently, the measured data points of the border of the damaged region are wrongfully selected as corresponding points (i.e., data points p_7 and p_8). Also, depending on the location, size, and geometry of damaged regions on the

blade surface, the closest corresponding points of the CAD data points of repair volume patch may be incorrectly picked from the other side of the blade surface. Figure 5.5 presents the closest correspondences of the CAD points belonging to the repair volume patch on the pressure side of the blade. This figure illustrates the problem on a 2D profile for the sake of better visualization. As we can see in Figure 5.5, for the CAD points on the pressure side of the blade, the closest correspondences are introduced on the suction side of the scanned blade surface. Employing the incorrect correspondences for CAD data points belonging to repair volume geometry results in the collapse of these points onto wrong measured data points and an inaccurate damage-free digital twin construction.

To address the errors resulting from the closest point-to-point correspondence search and eliminate the influences of corresponding pairs belonging to repair volume geometry on CAD-to-scan non-rigid registration we propose the following point-to-surface weighted correspondence search approach with medial axis constraint.

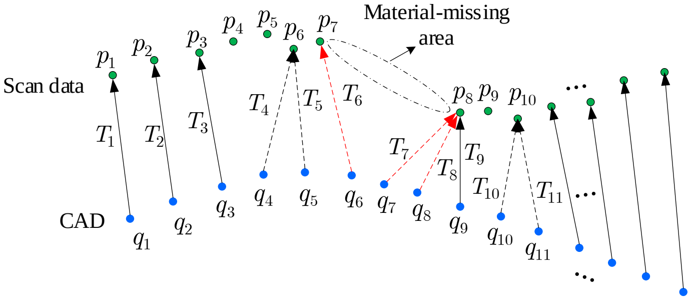

Figure 5.4 Closest point-to-point correspondence search procedure. Each CAD data point is then moved towards a corresponding measurement data point using a locally affine transformation matrix T_i.

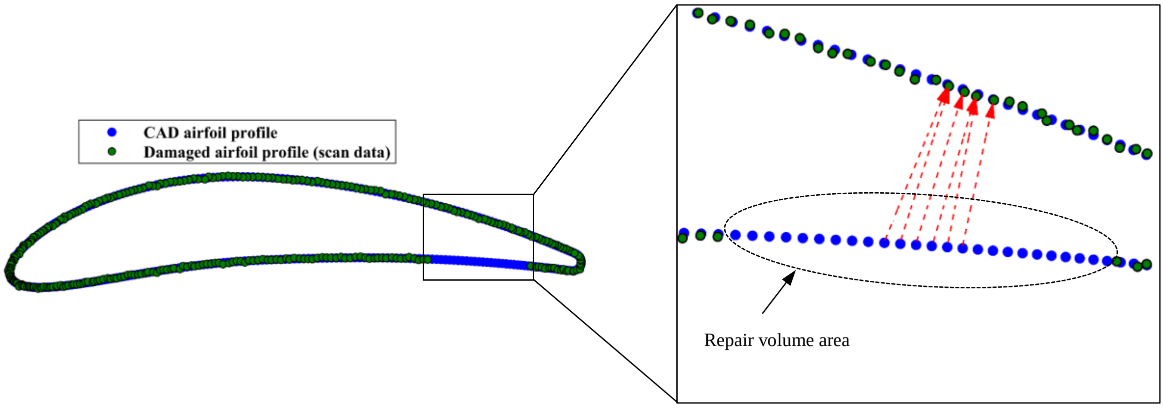

Figure 5.5 Incorrect correspondences between CAD data points (blue) belonging to repair volume region and scan data (green).

1- *Point-to-surface correspondence search*: to avoid shrinking and expanding the set of data points and eliminate the effects of measurement noise and outliers on the results of the CAD-to-scan non-rigid registration, we provide a unique correspondence for each CAD data point on the local underlying geometry of its closest point on the measurement dataset. As can be seen in Figure 5.6, for each CAD data point q_i, a quadric surface is fitted to the local neighborhood of its closest measured data point p_i and the nearest point p_i^* on the local surface to the point q_i is selected as the corresponding point. The proposed non-rigid registration method benefits from the point-to-surface correspondence search method to reduce the influence of measurement noise on damage-free digital twin construction and deform CAD points uniformly towards the underlying geometry of measured points which avoids shrinkage and expansion of CAD data points.

2- *Weighting of corresponding pairs*: a weight function is defined to measure the reliability of each corresponding pair. For each CAD data point q_i and its nearest measured data point p_i on the scanned point cloud, the weight value w_i is defined as:

$$w_i = 1 - e^{-(\frac{1}{D_i})^2} \tag{5.3}$$

where D_i is the number of CAD data points whose closest point on the scan data is p_i. For example, in Figure 5.4, the value of D_i for weight computation of CAD points q_7, q_8 and q_9 is equal to 3, because these points share the measured point p_8 as the nearest point on the scan data. Due to the fact that the calculated corresponding points for the CAD data points in the repair volume area are a few measured points lying on the border of damaged areas, D_i value for the CAD data points in the repair volume area is large, therefore the weight value w_i of the corresponding pairs in the repair volume areas of the CAD dataset is very small. Applying the weighting factor w_i significantly reduces the influence of unreliable corresponding pairs introduced in repair volume regions of the CAD model on non-rigid registration.

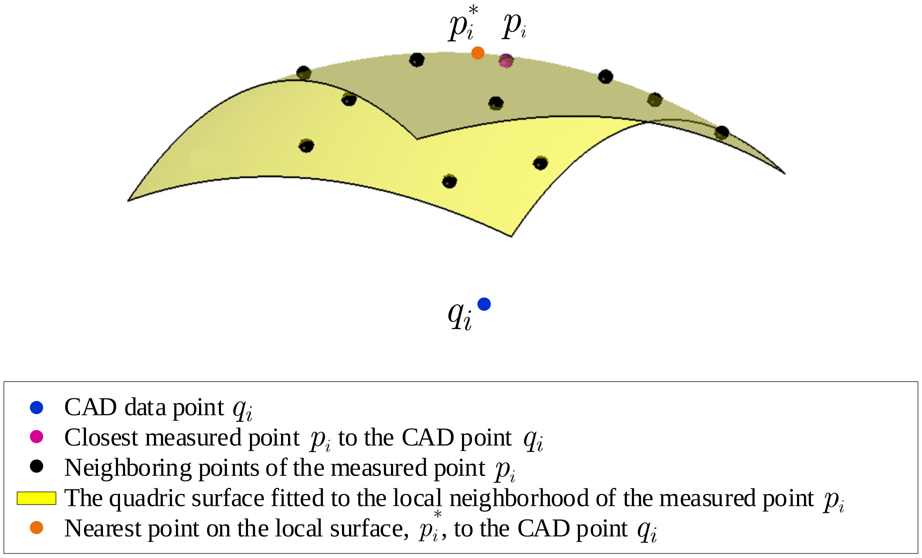

Figure 5.6 Finding the corresponding point of the CAD point q_i using the point-to-surface correspondence search: The closest measured data point (p_i) to the point q_i is found, and a quadric surface is fitted to the local neighboring points of p_i. Then, the nearest point on the local surface (p_i^*) to the point q_i is selected as the corresponding point of q_i.

3- *Medial axis constraint*: to avoid picking incorrect corresponding points for CAD points of repair volume geometry on the opposite side of the blade (see Figure 5.5), a mesh surface is generated using the sectional medial axes points to separate the suction side of the blade from its pressure side. Figure 5.7(a) shows the medial axis points of a 2D airfoil profile. We compute the medial axis points for several sectional airfoil profiles from the bottommost to the topmost section of the CAD model and create a mesh surface of the medial axes points as shown in Figure 5.7(b). Using the medial axis constraint, the point p_i^* (nearest point on the local surface fitted to neighboring points of p_i) is assigned as the corresponding point of CAD point q_i if the line segment p_i to q_i does not intersect the medial axes mesh surface.

The proposed correspondence search approach improves the accuracy of the subsequent non-rigid registration by removing the influence of incorrect corresponding pairs on transformation matrices computation.

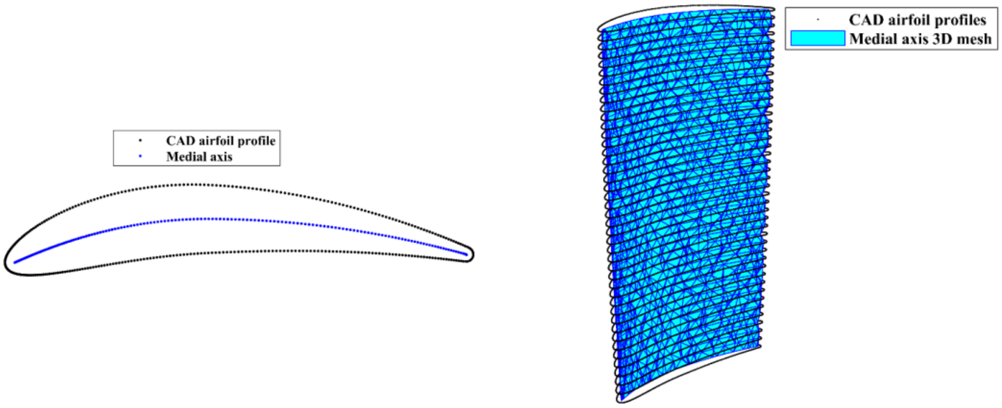

(a) (b)

Figure 5.7(a) Airfoil profile of a blade and its medial axis, and (b) the 3D mesh surface generated from the sectional medial axes points of CAD model.

5.4.3.2 Transformation calculation

If the CAD data points are given in homogenous coordinates q_i = [x,y,z,1]^T, an affine 3×4 transformation matrix T_i is defined for each CAD point q_i to project it onto its corresponding point p_i^*. As mentioned earlier, point p_i^* is the nearest point on the local surface fitted to the neighboring points $NB(p_i)$ where p_i is the closest measured data point to the CAD point q_i. The objective function ($E_d(T)$) for minimizing the distance between CAD model Q and dataset P^* is defined as follows [124]:

$$E_d(T) = \sum_{q_i \in Q} w_i \mathrm{dist}^2(p_i^*, T_i q_i)$$

$$T = [T_1, T_2, T_3, \ldots, T_m]^T \tag{5.4}$$

The reliability of the correspondences is weighted by w_i. To regularize the local deformation of the CAD points and provide a smooth projection, a stiffness term $E_s(T)$ is added to the cost function [124]:

$$E_s(T) = \sum_{q_i \in Q} \sum_{q_{i'} \in NB(q_i)} \left\| T_i - T_{i'} \right\|_F^2 \tag{5.5}$$

This term regularizes the deformation of CAD point q_i by penalizing the difference of the transformations of its neighboring points $NB(q_i)$ under the Frobenius norm $\|.\|_F$ which is computed as the square root of the sum of the squares of the elements of matrix $[T_i - T_{i'}]$. Utilizing the uniformly-sampled dataset of CAD model and adding the stiffness term to the objective function are both crucial to a reliable deformation of the CAD data points with a high degree of accuracy and local rigidity towards the underlying geometry of their corresponding points on the scanned point cloud data.

The full distance minimization objective function $E(T)$ is a weighted sum of $E_d(T)$ and $E_s(T)$ [124]:

$$E(T) = E_d(T) + \alpha E_s(T) \tag{5.6}$$

The parameter α, called the stiffness weight, influences the flexibility of the CAD model to accurately deform to match CAD data points to the scanned point cloud data. Since the cost function $E(T)$ is a quadratic function, we can convert it into linear equations and directly solve the problem by setting the derivative of the cost function to 0. The objective function $E(T)$ of Equation (5.6) is minimized under the non-rigid ICP framework [124].

Figure 5.8 shows the flowchart of the proposed non-rigid registration algorithm. The algorithm iteratively deforms the original (nominal) CAD model to match it to the scan data and get a damage-free digital twin of the defective blade. As mentioned earlier in Section 5.4.2., the scan data inputted to the non-rigid registration algorithm is a filtered scanned point cloud after removing all data points of damaged regions. This algorithm includes two main loops. The outer loop updates the stiffness weight value α in Equation (5.6) to deform the CAD model from global deformations toward more localized deformations. When the α value is high, the algorithm transforms the CAD model towards the scan data to recover the global deformations between two datasets, and then successively lower stiffness weights are used to recover more localized deformations on the surface. The inner loop of the algorithm iteratively computes the transformation of each CAD data point for a fixed stiffness value α_k to deform the CAD model gradually. In each iteration of the inner loop, the algorithm finds the nearest measured point p_i to each CAD point q_i to compute the weight value w_i, and then, fits a local quadric surface to neighboring points of the point p_i in order to get the corresponding point p_i^* of the CAD point q_i. The optimal transformations of CAD data points are determined for the corresponding pairs and fixed stiffness α_k through minimization of the objective function $E(T)$ of Equation (5.6). Due to stiffness term E_s defined in the objective function, the CAD data points are not projected directly towards their corresponding points but they may be projected parallel along the scan data to provide smooth local deformations. In each iteration, the algorithm reduces the distance between CAD data points and their corresponding points on measurement data [124].We compute the root mean square of weighted error of matching points (RMS_{we}) to measure the conformity between two datasets. Applying the RMS_{we} eliminates the influence of unreliable corresponding pairs (with small weight value) introduced in the repair volume zone of the CAD model on measuring the conformity between two datasets; and consequently, we can check the conformity between two datasets in the undamaged regions.

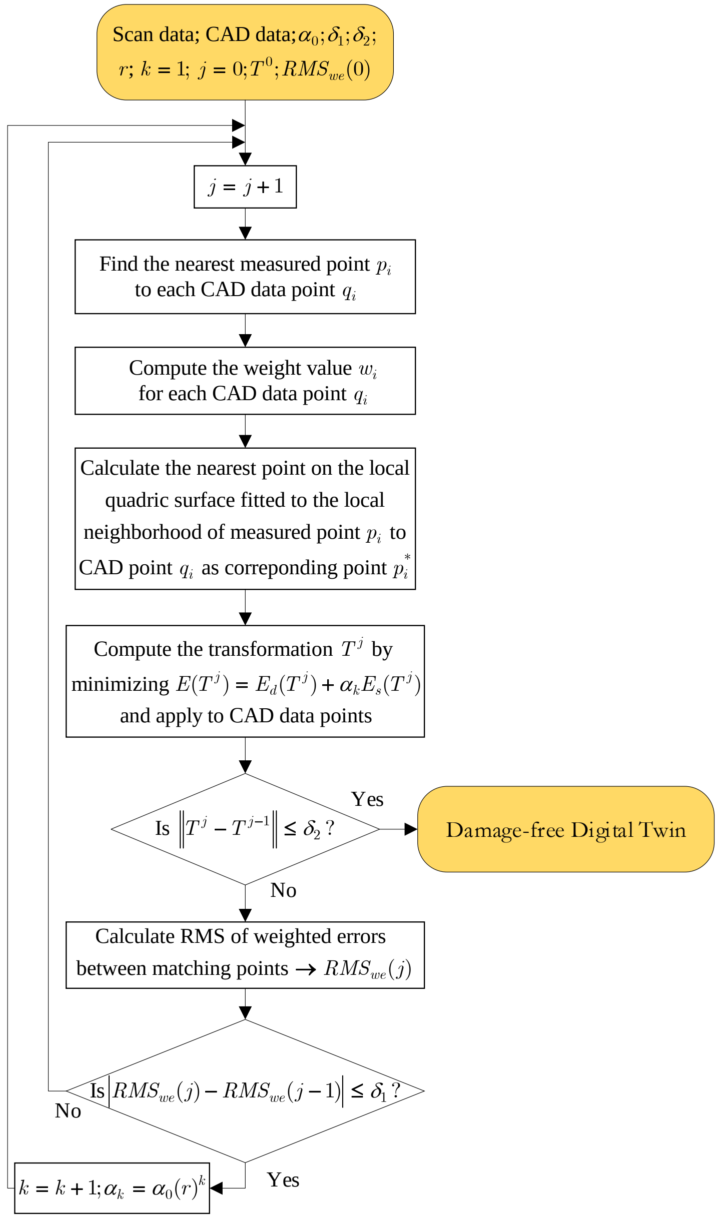

Figure 5.8 Flowchart of the proposed non-rigid registration method to construct the damage-free digital twin.

Figure 5.9(a) shows the RMS_{we} values in each iteration of the proposed CAD-to-scan non-rigid registration algorithm. The inner loop (with a fix α_k value) is repeated until the algorithm converges to a stable state where the change between RMS_{we} values of two successive iterations falls below a threshold δ_1. Then, the stiffness weight value α_k is lowered to continue the non-rigid registration process. For example, as can be seen in Figure 5.9(a), when the algorithm meets the threshold δ_1 for stiffness weight value α_0, the outer loop lowers the weight value to α_1 and repeats the search for optimal transformation matrices through minimization of the objective function $E(T)$ of Equation (5.6) in the inner loop. In order to enhance the efficiency and accuracy of the non-rigid registration process, the algorithm starts with a large stiffness weight value α_0 and incrementally decreases its value using the following relationship:

$$\alpha_k = \alpha_0 . (r)^k \tag{5.7}$$

where α_k is the stiffness weight value of the kth iteration of the outer loop and r (with a value between 0 and 1) is the stiffness weight coefficient. This relation provides a gradual relaxation of the stiffness term of the objective function during non-rigid registration and avoids high computation time. In the initial iterations of the algorithm, the difference between successive stiffness weight values is large while in the last iterations where the stiffness weight values are low, the difference between successive weight values is small. For lower α_k values where the stiffness term of the objective function is more relaxed, the distance between the CAD model and measurement point cloud is very small; therefore, the values of transformation matrix T become smaller and the CAD model is deformed slightly. Figure 5.9(b) depicts the Euclidean norm of the difference between transformation matrices of two successive iterations ($\|T^j - T^{j-1}\|$) of the proposed non-rigid registration algorithm. It is seen that the difference between two successive transformation matrices is gradually reduced to reach a small value. In the present work, the non-rigid registration algorithm terminates when the norm of the difference between transformation matrices of two successive iterations is smaller than a threshold δ_2.

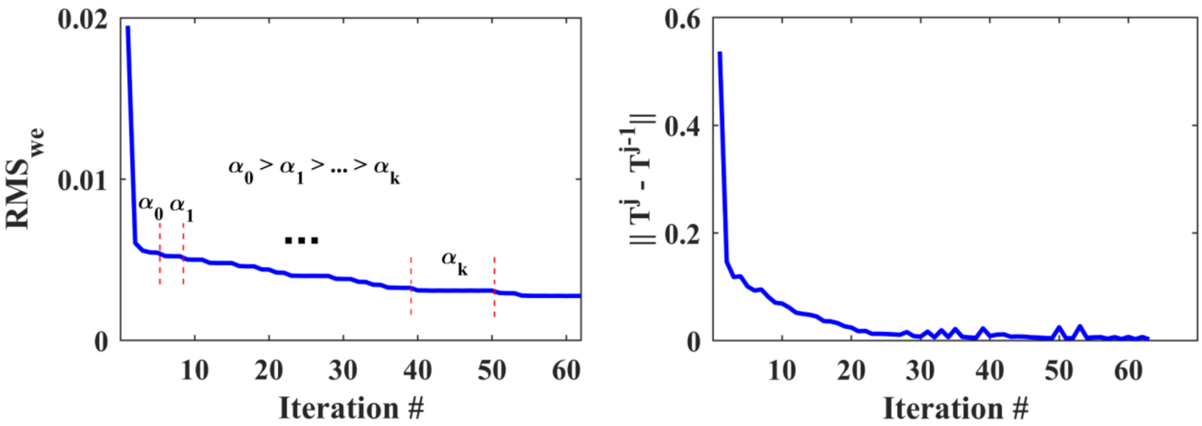

(a) (b)

Figure 5.9(a) Root mean squares of weighted error (RMS_{we}) of matching points in each iteration of the algorithm, and (b) norm of the difference between transformation matrices of two successive iterations.

5.4.3.3 Parameters

In the proposed non-rigid registration algorithm, there are a few parameters for which values must be specified: initial stiffness weight value α_0; stiffness weight coefficient r; inner loop threshold δ_1 and algorithm termination threshold δ_2. The stiffness weight values depend on the blade's geometry and the deformations on the undamaged regions of the defective blade, as well as the density of the point cloud data. Initial stiffness weight α_0 should be chosen such that at the beginning of the algorithm only the large deformations are covered. In this work, we start with a high α_0 to guarantee the accuracy of the results, although it may cause high computation time. The stiffness weight coefficient r applied in Equation (5.7) provides the required relaxation for the stiffness term of the objective function. r is a value between 0 and 1. If there is a high value of r, the algorithm may take more time to converge. The selection of inner loop threshold δ_1 and algorithm termination threshold δ_2 are related to geometric nonconformities between CAD and scanned point cloud in undamaged regions and the level of measurement noise. If there are big nonconformities and high measurement noise, the values of δ_1 and δ_2 should be larger. Based on a number of experiments, we apply the following settings in our implementation: $\alpha_0 \in [100 - 400]$; $r \in [0.75 - 0.95]$; $\delta_1 = [1 - 10] \times 10^{-6}$; $\delta_2 \in [1 - 5] \times 10^{-3}$.

5.5 Results and Discussions

Numerical and experimental case studies have been conducted to validate the proposed non-rigid registration method. For the numerical case studies, synthetic point cloud data are generated by sampling a simulated damaged blade for which the actual geometry of the simulated blade is known that can be used as the benchmark against which the CAD-to-scan non-rigid registration outcomes (i.e., damage-free digital twin) can be compared to assess the performance of the proposed algorithm. The blade CAD model was created with the overall dimensions of the blade roughly corresponding to a cuboid of 45 mm in length, 15 mm in width, and 105 mm in height. To follow a typical blade surface design, a twist of 25 degrees from the blade bottom to tip was introduced by incrementally twisting the airfoil sections from the bottommost to the topmost section. To simulate the deformed blade surface, certain form deviations were superimposed onto the nominal blade surface. First, a sinusoidal variation with the random amplitudes between 0 and 0.005 mm was superimposed onto the airfoil sections of the CAD model in the direction of the profile normal to emulate the combination of the typical manufacturing errors on the blade surface. Then, a sinusoidal variation with an amplitude between 0.04 and 0.08 mm was added to the pressure and suction sides of some airfoil sections of the blade to resemble a typical geometric deformation on a used blade during its operation. Next, geometric defects were added to the airfoil sections to simulate damages (material-missing regions) on the blade tip at the trailing edge as well as the pressure side of the blade surface. Using the NURBS surface interpolation of the airfoil sections, the simulated defective blade surface was created, which is then used as a reference. Figure 5.10

shows the nominal CAD model, as well as the simulated defective blade and simulated (actual) damage-free blade with their error colormaps with respect to the nominal CAD model. Since the maximum deformation of the actual damage-free blade (Figure 5.10(c)) with respect to the original CAD model is almost 0.1 mm, the error colormap range in Figure 5.10(b) is also capped at the same range (i.e., [0, 0.1] mm) for the sake of better visualization.

Then, the simulated damaged blade surface was randomly sampled to generate an ideal (noise-free) point cloud. In practice, the scanned point cloud data contains measurement noise. Therefore, the synthetic point clouds should also include the measurement noise for simulating the real scanned point cloud data. In order to generate noisy point clouds of the simulated blade, Gaussian deviates with 0.01 mm standard deviation (with the distribution’s mean at zero) were superimposed onto the ideal point cloud in random directions.

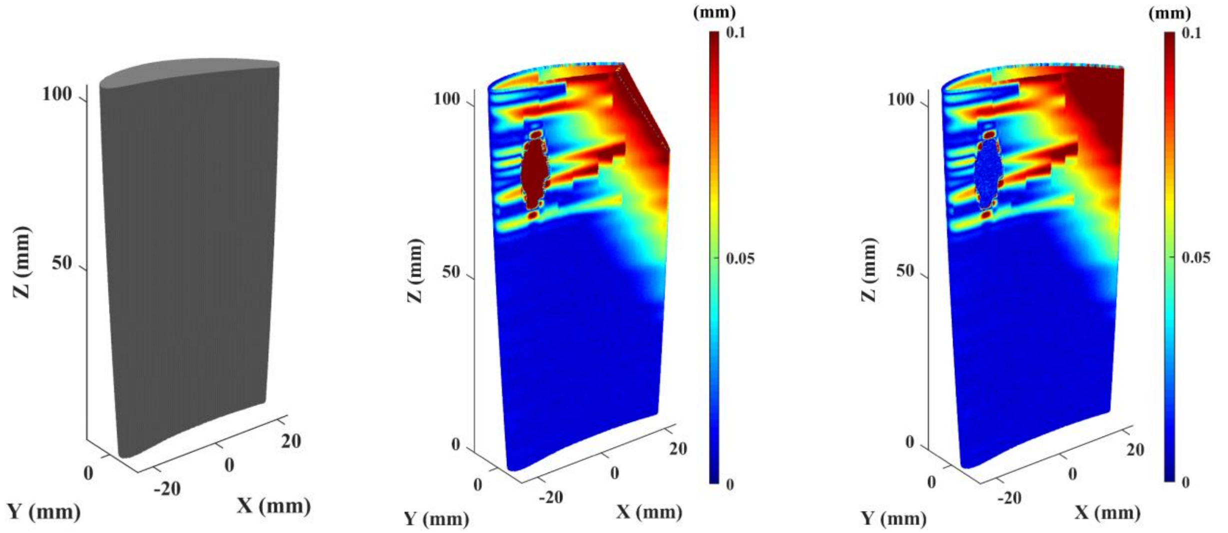

(a) (b) (c)

Figure 5.10(a) Nominal CAD model, (b) error colormap of the simulated point cloud (without noise) of the damaged blade, and (c) error colormap of point cloud of its actual damage-free blade.

5.5.1 Damage-free digital twin constructed based on the ideal point cloud (without noise) of simulated damaged blade

Figure 5.11(a) shows the error colormap (with respect to the original CAD model) of the constructed damage-free digital twin based on the ideal point cloud (without noise) of the simulated defective blade. Table 5.1 presents the deviation of the actual damage-free blade (Figure 5.10(c)) from the original CAD model (Figure 5.10(a)) and deformed CAD model (Figure 5.11(a)), i.e., constructed damage-free digital twin. As can be seen in Table 5.1, the average deviation of the actual damage-free blade from the CAD model and the generated damage-free digital twin model is 0.0223 mm and 0.0021 mm, respectively; that is, the proposed non-rigid registration method removes more than 90% of geometric nonconformities between the actual damage-free blade and original CAD model. Figure 5.11(b) shows the error colormap of damage-free digital twin obtained by non-rigid registration using closest point-to-point correspondence search instead of point-to-surface corresponding search. It is seen that the constructed damage-free digital twin by point-to-point correspondence search contains considerable shrinkage and expansion on the undamaged region's surface. To evaluate the performance of the proposed non-rigid registration method on the geometry of material-missing regions, the airfoil profiles of the generated damage-free digital twin models (in Figure 5.11(a) and (b)) are reconstructed for sectional data points of material-missing regions. In the present work, the adaptive curvilinear projection method presented in [9] was employed to get the sectional data points from 3D point cloud data, and then the airfoil profile reconstruction method of [125] was utilized to generate a smooth airfoil profile from 2D sectional data points. Figure 5.11(c) depicts the airfoil profiles reconstructed from sectional data points of the generated damage-free digital twin models, original CAD profile, actual damaged profile, and actual damage-free profile. The actual damaged profile and actual damage-free profile are reconstructed respectively from the sectional data points of the simulated damaged blade (Figure

5.10(b)) and simulated damage-free blade (Figure 5.10(c)). The airfoil profiles are reconstructed from sectional data points at Z = 90 mm belonging to a material missing region (tip damage) of the simulated damaged blade.

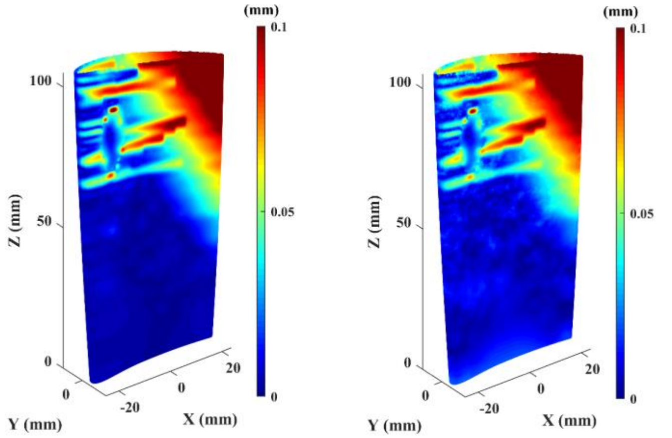

(a) (b)

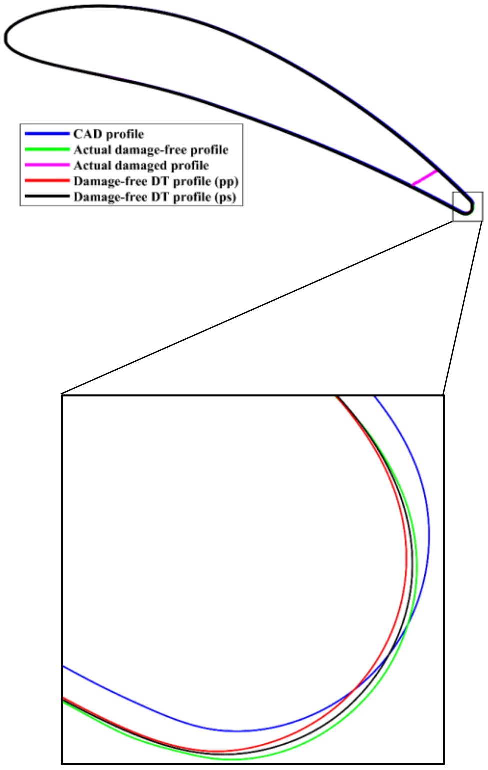

(c)

Figure 5.11(a) Error colormap (with respect to original CAD model) of the damage-free digital twin constructed based on the noiseless point cloud of the simulated defective blade, obtained by non-rigid registration process using (a) point-to-surface correspondence search (ps) and (b) closest point-to-point correspondence search (pp); (c) comparison between actual damage-free profile and airfoil profiles of damage-free digital twin (DT) models, CAD profile, and actual damaged profile at Z = 90 mm.

Table 5.1 Deviation of the actual damage-free blade (Figure 5.9(c)) from the original CAD model (Figure 5.9(a)) and from the constructed damage-free digital twin (Figure 5.10(a)).

	Deviation from CAD	Deviation from damage-free digital twin	Improvement (%)
Average error (mm)	0.0223	0.0021	90.93 %

Table 5.2 lists the deviation (root mean square error *RMSE*) of the original CAD profile and reconstructed profiles of the generated damage-free digital twin models from the actual damage-free profile at Z = 90 mm. As can be seen in Figure 5.11(c) and Table 5.2, there is a significant profile error (0.0618 mm) between CAD profile and actual damage-free profile which is resulted from the distortion of the simulated damaged blade. The profiles of the damage-free digital twin models have small RMS errors of 0.0067 mm (for closest point-to-point correspondence search) and 0.0041 mm (for point-to-surface correspondence search). The airfoil profile errors also demonstrate the superior performance of the point-to-surface correspondence search (ps) in non-rigid registration process over the closest point-to-point (pp) method, since the *RMSE* of the profile of the damage-free digital twin obtained by point-to-surface correspondence search from the actual profile is 0.0026 mm less than *RMSE* of the profile of the one obtained through point-to-point correspondence search. Figure 5.11(c) shows that there is a shrinkage in high-curvature features (i.e., trailing edge) of the damage-free digital twin obtained through closest point-to-point correspondence search (pp) which may lead to an inaccurate repair volume computation and unsmooth (jagged) transition between repaired and unrepaired regions. The CAD-to-scan non-rigid registration results demonstrated the effectiveness of the proposed method for accurate deformation of the CAD model to match it to the point cloud of the simulated damaged blade.

The computations required for the CAD-to-scan non-rigid registration were carried out in MATLAB R2018a on a PC with a 3.6 GHz Intel Core i7-7700 processor and 32 GB of RAM without parallel computing. The computation times for the construction of the damage-free digital twin models depicted in Figure 5.11(a) and (b) are listed in Table 5.3. The point clouds of Figure 5.11(a) and (b) contain 258,520 points. As can be seen in the table, the point-to-point correspondence search takes less time for damage-free digital twin construction than the point-to-surface correspondence search approach. Using the point-to-surface correspondence search, instead of finding the closest point on the scanned dataset as the corresponding point, the algorithm computes the nearest point to the CAD point on the local quadric surface fitted to the local neighboring points of the closest point on the scan data as the corresponding point. Therefore, the point-to-surface correspondence search is computationally more expensive than the point-to-point correspondence search. Also, computation time of the region growing segmentation approach for detection of the damaged regions' data points of the damaged blade in Figure 5.11(b) is 54 seconds.

Table 5.2 *RMSE* of the original CAD profile and the airfoil profiles of generated damage-free digital twin models from the actual damage-free profile at Z=90 mm.

	CAD profile	Damage-free digital twin profile (point-to-point correspondence search)	Damage-free digital twin profile (point-to-surface correspondence search)
RMSE (mm)	0.0618	0.0067	0.0041

Table 5.3 Computation time for the construction of the damage-free digital twin models shown in Figure 5.11(a) and (b) using the proposed CAD-to-scan non-rigid registration.

No. of iterations	Digital twin construction with point-to-point correspondence search (min)	Digital twin construction with point-to-surface correspondence search (min)
62	37.53	43.86

5.5.2 Damage-free digital twin constructed based on the noisy point cloud of simulated damaged blade

Here, we evaluate the performance of the proposed method in the presence of measurement noise. The synthetic noisy point cloud with 0.01 mm level of noise is inputted to the non-rigid registration algorithm. Figure 5.12(a) shows the error colormap of the damage-free digital twin of the noisy point cloud of the simulated defective blade with respect to the original CAD model after non-rigid registration by point-to-surface correspondence search. As can be seen in Table 5.4, the average deviation of the actual damage-free blade from generated damage-free digital twin is 0.008 mm, which means the proposed methodology has eliminated more than 64% of geometric nonconformities between the actual damage-free blade and original CAD model through non-rigid registration of CAD model to the noisy point cloud of the defective blade. Figure 5.12(b) depicts the error colormap of damage-free digital twin of the noisy point cloud of the simulated defective blade obtained by the closest point-to-point correspondence search. It is seen that the closest point-to-point correspondence search approach is more affected by noise in both damaged and undamaged regions than the point-to-surface correspondence search method. Because of unreliable correspondences created by the closest point-to-point search, there is a considerable shrinkage and expansion on the damage-free digital twin model of Figure 5.12(b). Figure 5.12(c) shows the airfoil profiles reconstructed from sectional data points of the generated damage-free digital twin of the noisy point cloud of the defective blade and compares them with the CAD profile, actual damaged profile, and actual damage-free profile at Z=90 mm. According to the results depicted in Table 5.5, the *RMSE* of the reconstructed profiles of the damage-free digital twin models obtained by closest point-to-point and point-to-surface correspondence search from the actual damage-free profile are respectively 0.009 mm and 0.006 mm which are significantly smaller than the CAD profile deviation (i.e., 0.0681 mm).

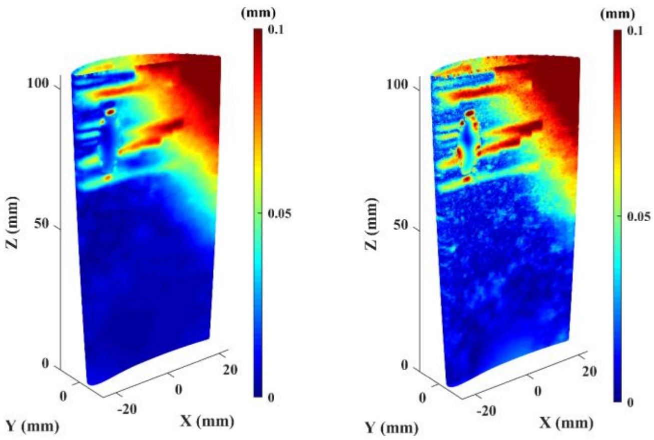

(a)

(b)

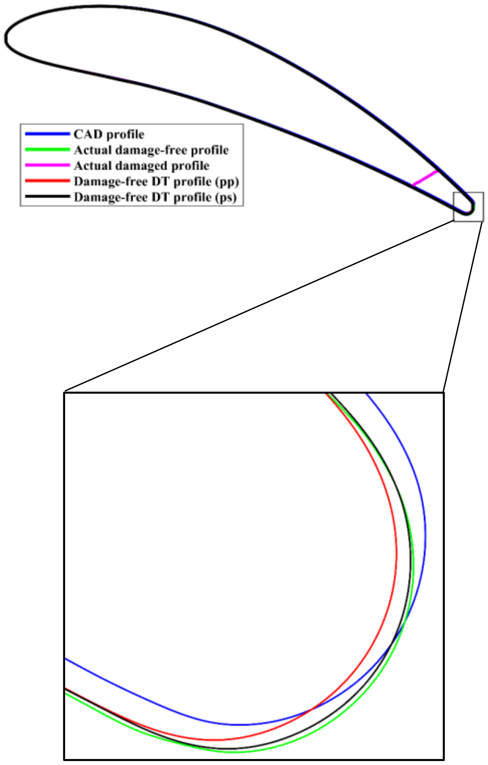

(c)

Figure 5.12(a) Error colormap (with respect to original CAD model) of the damage-free digital twin constructed based on the synthetic noisy point cloud of the simulated defective blade, obtained by non-rigid registration using (a) point-to-surface correspondence search (ps) and (b) closest point-to-point correspondence search (pp); (c) comparison between actual damage-free profile and airfoil profiles of damage-free digital twin (DT) models, CAD profile, and actual damaged profile at Z = 90 mm.

Table 5.4 Deviation of the actual damage-free blade (Figure 5.10(c)) from the original CAD model (Figure 5.10(a)) and from the constructed damage-free digital twin (Figure 5.12(a)).

	Deviation from CAD	Deviation from damage-free digital twin	Improvement (%)
Average error (mm)	0.0223	0.0080	64.29 %

Table 5.5 *RMSE* of the original CAD profile and the generated airfoil profiles of damage-free digital twin models based on the synthetic noisy point cloud from the actual damage-free profile at Z=90 mm.

	CAD profile	Damage-free digital twin profile (point-to-point correspondence search)	Damage-free digital twin profile (point-to-surface correspondence search)
RMSE (mm)	0.0618	0.0090	0.0060

These results also show that the non-rigid registration by point-to-surface correspondence search has a superior performance over the closest point-to-point correspondence search in the presence of noise. The *RMSE* of the profile of the damage-free digital twin obtained by point-to-surface (ps) correspondence search from the actual damage-free profile is 0.003 mm smaller than that of the damage-free digital twin generated through the closest point-to-point (pp) search. It is also visually seen in Figure 5.12(c) that the nonconformity between point-to-surface damage-free digital twin profile and actual damage-free profile in high-curvature feature of the blade is less than point-to-point damage-free digital twin profile. The results for the synthetic noisy point cloud data demonstrate that the proposed method is robust to noise and can accurately deform the CAD model to match it to the noisy point cloud and generate an accurate damage-free digital twin model while avoiding shrinkage and expansion of data points set.

5.5.3 Damage-free digital twin of a scanned damaged blade

Here, an experimental case study is presented in which we construct the damage-free digital twin of a damaged blade from the scanned point cloud data of it. The damaged blade was scanned using an ATOS Core 200 (GOM, Braunschweig, Germany) structured-light 3D scanner. Figure 5.13 shows the damaged blade being scanned, the scanned point cloud data, and the nominal CAD model of the blade. The scanned point cloud contains 950,202 points with an average point spacing of 0.08 mm. The damaged blade includes voids and tip damage (see Figure 5.13), which are common material-missing type damages on the surface of aero-engine blades. Since the scanned point cloud data has an arbitrary relative position and orientation with respect to the CAD model, as can be seen in Figure 5.13(b) and (c), the fine-tuned registration algorithm of [28] is applied to align the measurement data with the CAD model using a rigid body transformation. It should be noted that, in this work, we have employed the raw scanned point cloud data of the blade as input, which is contaminated by outliers at the high-curvature features.

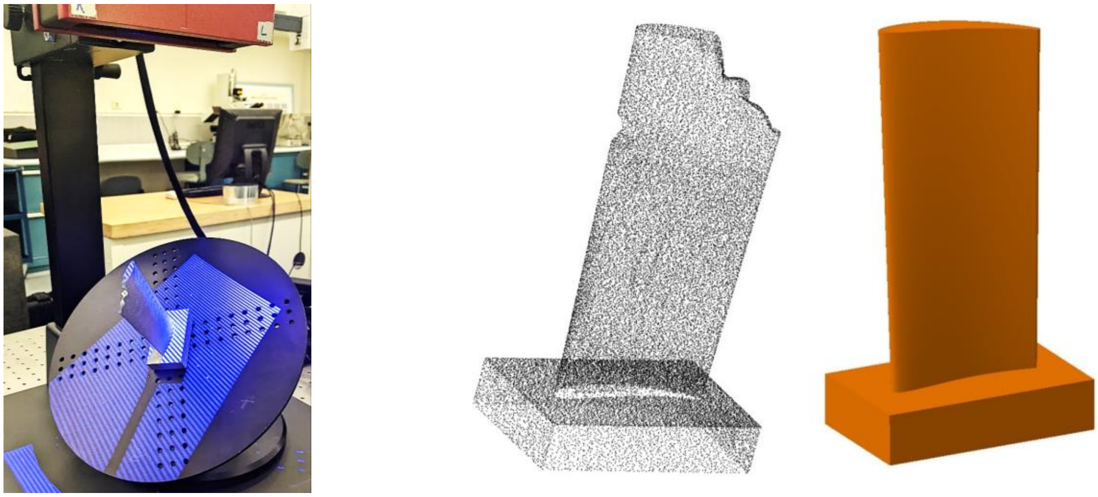

(a) (b) (c)

Figure 5.13(a) The damaged blade being scanned by the structured-light scanner, (b) the scanned point cloud of the damaged blade (the decimated point cloud data is shown for the sake of better visualization), and (c) the nominal CAD model of the blade.

Figure 5.14(a) shows the error colormap of scanned point cloud data with respect to the CAD model after being aligned using the fine-tuned scan-to-CAD rigid registration algorithm of [28]. The error range of the colormap is capped at 0.5 mm for the sake of better visualization. Figure 5.14(b) depicts the error colormap of the generated damage-free digital twin with respect to the nominal CAD model after point-to-surface non-rigid registration. It is seen by comparing the colormaps of Figure 5.14(a) and Figure 5.14(b) that the proposed algorithm correctly deforms the original CAD model in undamaged regions to match it to the scanned point cloud data. Due to the fact that there is no actual damage-free digital twin for which the actual deviations from the CAD are known, as a reference, the performance of the proposed CAD-to-scan non-rigid registration is evaluated through error evaluation between undamaged regions of the scanned damaged blade and constructed damage-free digital twin. Table 5.6 lists the deviation of the data points of undamaged regions of the scan data from the CAD model after rigid scan-to-CAD registration and from damage-free digital twin after the proposed non-rigid CAD-to-scan registration, respectively. It is seen that the average deviation between the scan data and the generated damage-free digital twin model is 0.067 mm smaller than the average deviation between the scan data and the original CAD model, which means a 32.5 % improvement in conformity of damage-free digital twin model to the scanned point cloud compared to the original CAD model.

A Boolean difference is performed between mesh models of the scan data and the damage-free digital twin in MeshLab software to get the geometric model of the repair volume (see Figure 5.14(c)). MeshLab carries out an exact Boolean difference between the two meshes using the code provided in the libigl library [126], which uses the method proposed in [127]. The acquired repair volumes can be used in subsequent steps of remanufacturing process planning including additive and subtractive repair toolpath generation.

Table 5.6 Deviation of the data points of undamaged regions of the scanned point cloud from the CAD model (after scan-to-CAD rigid registration) and from damage-free digital twin model (after proposed non-rigid registration).

	Deviation from CAD (after rigid registration)	Deviation from damage-free digital twin (after non-rigid registration)	Improvement (%)
Average error (mm)	0.2057	0.1388	32.5 %

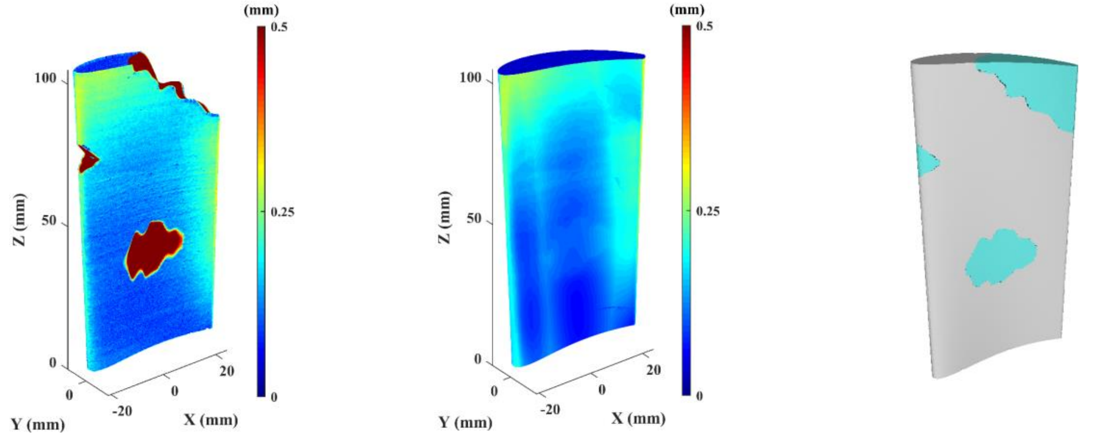

(a) (b) (c)

Figure 5.14(a) Deviation of the scan data from original CAD model after fine-tuned scan-to-CAD rigid fine-tuned registration of [28], (b) deviation of the damage-free digital twin from original CAD model after CAD-to-scan non-rigid registration, and (c) repair volumes representation in triangulated mesh form obtained by a Boolean difference between damage-free digital twin and scan data.

5.6 Conclusions

This paper presents a new methodology to accurately construct a damage-free digital twin of a damaged blade for generating the repair volume geometry for additive restoration of the damaged blade based on its scan data. A region growing segmentation approach is employed to eliminate the data points of damaged regions from the scanned point cloud of the damaged blade through geometric error evaluation between the scan data and the CAD model. The Euclidean distance and angular difference between normal vectors of each measured data point and its closest point on the CAD model are combined for geometric error computation. We propose a CAD-to-scan non-rigid registration algorithm to specify the relationship between the CAD model and the scanned point cloud of the damaged blade in order to deform the CAD model incrementally to match it to the defective blade in undamaged regions while preserving local rigidity of data points as much as possible. The proposed non-rigid registration benefits from a point-to-surface correspondence search method developed to reduce the influence of measurement noise on damage-free digital twin construction and avoid shrinkage and expansion of data points set in high curvature features (i.e., leading and trailing edges) by finding the corresponding point of each CAD point on the quadric surface fitted to the local neighborhood of its nearest measured data point. The proposed correspondence search method eliminates the influences of the unreliable corresponding pairs introduced in the repair volume region of the CAD model by weighting them and using the medial axes mesh surface constraint. The weighted stiffness term of the objective function of the non-rigid registration algorithm regularizes the deformation of CAD data points by penalizing the difference of the transformations of neighboring points to provide a smooth geometric transition at the interface of the constructed repair region and undamaged region.

Implementation results on numerical and experimental case studies have demonstrated the effectiveness of the proposed method in generating an accurate damage-free digital twin of the defective blade and avoiding the shrinkage and expansion of data points set in high curvature features of the blade. The Airfoil profile comparison in repair volume regions has substantiated superior performance of the proposed point-to-surface correspondence search over the traditional point-to-point correspondence search.

Although the proposed damage-free digital twin construction approach is accurate and effective, the non-rigid registration method is relatively computationally expensive. Thus, an avenue for future research is to focus on improving the efficiency of the proposed algorithm either through simplification of scan and CAD point clouds to reduce the computation time of non-rigid registration process or using voxel-based models instead of point-based models. In both cases, there would be a trade-off between preserving the fine details of data and computational efficiency depending on the resolution of the model. With low resolutions, useful data will be lost. Using high resolutions to preserve the fine details of data will increase the computation time. Due to the fact that the simplified datasets should preserve the details of the original models, it calls for further research on feature-preserved data simplification methods to enhance the efficiency of the proposed methodology while maintaining the accuracy at an acceptable level.

Chapter 6 GENERAL DISCUSSION

During the course of this research, we mainly focused on the development of a framework for automatic inspection and repair volume construction of damaged aero-engine blades using the 3D scanned point cloud data. The 3D scanned point cloud of the damaged blade and CAD model are given as input to the computational framework. This framework includes three main steps: a) scan-to-CAD rigid registration to bring the scanned point cloud data of the damaged blade and its CAD model into a common coordinate system, b) airfoil profile reconstruction from 2D sectional scattered data points for section-specific inspection of the damaged blade in undamaged regions, and c) damage-free digital twin construction of the defective blade for repair volume generation. The main contributions in each component of the proposed virtual framework are summarized as follows:

1- A novel scan-to-CAD rigid registration method has been developed for alignment of the scanned point cloud of the damaged blade with its CAD model to address the averaging-out errors resulted from original ICP-based registration algorithms. The proposed approach includes three main steps: rough registration, fine registration, and fine-tuned registration. In the correspondence search of fine-tuned alignment, the algorithm automatically assesses the geometric dissimilarity of each corresponding pair through group-to-group evaluation of Euclidean distance and curvature of the local neighborhood of each measured point and its nearest point on the CAD model and eliminates the unreliable pairs of damaged regions from the registration process. Numerical case studies have been conducted to validate the proposed alignment method. Comparison of the developed alignment method with the existing methods demonstrates the superiority of the proposed approach in aligning the point cloud of the damaged blade to the CAD model and its robustness to measurement noise. Moreover, the performance of the proposed method is examined in an experimental case study with a real scanned point cloud.

2- An airfoil profile reconstruction methodology has been developed to generate a smooth airfoil profile from unorganized and noisy sectional data points for section-specific geometric error evaluation of airfoil profiles in undamaged regions of the defective blades. The main contribution of the proposed method lies in automatically thinning the scattered sectional data points within the measurement uncertainty constraint of inspection data using a recursive weighted local least squares technique. A reliable profile polygon is generated from thinned data to order the dataset with no user interaction. After thinning and ordering the unorganized set of sectional data points, the smooth airfoil profile is generated by fitting a closed nonperiodic B-spline curve on the ordered data. Employing the proposed airfoil profile reconstruction, the centroid location and orientation angle of airfoil sections have been accurately estimated, which play a critical role in the precision inspection of aero-engine blades using non-contact 3D scanning techniques for MRO applications. The proposed method has been validated using synthetic inspection data points from the simulated in-service blade with known geometric deformations and manufacturing errors as reference. The performance of the airfoil profile reconstruction approach has also been evaluated for point clouds in presence of various measurement noise levels and various point cloud densities. In addition to blade inspection, the developed approach can equally benefit for automatic airfoil profile reconstruction in regenerate and adaptive machining of aero-engine blades.

3- A new methodology has been proposed to construct the repair volume by establishing a damage-free digital twin of the defective blade using a CAD-to-scan non-rigid registration approach. Utilizing a constrained point-to-surface correspondence search method, the algorithm avoids incorrect correspondences and eliminates the effects of measurement noise and outliers on the CAD-to-scan non-rigid registration. The damage-free digital twin has been constructed through incrementally deformation of CAD data points towards the measured data under the local rigidity constraint to avoid shrinking and expanding of data points and yield the repair volume with a smooth geometric continuity at the interface of the constructed repaired areas and unrepaired regions of the damaged blade. The developed repair volume construction method has been validated using numerical (i.e., the synthetic point cloud of the damaged blade) and experimental case studies. The Hybrid manufacturing applications can be equally benefited from the proposed method for toolpath generation in additive and subtractive processes.

The outcomes of each sub-objective of this thesis have been/will be published in peer-reviewed journals and conference paper listed as follows:

1. Sub-objective 1:
    - Ghorbani, H. and Khameneifar, F., 2021, “Accurate Registration of Point Clouds of Damaged Aeroengine Blades,” *Journal of Manufacturing Science and Engineering, Transactions of the ASME*, 143(3), pp. 031012-1--031012-10.
    - Ghorbani, H. and Khameneifar, F., 2022, “Scan-to-CAD Alignment of Damaged Airfoil Blade Point Clouds through Geometric Dissimilarity Assessment,” *Procedia CIRP*.
2. Sub-objective 2:
    - Ghorbani, H. and Khameneifar, F., 2021, “Airfoil Profile Reconstruction from Unorganized Noisy Point Cloud Data,” *Journal of Computational Design and Engineering*, 8(2), pp. 740--755.

3. Sub-objective 3:

   - Ghorbani, H. and Khameneifar, F., “Construction of Damage-free Digital Twin of Damaged Aero-engine Blades for Repair Volume Generation in Remanufacturing,” *Robotics and Computer-Integrated Manufacturing*, under review.

Chapter 7 CONCLUSIONS AND FUTURE RESEARCH DIRECTIONS

7.1 Conclusions

Due to operation in harsh environments, blades are susceptible to geometric deformations and material-missing damages on the surface. Blades must thus be inspected during their service life to check for their conformance to the design tolerances. Accurate inspection of in-service blades is crucial to make a reliable decision on acceptance, rejection, or repair of inspected blades. On the other hand, remanufacturing of damaged blades is of great interest for MRO applications to extend the service life of blades and reduce the costs associated with the replacement of new blades.

This thesis develops a framework for automatic 3D scanning-based inspection and repair volume construction of damaged aeroengine blades. As illustrated in Figure 7.1, the workflow of the proposed computational framework includes three main parts: scan-to-CAD rigid registration, section-specific geometric error evaluation, and damage-free digital twin construction.

The main challenge in the rigid registration of scanned point cloud of the damaged blades to their CAD model is that the measured data points of material-missing regions affect the alignment results of ICP-based methods. The least-squares minimization objective function of the ICP algorithm attempts to best-match the data points in both defective (material-missing) and non-defective regions with their corresponding points on the nominal model. This computation leads to averaging out errors in which the estimated errors at the damaged regions become smaller than the actual errors, and the estimated errors at the undamaged regions become larger than the actual errors. This thesis proposes the fine-tuned registration algorithm to provide an accurate scan-to-CAD matching between the damaged blade and its CAD model through group-to-group geometric dissimilarity evaluation between corresponding pairs and automatically remove the unreliable corresponding pairs with significant geometric nonconformities from the rigid registration process.

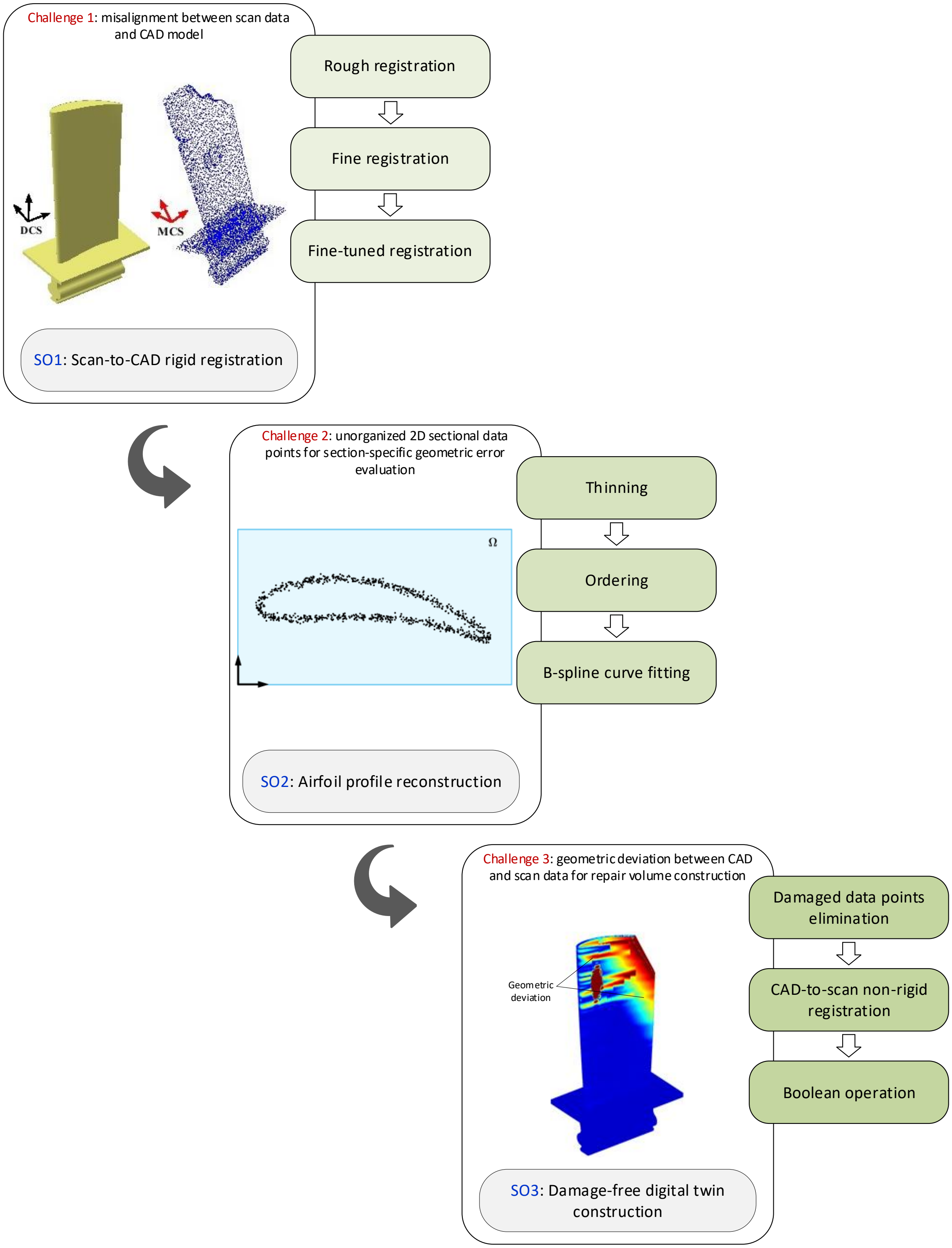

Figure 7.1 Workflow of the developed computational framework for 3D scanning-based virtual inspection and repair volume generation of damaged blades (based on the research objectives).

Once the scanned point cloud of the damaged blade is registered to the CAD model and both are in the design coordinate system, for any section-specific geometric error evaluation it is essential to construct the airfoil profile from unorganized and noisy projected 2D sectional data points. However, for the projected set of data points from the 3D scanned point cloud, the order of points is unknown for parametrization purposes. On other hand, the sectional projected data points are also scattered, which makes the data point ordering a challenge. This leads to a need for accurate airfoil profile reconstruction from scattered sectional data points. This thesis proposes an airfoil profile reconstruction method in which the scattered 2D data points are automatically thinned and ordered; and then, the smooth profile is approximated by fitting a B-spline curve to data.

After accurate section-specific inspection of the damaged blades, it is crucial to generate the repair volume in material-missing regions of the repairable blades for additive restoration. Due to extreme working conditions, the geometric shapes of aero-engine blades deviate and the original CAD model no longer represents the actual underlying geometry shape of the damaged blade. Thus, the Boolean difference between the original CAD model and scanned point cloud data of the damaged blade may not provide an accurate repair volume with a smooth transition between repaired and unrepaired regions. Moreover, applying a limited number of sectional profiles obtained from scan data could not provide sufficient information of underlying geometry of damaged blade for repair volume generation via interpolation/extrapolation methods. Therefore, there is a definite need to devise an approach to accurately deform the CAD model to best-match to undamaged regions of the scanned point cloud. This thesis presents an accurate CAD-to-scan non-rigid registration algorithm to match the CAD data points with the whole data points in undamaged regions of the scanned point cloud through incrementally deformation of CAD data points towards the measured data while maintaining the local rigidity of CAD points as much as possible.

7.2 Future Work

This thesis has successfully generated a computational framework for virtual inspection and repair volume generation of the damaged aero-engine blades from 3D scanned point cloud data. The following subjects are suggested for future research topics:

1- In this research, it is assumed that the filtered 3D scanned point cloud of the damaged blade is given as input to the proposed computational framework. However, due to undesirable reflections in the scanning process, the raw scan data of the blade is often contaminated by outliers at the high-curvature features i.e., leading and trailing edges, which may influence on the accuracy of the implemented algorithms. Therefore, an appropriate point cloud preprocessing scheme should be proposed for outlier removal, smoothing, and simplification of the raw scan data of the damaged blade while preserving the underlying geometry of the surface.

2- Due to the fact that many parameters affect the accuracy and efficiency of the proposed computational framework such as location, size, and geometry of damages on the blade surface, measurement noise, and point could density, it is desirable to develop deep learning methodologies such as Convolutional Neural Network (CNN) for intelligent inspection and repair volume construction of the damaged blades. Deep learning mainly can be explored to extract the intrinsic relation for damage detection (i.e., location and type of material missing damages) on the scan data of damaged blade and shape correspondence between scan data and CAD model for rigid and non-rigid registrations. In particular, the convolution operation can be designed based on intrinsic geometric properties of data points such as curvature, normal direction, and geodesic distance to capture the shape variations between the CAD model and scan data of the damaged blade. Thus, the constructed non-Euclidean CNN can be utilized to train the network for damaged blades (with the same design geometric specifications) containing different types of material-missing damages on the surface and point cloud quality (i.e., noise levels and point cloud density). Artificial intelligence-based inspection and repair of damaged blades can be of great interest for the MRO industry to improve the efficiency and accuracy in remanufacturing of the damaged blades.

REFERENCES

[1] B. Denkena, P. Nyhuis, B. Bergmann, N. Nübel, and T. Lucht, "Towards an autonomous maintenance, repair and overhaul process: Exemplary holistic data management approach for the regeneration of aero-engine blades," *Procedia Manufacturing,* vol. 40, pp. 77-82, 2019.

[2] T. Cooper, J. Smiley, C. Porter, and C. Precourt, "Global fleet & MRO market forecast commentary," *Olyver Wyman*, 2018.

[3] Z. Bi and L. Wang, "Advances in 3D data acquisition and processing for industrial applications," *Robotics and Computer-Integrated Manufacturing,* vol. 26, pp. 403-413, 2010.

[4] F. Khameneifar, "Section-specific geometric error evaluation of airfoil blades based on digitized surface data," University of British Columbia, 2015.

[5] T.-H. Hsu, J.-Y. Lai, and W.-D. Ueng, "On the development of airfoil section inspection and analysis technique," *The International Journal of Advanced Manufacturing Technology,* vol. 30, p. 129, 2006.

[6] F. Khameneifar and H.-Y. Feng, "A new methodology for evaluating position and orientation errors of airfoil sections," *The International Journal of Advanced Manufacturing Technology*, vol. 83, pp. 1013-1023, 2016.

[7] Y. Li and P. Gu, "Inspection of free-form shaped parts," *Robotics and Computer-Integrated Manufacturing,* vol. 21, pp. 421-430, 2005.

[8] P. J. Besl and N. D. McKay, "Method for registration of 3-D shapes," in *Sensor fusion IV: control paradigms and data structures*, 1992, pp. 586-606.

[9] F. Khameneifar and H.-Y. Feng, "Extracting sectional contours from scanned point clouds via adaptive surface projection," *International Journal of Production Research*, vol. 55, pp. 4466-4480, 2017.

[10] W.-l. Li, H. Xie, Q.-d. Li, L.-p. Zhou, and Z.-p. Yin, "Section curve reconstruction and mean-camber curve extraction of a point-sampled blade surface," *PloS one*, vol. 9, p. e115471, 2014.

[11] J. Zheng, Z. Li, and X. Chen, "Worn area modeling for automating the repair of turbine blades," *The International Journal of Advanced Manufacturing Technology,* vol. 29, pp. 1062-1067, 2006.

[12] Y. Zhang, Z. Yang, G. He, Y. Qin, and H.-c. Zhang, "Remanufacturing-oriented geometric modelling for the damaged region of components," *Procedia CIRP*, vol. 29, pp. 798-803, 2015.

[13] X. Zhang, W. Li, and F. Liou, "Damage detection and reconstruction algorithm in repairing compressor blade by direct metal deposition," *The International Journal of Advanced Manufacturing Technology*, vol. 95, pp. 2393-2404, 2018.

[14] M. Praniewicz, T. Kurfess, and C. Saldana, "An adaptive geometry transformation and repair method for hybrid manufacturing," *Journal of Manufacturing Science and Engineering*, vol. 141, 2019.

[15] C. Yan, W. Wan, K. Huang, L. Liu, and C.-H. Lee, "A reconstruction strategy based on CSC registration for turbine blades repairing," *Robotics and Computer-Integrated Manufacturing,* vol. 61, p. 101835, 2020.

[16] J. M. Wilson, C. Piya, Y. C. Shin, F. Zhao, and K. Ramani, "Remanufacturing of turbine blades by laser direct deposition with its energy and environmental impact analysis," *Journal of Cleaner Production,* vol. 80, pp. 170-178, 2014.

[17] O. Yilmaz, N. Gindy, and J. Gao, "A repair and overhaul methodology for aeroengine components," *Robotics and Computer-Integrated Manufacturing,* vol. 26, pp. 190-201, 2010.

[18] T.-H. Hsu, J.-Y. Lai, W.-D. Ueng, and J.-Z. Hwang, "An iterative coordinate setup algorithm for airfoil blades inspection," *The International Journal of Advanced Manufacturing Technology,* vol. 26, pp. 797-807, 2005.

[19] Y. Li and P. Gu, "Free-form surface inspection techniques state of the art review," *Computer-Aided Design,* vol. 36, pp. 1395-1417, 2004.

[20] J. E. Makem, H. Ou, and C. G. Armstrong, "A virtual inspection framework for precision manufacturing of aerofoil components," *Computer-Aided Design,* vol. 44, pp. 858-874, 2012.

[21] J. Makem, H. Ou, C. Armstrong, A. Rennie, and S. Nikov, "A virtual inspection technique for assessing the dimensional accuracy of forged compressor blades using FE modeling and CMM inspection," *International Journal of Material Forming,* vol. 1, pp. 375-378, 2008.

[22] J. B. Jones, P. McNutt, R. Tosi, C. Perry, and D. I. Wimpenny, "Remanufacture of turbine blades by laser cladding, machining and in-process scanning in a single machine," 2012.

[23] F. Hou, N. Wan, Z. Chang, Z. Chen, and H. Sun, "An adaptive repair surface modeling approach for worn blades," *The International Journal of Advanced Manufacturing Technology,* vol. 94, pp. 523-532, 2018.

[24] E. Savio, L. De Chiffre, and R. Schmitt, "Metrology of freeform shaped parts," *CIRP annals,* vol. 56, pp. 810-835, 2007.

[25] Z. Zheng-Qing, Z. Yun, and C. Zhi-Tong, "A repair strategy based on tool path modification for damaged turbine blade," *The International Journal of Advanced Manufacturing Technology,* vol. 106, pp. 2995-3006, 2020.

[26] H. J. Pahk and W. J. Ahn, "Precision inspection system for aircraft parts having very thin features based on CAD/CAI integration," *The International Journal of Advanced Manufacturing Technology,* vol. 12, pp. 442-449, 1996.

[27] R. J. Campbell and P. J. Flynn, "A survey of free-form object representation and recognition techniques," *Computer Vision and Image Understanding,* vol. 81, pp. 166-210, 2001.

[28] H. Ghorbani and F. Khameneifar, "Accurate registration of point clouds of damaged aeroengine blades," *Journal of Manufacturing Science and Engineering,* vol. 143, p. 031012, 2021.

[29] L. Li, C. Li, Y. Tang, and Y. Du, "An integrated approach of reverse engineering aided remanufacturing process for worn components," *Robotics and Computer-Integrated Manufacturing,* vol. 48, pp. 39-50, 2017.

[30] J. Huang, Y. Yuan, Z. Wang, Z. Qi, C. Xing, and J. Gao, "A global-to-local registration and error evaluation method of blade profile lines based on parameter priority," *The International Journal of Advanced Manufacturing Technology,* vol. 94, pp. 3829-3839, 2018.

[31] H. Yu and X. Lyu, "Repair of defective 3D blade model based on deformation of adjacent non-defective cross-sectional curve," *The International Journal of Advanced Manufacturing Technology,* vol. 95, pp. 3045-3055, 2018.

[32] J. M. Tam, K. M. Yu, and R. Sun, "Integrated computer-aided verification of turbine blade," *Computer-Aided Design and Applications,* vol. 12, pp. 589-600, 2015.

[33] X. Li, J. Barhak, I. Guskov, and G. Blake, "Automatic registration for inspection of complex shapes," *Virtual and Physical Prototyping,* vol. 2, pp. 75-88, 2007.

[34] M. Attia, Y. Slama, L. Peyrodie, H. Cao, and F. Haddad, "3D Point Cloud Coarse Registration based on Convex Hull Refined by ICP and NDT," in *2018 25th International Conference on Mechatronics and Machine Vision in Practice (M2VIP),* 2018, pp. 1-6.

[35] W. He, Z. Li, Y. Guo, X. Cheng, K. Zhong, and Y. Shi, "A robust and accurate automated registration method for turbine blade precision metrology," *The International Journal of Advanced Manufacturing Technology,* vol. 97, pp. 3711-3721, 2018.

[36] S. Ji, Y. Ren, Z. Ji, X. Liu, and G. Hong, "An improved method for registration of point cloud," *Optik,* vol. 140, pp. 451-458, 2017.

[37] D. OuYang, H.-Y. Feng, N. A Jahangir, and H. Song, "Robust initial matching of free-form objects represented by point clouds," *Journal of manufacturing science and engineering,* vol. 134, 2012.

[38] R. Rantoson, H. Nouira, N. Anwer, and C. Mehdi-Souzani, "Novel automated methods for coarse and fine registrations of point clouds in high precision metrology," *The International Journal of Advanced Manufacturing Technology,* vol. 81, pp. 795-810, 2015.

[39] Y.-S. Liu and K. Ramani, "Robust principal axes determination for point-based shapes using least median of squares," *Computer-Aided Design,* vol. 41, pp. 293-305, 2009.

[40] K. S. Arun, T. S. Huang, and S. D. Blostein, "Least-squares fitting of two 3-D point sets," *IEEE Transactions on pattern analysis and machine intelligence,* pp. 698-700, 1987.

[41] Y. Chen and G. Medioni, "Object modelling by registration of multiple range images," *Image and vision computing,* vol. 10, pp. 145-155, 1992.

[42] N. J. Mitra, N. Gelfand, H. Pottmann, and L. Guibas, "Registration of point cloud data from a geometric optimization perspective," in *Proceedings of the 2004 Eurographics/ACM SIGGRAPH symposium on Geometry processing,* 2004, pp. 22-31.

[43] J. Ding, Q. Liu, and P. Sun, "A robust registration algorithm of point clouds based on adaptive distance function for surface inspection," *Measurement Science and Technology,* vol. 30, p. 075003, 2019.

[44] L. Zhu, J. Barhak, V. Srivatsan, and R. Katz, "Efficient registration for precision inspection of free-form surfaces," *The International Journal of Advanced Manufacturing Technology,* vol. 32, pp. 505-515, 2007.

[45] J. Yu, Z. Chen, and Z. Jiang, "An approach for machining distortion measurements and evaluation of thin-walled blades with small datum," *Chinese Journal of Aeronautics,* vol. 29, pp. 1806-1814, 2016.

[46] T. Li, L. Gao, P. Li, and Q. Pan, "An ensemble fruit fly optimization algorithm for solving range image registration to improve quality inspection of free-form surface parts," *Information Sciences,* vol. 367, pp. 953-974, 2016.

[47] T. Li, L. Gao, Q. Pan, and P. Li, "Free-form surface parts quality inspection optimization with a novel sampling method," *Applied Soft Computing,* vol. 62, pp. 550-570, 2018.

[48] Y. Gao, Z. Du, M. Li, and W. Dong, "An automated approach for machining allowance evaluation of casting parts," *International Journal of Computer Integrated Manufacturing,* vol. 32, pp. 1043-1052, 2019.

[49] Y. Sijie, Z. Yunfei, P. Fangyu, and L. Xide, "Research on the localisation of the workpieces with large sculptured surfaces in NC machining," *The International Journal of Advanced Manufacturing Technology,* vol. 23, pp. 429-435, 2004.

[50] Z. Wang, Y. Li, Y. Tang, and Z. Shang, "Enhanced precision inspection of free-form surface with an improved whale optimization algorithm," *Optics Express,* vol. 29, pp. 26909-26924, 2021.

[51] R. Liu, Z. Wang, and F. Liou, "Multifeature-fitting and shape-adaption algorithm for component repair," *Journal of Manufacturing Science and Engineering,* vol. 140, p. 021003, 2018.

[52] X. Zhang, W. Li, K. M. Adkison, and F. Liou, "Damage reconstruction from tri-dexel data for laser-aided repairing of metallic components," *International Journal of Advanced Manufacturing Technology,* vol. 96, 2018.

[53] W. Wang, H. Pottmann, and Y. Liu, "Fitting B-spline curves to point clouds by curvature-based squared distance minimization," *ACM Transactions on Graphics (ToG),* vol. 25, pp. 214-238, 2006.

[54] H. Pottmann, S. Leopoldseder, and M. Hofer, "Approximation with active B-spline curves and surfaces," in *10th Pacific Conference on Computer Graphics and Applications, 2002. Proceedings.,* 2002, pp. 8-25.

[55] D. F. Rogers and N. Fog, "Constrained B-spline curve and surface fitting," *Computer-Aided Design,* vol. 21, pp. 641-648, 1989.

[56] T. Speer, M. Kuppe, and J. Hoschek, "Global reparametrization for curve approximation," *Computer Aided Geometric Design,* vol. 15, pp. 869-877, 1998.

[57] W. Zheng, P. Bo, Y. Liu, and W. Wang, "Fast B-spline curve fitting by L-BFGS," *Computer Aided Geometric Design,* vol. 29, pp. 448-462, 2012.

[58] H. Yang, W. Wang, and J. Sun, "Control point adjustment for B-spline curve approximation," *Computer-Aided Design,* vol. 36, pp. 639-652, 2004.

[59] L. Chen and S. K. Ghosh, "Uncertainty quantification and estimation of closed curves based on noisy data," *Computational Statistics,* pp. 1-16, 2021.

[60] T. Sabsch, C. Braune, A. Dockhorn, and R. Kruse, "Using a multiobjective genetic algorithm for curve approximation," in *2017 IEEE symposium series on computational intelligence (SSCI)*, 2017, pp. 1-6.

[61] M. Sarfraz, M. Riyazuddin, and M. Baig, "Capturing planar shapes by approximating their outlines," *Journal of Computational and Applied Mathematics,* vol. 189, pp. 494-512, 2006.

[62] A. Iglesias, A. Galvez, and M. Collantes, "Multilayer embedded bat algorithm for B-spline curve reconstruction," *Integrated Computer-Aided Engineering,* vol. 24, pp. 385-399, 2017.

[63] D. Levin, "The approximation power of moving least-squares," *Mathematics of computation,* vol. 67, pp. 1517-1531, 1998.

[64] I.-K. Lee, "Curve reconstruction from unorganized points," *Computer aided geometric design,* vol. 17, pp. 161-177, 2000.

[65] S.-W. Cheng, S. Funke, M. Golin, P. Kumar, S.-H. Poon, and E. Ramos, "Curve reconstruction from noisy samples," *Computational Geometry,* vol. 31, pp. 63-100, 2005.

[66] T. K. Dey and P. Kumar, "A Simple Provable Algorithm for Curve Reconstruction," in *SODA*, 1999, pp. 893-894.

[67] S. Ohrhallinger and M. Wimmer, "Stretchdenoise: Parametric curve reconstruction with guarantees by separating connectivity from residual uncertainty of samples," *arXiv preprint arXiv:1808.07778,* 2018.

[68] S. Ohrhallinger and M. Wimmer, "Fitconnect: Connecting noisy 2d samples by fitted neighbourhoods," in *Computer Graphics Forum*, 2019, pp. 126-137.

[69] S. Ohrhallinger, S. A. Mitchell, and M. Wimmer, "Curve reconstruction with many fewer samples," in *Computer Graphics Forum*, 2016, pp. 167-176.

[70] N. Amenta, M. Bern, and D. Eppstein, "The crust and the β-skeleton: Combinatorial curve reconstruction," *Graphical models and image processing,* vol. 60, pp. 125-135, 1998.

[71] H. Lin, W. Chen, and G. Wang, "Curve reconstruction based on an interval B-spline curve," *The Visual Computer,* vol. 21, pp. 418-427, 2005.

[72] J. Wang, Z. Yu, W. Zhang, M. Wei, C. Tan, N. Dai, *et al.*, "Robust reconstruction of 2D curves from scattered noisy point data," *Computer-Aided Design,* vol. 50, pp. 27-40, 2014.

[73] M. W. Rupniewski, "Curve Reconstruction from Noisy and Unordered Samples," in *ICPRAM*, 2014, pp. 183-188.

[74] X. Zhang, W. Cui, and F. Liou, "Voxel-Based Geometry Reconstruction for Repairing and Remanufacturing of Metallic Components Via Additive Manufacturing," *International Journal of Precision Engineering and Manufacturing-Green Technology,* pp. 1-24, 2021.

[75] X. Zhang, W. Li, W. Cui, and F. Liou, "Modeling of worn surface geometry for engine blade repair using Laser-aided Direct Metal Deposition process," *Manufacturing letters,* vol. 15, pp. 1-4, 2018.

[76] B. Wu, H. Zheng, J. Wang, and Y. Zhang, "Geometric model reconstruction and CNC machining for damaged blade repair," *International Journal of Computer Integrated Manufacturing,* vol. 33, pp. 287-301, 2020.

[77] J. Gao, X. Chen, O. Yilmaz, and N. Gindy, "An integrated adaptive repair solution for complex aerospace components through geometry reconstruction," *The International Journal of Advanced Manufacturing Technology,* vol. 36, pp. 1170-1179, 2008.

[78] C. Piya, J. M. Wilson, S. Murugappan, Y. Shin, and K. Ramani, "Virtual repair: geometric reconstruction for remanufacturing gas turbine blades," in *International Design Engineering Technical Conferences and Computers and Information in Engineering Conference*, 2011, pp. 895-904.

[79] J. Aschenbruck, R. Adamczuk, and J. R. Seume, "Recent progress in turbine blade and compressor blisk regeneration," *Procedia CIRP,* vol. 22, pp. 256-262, 2014.

[80] B. Denkena, V. Boess, D. Nespor, F. Floeter, and F. Rust, "Engine blade regeneration: a literature review on common technologies in terms of machining," *The International Journal of Advanced Manufacturing Technology,* vol. 81, pp. 917-924, 2015.

[81] W.-l. Li, L.-p. Zhou, and S.-J. Yan, "A case study of blade inspection based on optical scanning method," *International Journal of Production Research,* vol. 53, pp. 2165-2178, 2015.

[82] J. Gao, J. Folkes, O. Yilmaz, and N. Gindy, "Investigation of a 3D non-contact measurement based blade repair integration system," *Aircraft Engineering and Aerospace Technology,* 2005.

[83] J. Gao, N. Gindy, and X. Chen, "An automated GD&T inspection system based on non-contact 3D digitization," *International journal of production research,* vol. 44, pp. 117-134, 2006.

[84] F. Khameneifar and H.-Y. Feng, "Airfoil profile reconstruction under the uncertainty of inspection data points," *The International Journal of Advanced Manufacturing Technology,* vol. 71, pp. 675-683, 2014.

[85] Y. Li and P. Gu, "Automatic localization and comparison for free-form surface inspection," *Journal of manufacturing systems,* vol. 25, pp. 251-268, 2006.

[86] S. Rusinkiewicz and M. Levoy, "Efficient variants of the ICP algorithm," in *Proceedings third international conference on 3-D digital imaging and modeling,* 2001, pp. 145-152.

[87] J. Salvi, C. Matabosch, D. Fofi, and J. Forest, "A review of recent range image registration methods with accuracy evaluation," *Image and Vision computing,* vol. 25, pp. 578-596, 2007.

[88] E. Trucco, A. Fusiello, and V. Roberto, "Robust motion and correspondence of noisy 3-D point sets with missing data," *Pattern recognition letters,* vol. 20, pp. 889-898, 1999.

[89] S. Granger and X. Pennec, "Multi-scale EM-ICP: A fast and robust approach for surface registration," in *European Conference on Computer Vision*, 2002, pp. 418-432.

[90] J. M. Phillips, R. Liu, and C. Tomasi, "Outlier robust ICP for minimizing fractional RMSD," in *Sixth International Conference on 3-D Digital Imaging and Modeling (3DIM 2007)*, 2007, pp. 427-434.

[91] C. Feng, J. Liang, C. Gong, W. Pai, and S. Liu, "Repair volume extraction method for damaged parts in remanufacturing repair," *The International Journal of Advanced Manufacturing Technology*, vol. 98, pp. 1523-1536, 2018.

[92] N. Gelfand, N. J. Mitra, L. J. Guibas, and H. Pottmann, "Robust global registration," in *Symposium on geometry processing*, 2005, p. 5.

[93] F. Khameneifar and H.-Y. Feng, "Establishing a balanced neighborhood of discrete points for local quadric surface fitting," *Computer-Aided Design,* vol. 84, pp. 25-38, 2017.

[94] F. Khameneifar and H. Ghorbani, "On the curvature estimation for noisy point cloud data via local quadric surface fitting," *Comput.-Aided Des. Appl.,* vol. 16, pp. 140-149, 2019.

[95] M. P. d. Carmo, *Differential Geometry of Curves and Surfaces*: Prentice-Hall, Englewood Cliffs, 1976.

[96] M. D. Shapiro and M. B. Blaschko, "On hausdorff distance measures," *Computer Vision Laboratory University of Massachusetts, Amherst, MA,* vol. 1003, 2004.

[97] M.-L. Zhang and Z.-H. Zhou, "Multi-instance clustering with applications to multi-instance prediction," *Applied intelligence,* vol. 31, pp. 47-68, 2009.

[98] P. Ghandali, F. Khameneifar, and J. Mayer, "A pseudo-3D ball lattice artifact and method for evaluating the metrological performance of structured-light 3D scanners," *Optics and Lasers in Engineering,* vol. 121, pp. 87-95, 2019.

[99] D. Brujic and M. Ristic, "Monte Carlo simulation and analysis of free-form surface registration," *Proceedings of the Institution of Mechanical Engineers, Part B: Journal of Engineering Manufacture,* vol. 211, pp. 605-617, 1997.

[100] Y. Wang and H.-Y. Feng, "Outlier detection for scanned point clouds using majority voting," *Computer-Aided Design,* vol. 62, pp. 31-43, 2015.

[101] W.-L. Li, H. Xie, G. Zhang, Q.-D. Li, and Z.-P. Yin, "Adaptive bilateral smoothing for a point-sampled blade surface," *IEEE/ASME Transactions on Mechatronics,* vol. 21, pp. 2805-2816, 2016.

[102] W.-l. Li, H. Xie, G. Zhang, S.-j. Yan, and Z.-p. Yin, "3-D shape matching of a blade surface in robotic grinding applications," *IEEE/ASME Transactions on Mechatronics,* vol. 21, pp. 2294-2306, 2016.

[103] H. Xie, W.-L. Li, Z.-P. Yin, and H. Ding, "Variance-Minimization iterative matching method for free-form surfaces—Part I: Theory and method," *IEEE Transactions on Automation Science and Engineering,* vol. 16, pp. 1181-1191, 2018.

[104] H. Xie, W.-l. Li, Z.-P. Yin, and H. Ding, "Variance-Minimization iterative matching method for free-form surfaces—Part II: Experiment and analysis," *IEEE Transactions on Automation Science and Engineering,* vol. 16, pp. 1192-1204, 2018.

[105] Z. Yun, C. Zhi-Tong, and N. Tao, "Reverse modeling strategy of aero-engine blade based on design intent," *The International Journal of Advanced Manufacturing Technology,* vol. 81, pp. 1781-1796, 2015.

[106] B. Wu, J. Wang, Y. Zhang, and M. Luo, "Adaptive location of repaired blade for multi-axis milling," *Journal of Computational Design and Engineering,* vol. 2, pp. 261-267, 2015.

[107] G. Xiao and Y. Huang, "Surface reconstruction of laser-cladding remanufacturing blade using in adaptive belt grinding," *International Journal of Advanced Manufacturing Technology,* vol. 101, 2019.

[108] W. Ma and J.-P. Kruth, "Parameterization of randomly measured points for least squares fitting of B-spline curves and surfaces," *Computer-Aided Design,* vol. 27, pp. 663-675, 1995.

[109] Y. Liu, H. Pottmann, and W. Wang, "Constrained 3D shape reconstruction using a combination of surface fitting and registration," *Computer-Aided Design,* vol. 38, pp. 572-583, 2006.

[110] P. Lancaster and K. Salkauskas, "Surfaces generated by moving least squares methods," *Mathematics of computation,* vol. 37, pp. 141-158, 1981.

[111] M. Alexa, J. Behr, D. Cohen-Or, S. Fleishman, D. Levin, and C. T. Silva, "Computing and rendering point set surfaces," *IEEE Transactions on visualization and computer graphics,* vol. 9, pp. 3-15, 2003.

[112] S. Fleishman, D. Cohen-Or, and C. T. Silva, "Robust moving least-squares fitting with sharp features," *ACM transactions on graphics (TOG),* vol. 24, pp. 544-552, 2005.

[113] W. S. Cleveland, "Robust locally weighted regression and smoothing scatterplots," *Journal of the American statistical association,* vol. 74, pp. 829-836, 1979.

[114] A. Nealen, "An as-short-as-possible introduction to the least squares, weighted least squares and moving least squares methods for scattered data approximation and interpolation," *URL: http://www. nealen. com/projects,* vol. 130, p. 25, 2004.

[115] P. Teunissen, *Dynamic Data Processing; Recursive Least Squares*, 2001.

[116] L. Piegl and W. Tiller, *The NURBS book*: Springer Science & Business Media, 1996.

[117] C. De Boor and C. De Boor, *A practical guide to splines* vol. 27: springer-verlag New York, 1978.

[118] Y. Zhang, Z.-T. Chen, and T. Ning, "Efficient measurement of aero-engine blade considering uncertainties in adaptive machining," *The International Journal of Advanced Manufacturing Technology,* vol. 86, pp. 387-396, 2016.

[119] B. Wu, H. Zheng, Y. Zhang, M. Luo, and D. Zhang, "A Model Reconstruction Method of Blade Repair Based on Linear Combination," *International Journal of Precision Engineering and Manufacturing,* vol. 22, pp. 383-394, 2021.

[120] H. Ghorbani and F. Khameneifar, "Scan-to-CAD alignment of damaged airfoil blade point clouds through geometric dissimilarity assessment," *Procedia CIRP,* 2022.

[121] X. Zhao, Y. Pan, C. Zhou, Y. Chen, and C. C. Wang, "An integrated CNC accumulation system for automatic building-around-inserts," *Journal of Manufacturing Processes,* vol. 15, pp. 432-443, 2013.

[122] C. Su, X. Jiang, G. Huo, Q. Zou, Z. Zheng, and H.-Y. Feng, "Accurate model construction of deformed aero-engine blades for remanufacturing," *The International Journal of Advanced Manufacturing Technology,* vol. 106, pp. 3239-3251, 2020.

[123] S. Patro and K. K. Sahu, "Normalization: A preprocessing stage," *arXiv preprint arXiv:1503.06462,* 2015.

[124] B. Amberg, S. Romdhani, and T. Vetter, "Optimal step nonrigid ICP algorithms for surface registration," in *2007 IEEE conference on computer vision and pattern recognition*, 2007, pp. 1-8.

[125] H. Ghorbani and F. Khameneifar, "Airfoil profile reconstruction from unorganized noisy point cloud data," *Journal of Computational Design and Engineering*, vol. 8, pp. 740-755, 2021.

[126] A. Jacobson, D. Panozzo, C. Schüller, O. Diamanti, Q. Zhou, and N. Pietroni, "libigl: A simple C++ geometry processing library," ed, 2018.

[127] Q. Zhou, E. Grinspun, D. Zorin, and A. Jacobson, "Mesh arrangements for solid geometry," *ACM Transactions on Graphics (TOG),* vol. 35, pp. 1-15, 2016.

APPENDIX A SCAN-TO-CAD ALIGNMENT OF DAMAGED AIRFOIL BLADE POINT CLOUDS THROUGH GEOMETRIC DISSIMILARITY ASSESSMENT

In Chapter 3, we evaluated the effectiveness of the proposed scan-to-CAD registration method using various numerical case studies [28]. Here, we compare the result of the proposed rigid registration method and the standard ICP algorithm for the experimental case study using scanned point cloud data of a damaged blade. The damaged blade was scanned using an ATOS Core 200 (GOM, Braunschweig, Germany) structured-light 3D scanner. Figure A.1 shows the damaged blade, scanned point cloud data, and the nominal CAD model. As can be seen in Figure A.1, the scanned point cloud data has an arbitrary relative position and orientation with respect to the CAD model. The scanned point cloud contains 950,202 points with an average point spacing of 0.08 mm. The damaged blade contains voids and tip damage (see Figure A.1), which are common material-missing type damages on the surface of the aero-engine blades. The point cloud of the CAD model is also obtained by the uniform sampling of the surface with the average point spacing equal to scanned point cloud data (i.e., 0.08 mm) to analyze the same surface area on both CAD surface and the underlying surface of the scan data for the subsequent curvature and distance analysis.

The PCA method and original ICP algorithm are applied respectively for rough and fine matching [28]. The classical point-to-point minimization algorithm has been used to globally minimize the root mean square error (*RMSE*) of the measured data from the CAD model and compute the transformation parameters $\boldsymbol{T}$ and $\boldsymbol{R}$ in Equation (3.1). The iteration is terminated when the change of the global registration error falls below the threshold, which is set to be $\mu=10^{-6}$.

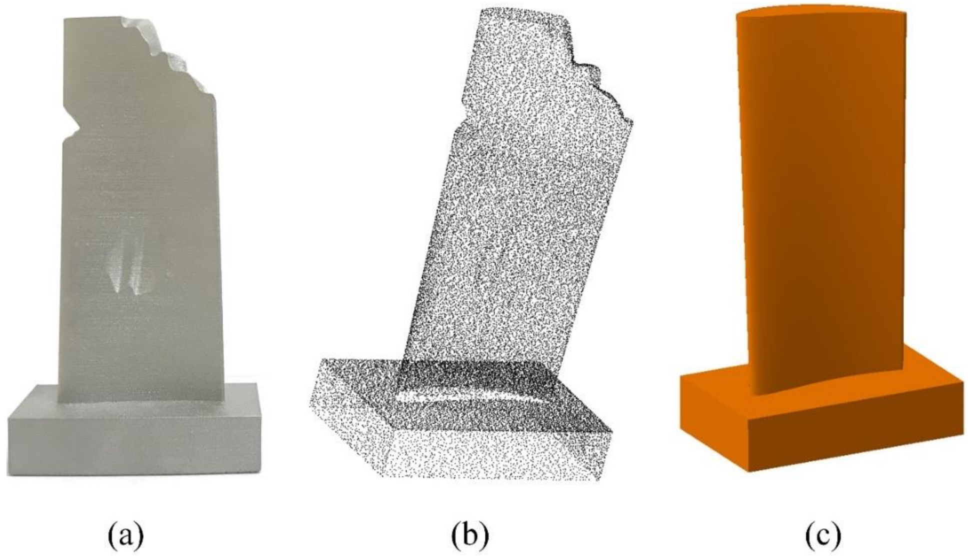

Figure A.1(a) Damaged blade, (b) scanned point cloud of the damaged blade, and (c) the nominal CAD model.

Figure A.2(a) shows the point cloud data of the damaged blade with its colormap based on the absolute deviations from the CAD model after being aligned using the fine-tuned registration procedure. Figure A.2(b), illustrates the removed data points (in black) at the end of the last iteration of the fine-tuned registration. Using the proposed method, almost all data points of the damaged regions are eliminated from the registration process. It is seen in Figure A.2(b) that some data points of the undamaged regions in the trailing edge and sharp edges of the blade tail are also removed as unreliable points. Since only a tiny portion of data points in undamaged regions are removed as unreliable points, it does not affect the accuracy of the registration outcome. It should be noted that we have employed the raw scanned point cloud data of the blade as input, which is contaminated by outliers at the high-curvature features.

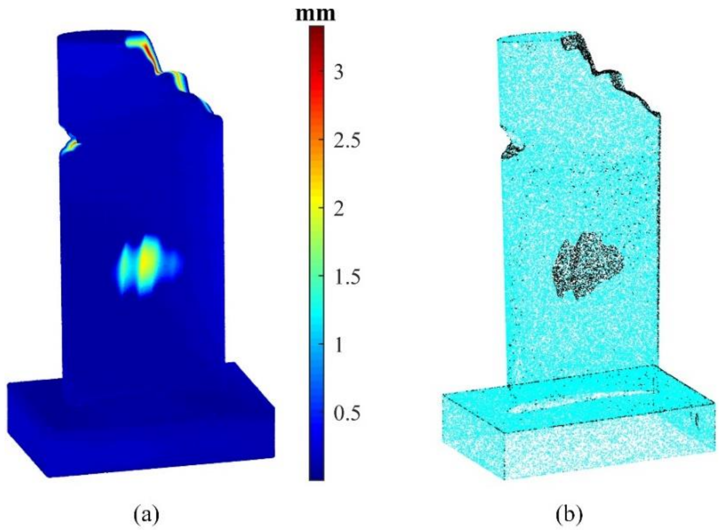

Figure A.2(a) Error colormap of the aligned scanned point cloud data, and (b) the removed data points (in black) after the last iteration of the fine-tuned alignment.

To locally investigate the averaging-out errors resulted from the original ICP algorithm, the point cloud data of both damaged blade and CAD model are sectioned by 17 equidistant sectional planes parallel to XY-plane of the CAD model from the bottom (Z=20 mm) to top (Z=100 mm) of the blade. Then, the data points in 0.1 mm distance from each sectional plane are specified as sectional data. The post-alignment errors are analyzed for each sectional data to compare the performance of the proposed method and standard ICP algorithm. Figure A.3 shows the *RMSE* of sectional data points of the scanned point cloud from the CAD model after the original ICP (in red) and fine-tuned registration (in black). The sectional planes 4-6 and 12-17 are in damaged regions, and sectional planes 1-3 and 7-11 are in undamaged areas. As can be seen in Figure A.3, the post-alignment sectional *RMSE* values of the ICP method in damaged regions are smaller than the post-alignment sectional *RMSE* values of the proposed method and in undamaged regions are larger than the *RMSE* values of the proposed method. The maximum absolute deviation between the two is 21.5 μm at the tip of the blade (sectional plane #17). As discussed earlier, these averaging-out errors result from global minimization of the least-squares objective function of ICP. It should be noted that the averaging-out error values depend on the size and the geometry of damages on the scanned damaged blade. The results of aligning the scanned point cloud data of the damaged blade with the CAD model demonstrated that the proposed fine-tuned scan-to-CAD alignment method is successful in avoiding the averaging-out errors of the original ICP algorithm.

The results of Appendix A has been presented at the CIRP ICME conference [120].

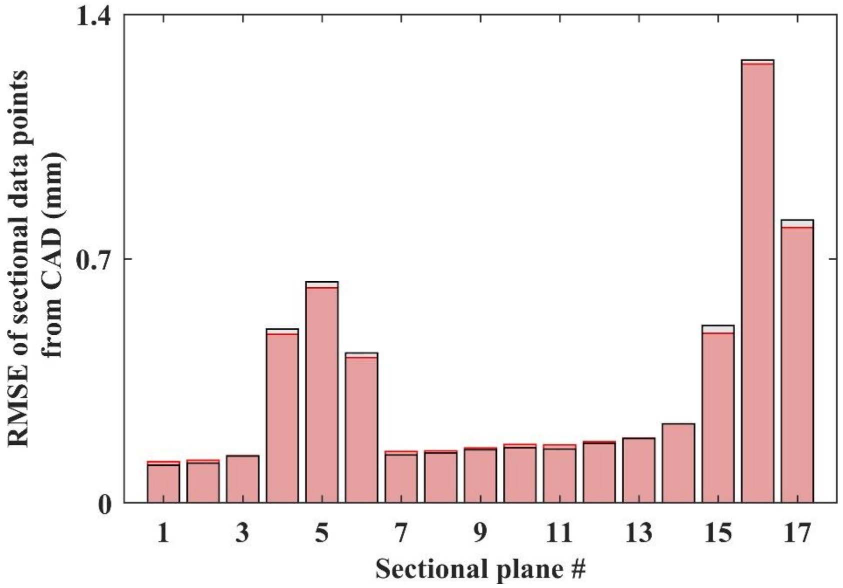

Figure A.3 Deviation of post-alignment *RMSE* of sectional data points from the CAD sectional data points after original ICP registration (in red) and the proposed method (in black).